Chapter 2
Dynamics and Control of Electrostatic Flight

Marco B. Quadrelli, Michele Bechini, Joseph Wang, and Shota Kikuchi

Abstract We describe the principles of electrostatic flight in tenuous plasma around solar system bodies. The lack of an atmosphere, low gravity levels, and unknown surface soil properties pose a very difficult challenge for all forms of known locomotion at airless bodies. The environment near the surface of asteroids, comets, and the Moon is electrically charged due to the Sun's photoelectric bombardment and lofting dust, which follows the Sun's illumination as the body spins. If a body with high surface resistivity is exposed to solar wind and solar radiation, Sun-exposed areas and shadowed areas become differentially charged. Our work in this field is motivated by the E-Glider, i.e., the Electrostatic Glider, which provides an enabling capability for practical electrostatic flight at airless bodies, a solution applicable to many types of in situ missions, which leverages the natural environment. The E-Glider is a small spacecraft that uses, instead of avoids, the charged environment in the solar system for near fuel-less circumnavigation, allows in situ characterization of the plasmasphere of planetary bodies, and reduces the risk of landing on hazardous surfaces.

M. B. Quadrelli (✉)
Jet Propulsion Laboratory, California Institute of Technology, 4800 Oak Grove Drive, Pasadena, CA 91109-8099, USA
e-mail: marco.b.quadrelli@jpl.nasa.gov

M. Bechini
Department of Aerospace Science and Technology (DAER), Politecnico di Milano, Via La Masa 34, 20156 Milano, Italy
e-mail: michele.bechini@polimi.it

J. Wang
Department of Astronautical Engineering, University of Southern California, 3650 S. McClintock Avenue, Los Angeles, CA 90089, USA
e-mail: josephjw@usc.edu

S. Kikuchi
Japan Aerospace Exploration Agency (JAXA), Kanagawa, Japan
e-mail: kikuchi.shota@perc.it-chiba.ac.jp

Planetary Exploration Research Center, Chiba Institute of Technology, 2-17-1 Tsudanuma, Narashino, Chiba 275-0016, Japan

V. Badescu et al. (eds.), *Handbook of Space Resources*,
https://doi.org/10.1007/978-3-030-97913-3_2

2.1 Introduction

Small airless bodies in the solar system (small asteroids and comets) represent the next frontier in deep space exploration. Recent studies have demonstrated the important role played by small airless bodies in the origin and history of the solar system (Quadrelli et al. 2017b). Understanding small airless bodies also contributes directly to research addressing the characteristics of the solar system that led to the origin of life. The National Research Council has designated technologies for exploring small bodies as a high priority for NASA because of their destination potential for both scientific discovery and human spaceflight (which would also likely require precursor robotic missions) (Council 2011).

Currently, our knowledge of small bodies is mostly obtained from remote sensing. While remote sensing is very useful in providing information from a distance, an in-depth knowledge requires proximity and in situ measurements. Small satellites (SmallSat) (including CubeSats and nanosatellites) can enable a wide range of proximity missions around small bodies.

In the last few years, nanosatellites have found numerous interesting applications in commercial and scientific missions. Their role has switched from the old concept of a cheap and highly reliable small technology demonstrator to one of the most adopted technologies in space application, especially for Earth observation. The novelty in the application of nanosatellites lies in interplanetary missions and high-level scientific missions. To make these types of missions feasible for a nanosatellite, a "push" in the development of new advanced technologies is required. In particular, the main fields in which the biggest effort should be employed are propulsion (state-of-the-art solutions are chemical and electric thrusters (Páscoa et al. 2018), but two promising technologies are solar sails and field-emission electric propulsors), communication (low-power deep space systems), and navigation and control (autonomous navigation and high-accuracy pointing). If properly developed, these technologies can lead to the beginning of a new era of space exploration based on less expensive but more versatile spacecraft with new operational capabilities.

However, mobility around small bodies is highly challenging (Quadrelli et al. 2017b). Gravitational acceleration produced by small bodies is very small, typically on the order of the milli-G order of magnitude (Quadrelli et al. 2017b). The shape of asteroids/comets is typically extremely irregular, and the mass distribution is typically nonuniform. Hence, the gravity field around small bodies is typically highly complex (Scheeres 1994; Scheeres et al. 2006).

The National Research Council (USA) stated that the development of new technologies for small-body mobility should be of high priority for NASA (Council 2011). Moreover, recent observations have demonstrated the relevance of small bodies from an astrobiological point of view (Quadrelli et al. 2017b), making their exploration extremely intriguing. In situ analysis of small bodies like asteroids and comets is limited by the knowledge of the surface terrain since all the current robotics and human systems rely on the interaction between the system itself and the main body surface. Several studies have revealed that the surface of small bodies can show

extremely different landscapes composed of a thick layer of fine regolith in some cases or by big boulders in other cases (Han 2015; Scheeres et al. 2006). Recently, some advanced vehicle concepts capable of operating in extreme conditions like the ones depicted above have been proposed, for example, the DuAxel vehicle (Nesnas et al. 2012) which will be capable of operating in extremely challenging surface conditions, or the recently assembled small helicopter capable of flying in Mars' atmosphere (Withrow-Maser et al. 2020), avoiding the problems related to the surface conformation. Despite the extremely fascinating capabilities of these vehicles, they are still not suitable for applications on a small airless body due to the extremely challenging conditions for mobility.

The environment presented by small bodies is extremely challenging (Quadrelli et al. 2017b). Due to the extremely irregular shape presented by some asteroids, the gravity field can be highly irregular, especially on the surfaces (Scheeres 1994; Scheeres et al. 2006). The combined effects of the irregularity of the gravity field and the low intensity of the gravitational acceleration produced by these bodies (milli-G order of magnitude Quadrelli et al. 2017b) make the environment highly perturbed (Scheeres 2012). The effects of solar radiation pressure (SRP) have been proven to have a strong impact on vehicle dynamics (Scheeres 1994, 1999). As a result of this highly perturbed environment, escape velocities from these bodies are particularly low (Scheeres and Marzari 2002; Scheeres 2007). This must be carefully taken into account both for landers and orbiters, and for these reasons, vehicles that operate in micro-gravity are different from planetary vehicles, requiring special precautions in the design phase. Mobility in this environment is currently achieved by using hoppers, grippers, and hybrid systems (Seeni et al. 2010; Quadrelli et al. 2012). No other solutions are present at this time (Quadrelli et al. 2017b). Another promising idea is to take advantage of the environment near the airless body, developing the vehicle named Electrostatic Glider (E-Glider) capable of exploiting the naturally charged particle environment near the surface to produce lift (Quadrelli et al. 2017b).

As will be discussed later, for small satellites, the effects from solar radiation pressure and electrostatic interactions between a charged airless body and a charged spacecraft can become comparable to that of a gravitation field, and can thus have a strong impact on the vehicle dynamics (Scheeres 1994, 1999; Cui and Wang 2019). The combined effects from a small and irregular gravitational field and the perturbations from solar radiation pressure and Coulomb force make the dynamic environment around small bodies highly complex (Scheeres 2012). As a result, vehicles that operate in such a highly perturbed micro-gravity environment need to satisfy a set of mobility requirements different from standard planetary spacecraft. Various propulsion options and mobility concepts have been previously proposed for small-body missions, such as solar sails, electrospray thrusters, hoppers, grippers, and hybrid systems (Seeni et al. 2010; Quadrelli et al. 2012).

The E-Glider concept, developed at NASA's Jet Propulsion Laboratory (Quadrelli et al. 2017b), is a new technology that can offer significantly more advantageous propulsion and navigation capabilities for proximity operations around small airless bodies using SmallSats.

This concept makes it possible to have a "closer look" at the asteroid surface without touching it and thus avoiding all the problems related to interacting with an extremely uncertain surface.

The E-Glider concept utilizes the electrostatic force between spacecraft and the naturally charged environment in proximity of an airless body for mobility. Without a global magnetic field and an atmosphere, small airless bodies are directly exposed to solar radiation and space plasma and thus are electrically charged by the ambient plasma and the emissions of photoelectrons and secondary electrons. A spacecraft around a small airless body is also electrically charged by the same process. By manipulating the charging state of a "glider" and thus the Coulomb force, an E-Glider may achieve complex orbital maneuvers beyond the capabilities of other mobility options.

We note that utilizing the electrostatic interaction between charged bodies had been considered for possible space applications in recent years, such as for docking, formation flying, collision avoidance, and attitude control (Quadrelli et al. 2017b; Schaub et al. 2004; Aslanov and Schaub 2019; King et al. 2002). However, these applications differ from the E-Glider concept because all of them rely on the Coulomb forces artificially generated between two (or more) spacecraft, while the E-Glider interacts directly with the electrostatic field around small bodies.

The E-Glider vehicle concept is bioinspired by small spiders (named *gossamer or ballooning spiders*) that produce charged threads that are mutually repelled (creating a sort of "hot-air balloon" made by thin threads) due to the presence of an electric charge, which also interacts with the Earth's static atmospheric electric field, generating a lift component on the spider itself (Morley and Robert 2018). This *ballooning* is effective also in absence of convection or aerodynamics effects. Thus, behaving like a gossamer spider, the E-Glider transforms the problem of the spacecraft charging into an advantage being capable of orbiting and maneuvering due to electrostatic interactions with the environment (see Fig. 2.1).

This paper proposes the two distinct types of operations for an E-glider, namely, electrostatic hovering and electrostatic orbiting. The basic strategy of electrostatic hovering is to create artificial equilibrium points by inducing repulsive electrostatic force. These artificial equilibrium points are present not only on the nightside but also on the dayside, unlike natural equilibrium points, as illustrated in Fig. 2.2. Therefore, the proposed method can potentially achieve fuel-free hovering on the dayside without experiencing an eclipse. On the other hand, the utilization of electrostatic force offers advantages for orbiting operations as well. This paper identifies a new class of periodic orbits around asteroids using electrostatic force, which is called *electrostatic periodic orbits*. In contrast to the natural terminator orbits, these orbits are displaced from the terminator plane in the direction of the Sun, as depicted in Fig. 2.2, enabling the observation of the sunlit side of an asteroid. Besides, the electrostatic periodic orbits are Sun-synchronous, thereby ensuring constant illumination from the Sun. Another advantage of electrostatic orbiting is that it only requires a small amount of power; for example, some electrostatic periodic orbits consume only a few watts of electricity.

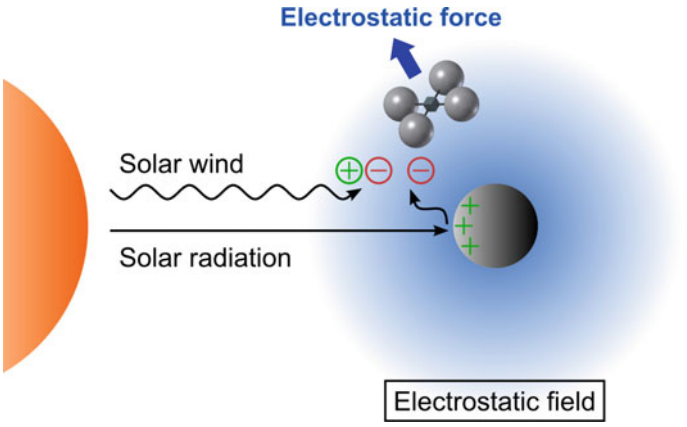

a) E-Glider Concept

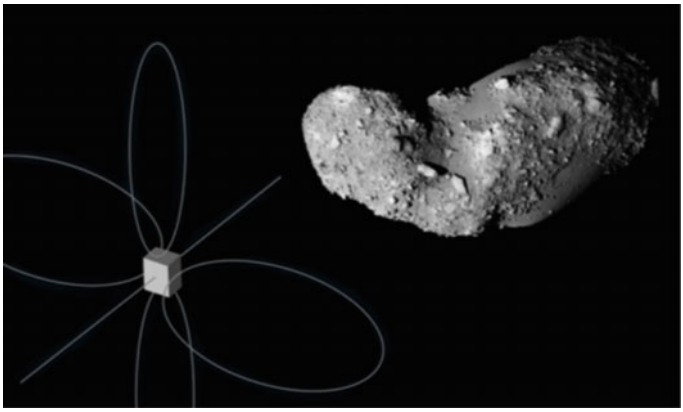

b) E-Glider Artistic Concept

Fig. 2.1 E-Glider concept (**a**) and artistic concept (**b**) of an E-Glider approaching 25143 Itokawa (Corradino 2018)

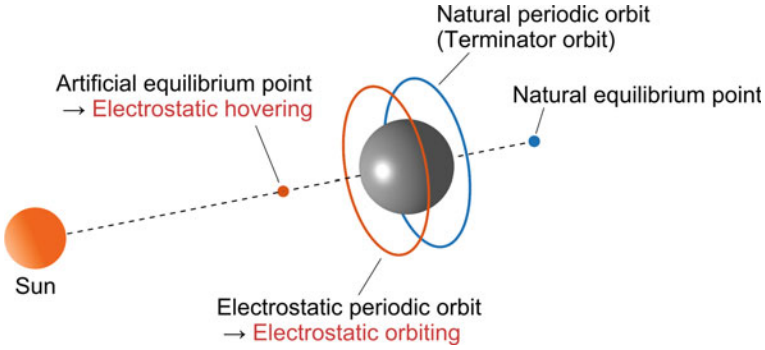

Fig. 2.2 Electrostatic hovering and electrostatic orbiting

As mentioned above, electrostatic hovering and electrostatic orbiting methods using an E-glider allow dayside operation without requiring any fuel. Therefore, the proposed methods are advantageous for mass budget, optical observation, solar power generation, and thermal design. By virtue of these characteristics, the E-Glider enables asteroid missions with lower cost and higher scientific value. For instance, an E-Glider could serve as a daughter spacecraft (secondary spacecraft deployed by a bigger spacecraft that acts as the mother spacecraft) for close observation of an asteroid. In addition to these practical advantages, this study is also intriguing in that completely new aspects of astrodynamics are revealed.

Many science objectives can be addressed by the E-Glider at small bodies, such as determining surface mechanical properties, searching for in situ resources, and understanding and simulating human activities in a low-gravity environment, among many others. Thanks to recent advances in miniaturization, several science-grade instruments are becoming available for implementation on small vehicles such as CubeSats. Some of these instruments which could be suitable for use on the E-Glider are (Kobrick et al. 2014) quadrupole ion trap spectrometers (2.5 kg, with isotopic accuracy $< 1\%$), snow and water imaging spectrometers (with high throughput, low polarization, high uniformity, in the 350–1700-nm spectral range), advanced infrared photodetectors (thermal sensitivity of 0.2°), high-resolution visible cameras (used for science, optical navigation, and autonomous navigation demonstration), and micro-seismometers.

To alter the charge level of the electrodes of the E-Glider, the methods described in Quadrelli et al. (2017a) have been considered. A "classic" charge ejection system that works by emitting beams of electrons (Evlanov et al. 2013) or ions (Masek and Cohen 1978) could be used to generate and control surface charging (Lai 1989), but it must be noticed that the emission of only positive ions leads to negative potential of the spacecraft of the order of kV (Lai 1989; Masek and Cohen 1978). Because of the potential bias due to the differential charging caused by the returning particles and to the uncertainties in the definition of the return current patterns (Quadrelli et al. 2017a), charge control systems based on monoenergetic beams are not commonly used. Moreover, for the E-Glider concept, the system for generating ion beams can be bulky. Another possible method is the use of electron field emission devices (Iwata et al. 2012; Khan et al. 2013). Currently, these devices are limited to only electron emission, and they need to be hard-mounted and coupled to the surfaces to be charged. These devices can be used to imitate photoelectron emission (Quadrelli et al. 2017a) due to the low potential reached. Proper selection of the surface material could act as another simple way to generate differential charges on surfaces. Several studies on the electrical properties of the materials are available in the literature (e.g., Plis et al. 2018; Czepiela et al. 2000; Mizera 1983). This method is not well suited for the E-Glider concept, even if this is a simple and passive method, because the differential charge is strongly dependent on the environmental conditions, which can be highly variable in the scenarios that will be explored by the E-Glider. In conclusion, the last method considered to induce different potentials on different surfaces is the employment of direct biasing devices like batteries and solar cells or small Van De Graaff generators (Peck 2005). A small Van De Graaff generator seems

to be the most promising and reliable charge source to be applied to the E-Glider concept due to the possibility of generating high surface potentials (Quadrelli et al. 2017a), even if drawbacks like the presence of moving parts or the necessity of being always powered by batteries or solar cells are still present. These methods must be capable of reacting in a short time to a fast-changing external environment that can be sensed by using classic Langmuir probes mounted onboard and that could act also as electrodes to control the E-Glider dynamics.

This paper presents a unique dynamical framework behind the complex environment around an asteroid involving the interaction between irregular gravitational force, SRP force, and electrostatic force. Consequently, this research expands the possibility of flight mechanics in space. This paper concludes that electrostatic flight using an E-Glider is useful for asteroid missions and exhibits unique and valuable dynamic characteristics. Figure 2.3 shows the elements of the concept of operations for modeling and simulation of E-Glider operations: (a) the relevant dust and charge environment is modeled with high-fidelity physics codes; (b) the coupled orbital and attitude dynamics can now be modeled in this environment; (c) the local plasma conditions, combined with the E-Glider dynamics and local charge levels can new enable the process of electrostatic inflation; (d) electrostatic maneuvering is now possible; (e) circumnavigation and small-body sampling is enabled based on electrostatic hovering and orbiting; and (f) leading to new airless body science that was not possible before.

The chapter's layout is organized as follows. In Sect. 2.2, we discuss the challenges presented by the environment near an airless body. Then in the Sects. 2.3–2.7, a description of the kinematics and kinetics of electrostatic flight is presented. We consider a system composed by a small airless asteroid and an E-Glider. These sections include the derivation of the equations of motion and of attitude dynamics. The gravitational and the SRP effects equations are derived for an extended spacecraft, and the gravitational field is defined both for a spherical body and for an ellipsoidal one. The core of the dynamical modeling is the spacecraft–plasma electrostatic interaction model and the model used to define the plasma around an airless body. These topics are discussed in Sect. 2.8, where both an analytical and a numerical model of the electric field are presented, and in Sect. 2.9, where the equations for the electrostatic effects are derived. The definition and the analysis of a new class of orbits named *electrostatic periodic orbits* are carried out in Sect. 2.10 by using the Nitter model for the electrostatic field definition. In the same section, the effects of an ellipsoidal asteroid on the E-Glider orbital dynamics are evaluated. By using the same model for the electrostatic field and for the spacecraft, the attitude stability of a double-dipole spacecraft is addressed in Sect. 2.11. These two analyses are merged to investigate the coupled orbital attitude stability in Sect. 2.12. The other mode to conduct the dayside operation of the E-Glider, the fixed hovering with respect to the Sun, is investigated for a point-charge spacecraft in Sect. 2.13 by using the particle-in-cell (PIC)-described plasma field. In Sect. 2.14, a preliminary control law to switch a single-dipole and a double-dipole E-Glider from a hovering condition to another is defined and investigated, by including also a preliminary electrostatic attitude control. In regards to the power required and the potential reached by the electrodes,

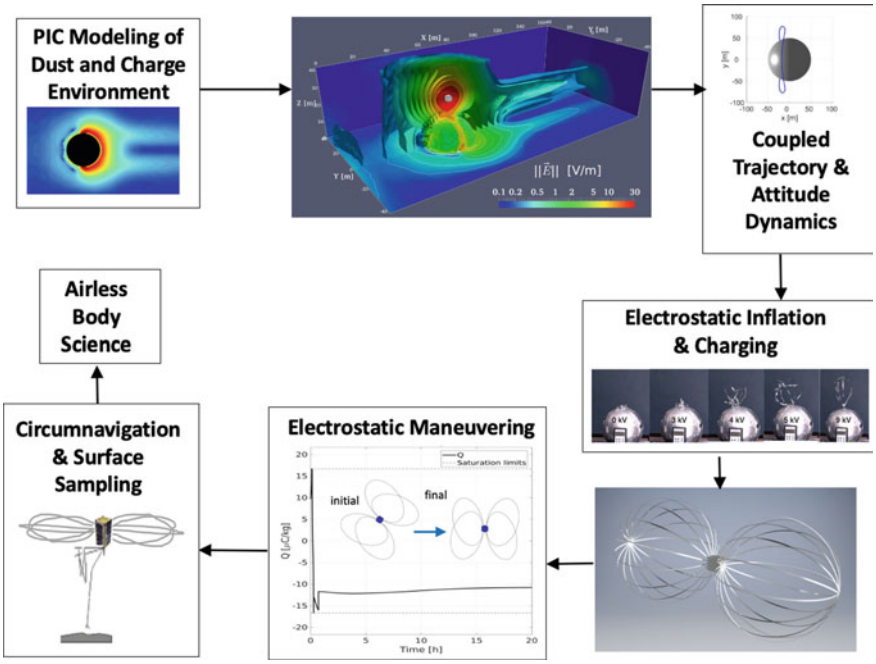

Fig. 2.3 Block diagram of the E-Glider concept of operations

Table 2.1 E-Glider concept models

S/C model	Electrodes geometry model	Plasma model	Sections
Point-charge S/C	Sphere	PIC	Section 2.13
Single-dipole S/C	Sphere	PIC	Section 2.14
Double-dipole S/C	Sphere	Nitter	Sections 2.10, 2.11, 2.12, 2.15
Double-dipole S/C	Sphere	PIC	Sections 2.14, 2.15
Double-dipole S/C	Wires (hoops)	PIC	Section 2.15

several analyses are conducted considering both the Nitter and the PIC plasma model for both the orbital and the hovering case for several electrodes geometries to identify the most promising one, and by comparing the results obtained and reported in Sect. 2.15. In conclusion, the main outcomes of this research are summarized in in Sect. 2.16 with possible future developments on the E-Glider concept.

To have an easier overview of the spacecraft models described in this work, they are summarized in Table 2.1 with the sections in which they are discussed.

2.2 Environmental Challenges at Small Bodies

The physics at airless bodies is dominated by four physical fields (Kobrick et al. 2014; Quadrelli et al. 2015): (a) microgravity, responsible for locomotion; (b) cohesion forces, which can dominate particle interactions through van der Waals forces; (c) solar radiation, which is constantly acting; and (d) electrostatics, which is strongest at the terminator where it can lead to significant dust transport. The highly irregular shapes of many asteroids and other small bodies lead to unique modeling and dynamics challenges. In contrast to the gravitational fields of spherical and ellipsoidal bodies, those produced by near-earth objects (NEOs) are frequently much more complex. The gravitational fields of these irregular bodies exhibit high levels of variation at both the surface and locations near the bodies. These gravitational fields are often orders of magnitude weaker than the Earth's. In addition to exhibiting irregular shapes, the gravitational fields produced by small bodies often have milli-G or micro-G orders of magnitude. As a result, escape velocities from these bodies are exceptionally low and must be carefully considered when maneuvering landers or spacecraft. Another consequence of these low gravitational magnitudes is that the rotational period, sometimes as fast as a fraction of a minute, may impact the motion of the spacecraft's motion. It may be possible to take advantage of this behavior to aid in motion between surface locations on a small body. This could potentially be achieved by applying an impulse to the lander such that it hops away from the surface without an orbital velocity component while the small body continues to rotate. This maneuver would lead to a change in position when gravity pulls the lander back to the surface. As the topics examined illustrate, it is necessary to understand the impacts of both small gravitational magnitudes and irregular gravitational field shapes to ensure successful spacecraft interactions with small bodies. The environment near the surface of airless bodies (asteroids, comets, moons) is electrically charged due to interactions with solar wind plasma and ultraviolet (UV) radiation. Charged dust is ever present, in the form of dusty plasma (Vladimirov 2005). Comets have a gas tail and a second electrostatic tail. This environment is also largely unexplored. Electrostatically levitating dust grains have been hypothesized to exist above tens of meters above the dayside surface (Hartzell 2012; Lee 1996). If a body with high surface resistivity is exposed to the solar wind and solar radiation, sun-exposed areas and shadowed areas become differentially charged. Charging on the dayside surface is dominated by photoelectrons emitted due to solar UV radiation that create a positive surface potential, while the shadowed side accumulates electrons and acquires a negative surface potential. Recent work Renno and Kok (2008), Stubbs et al. (2006) shows that on the Moon, soft solar X-rays with wavelengths smaller than 25 Angstroms can remove electrons with energies of 500 to 1500 eV from the surface and create cm-scale electric fields which may reach levels of $50-150\,\mathrm{kV/m}$. The spokes in Saturn's rings are most likely clouds of particles electrostatically levitated from the surfaces of larger bodies in the rings, and electrostatic dust transport processes have been proposed on the surface of Mercury (Ip 1986) and comets (Mendis et al. 1981). Asteroid electric charge has never been measured, but simple estimates

predict that an electric potential difference of 1 kV can be attained on the dark side compared to the sunlit side, which becomes slightly positively charged by photoelectron emission. These differences are enhanced further at the terminator (the day/night boundary) when fields could reach 100–300 kV/m (Aplin et al. 2011) (with results obtained by simulation). Millimeter-size particles can be most easily lifted from the surface of Itokawa (Hartzell 2012). As these particles are lifted, they dislodge smaller particles that are harder to lift due to their strong cohesive forces. Once separated from the surface, grains can either travel on ballistic trajectories, escape from the asteroid, or levitate. During these migrations, the larger particles can get trapped in topographic lows, as observed in Miyamoto (2007). As a surface element on a resistive asteroid rotates in and out of view of the Sun, electrostatic levitation may agitate its uppermost particulate layer. Larger levitated particles remaining gravitationally bound to the asteroid are redistributed across its surface following local electrostatic and gravity gradients. Consequently, the study of levitating dust is relevant in that it provides some insight into the plasma environment and confirms the possibility of levitation. An intriguing example from nature discussed in Gorham (2013) refers to existing observations and the physics of spider silk in the presence of the Earth's static atmospheric electric field (–120 V/m negative) to indicate a potentially important role for electrostatic forces in the flight of gossamer spiders. A compelling example is analyzed in detail, motivated by the observed "unaccountable rapidity" in the launching of such spiders from the vessel H.M.S. Beagle, recorded by Charles Darwin during his famous voyage, on a day without wind, and far away from the shore. It is believed that such spiders can emit threads that are either preloaded with a static electric charge so that the presence of this charge will lead both to mutual repulsion among the emitted threads, and an additional overall induced electrostatic force on the spider, providing a component of lift that is independent of convection or aerodynamic effects. The E-Glider biomorphically behaves like one of these spiders, greatly favored by the charged environment, in absence of aerodynamics and convection, and in the microgravity fields at small bodies.

2.3 Kinematics

The definition of the notation and the reference frames used is necessary to correctly understand the dynamic models and the equations of motion explained in the following paragraphs. The notation used to express the vectors and the matrices in the different reference frames is the following:

- ${}^{a}\mathbf{x}$ stands for a vector or a tensor $\mathbf{x}$ expressed in the a-frame
- ${}^{a}\omega_{bc}$ stands for the angular velocity of c frame with respect to b frame expressed in the a frame
- ${}^{a}\mathbf{R}_{b}$ stands for the rotation matrix (or tensor) $\mathbf{R}$ which converts ${}^{b}\mathbf{x}$ into ${}^{a}\mathbf{x}$, thus ${}^{a}\mathbf{x} = {}^{a}\mathbf{R}_{b}\,{}^{b}\mathbf{x}$

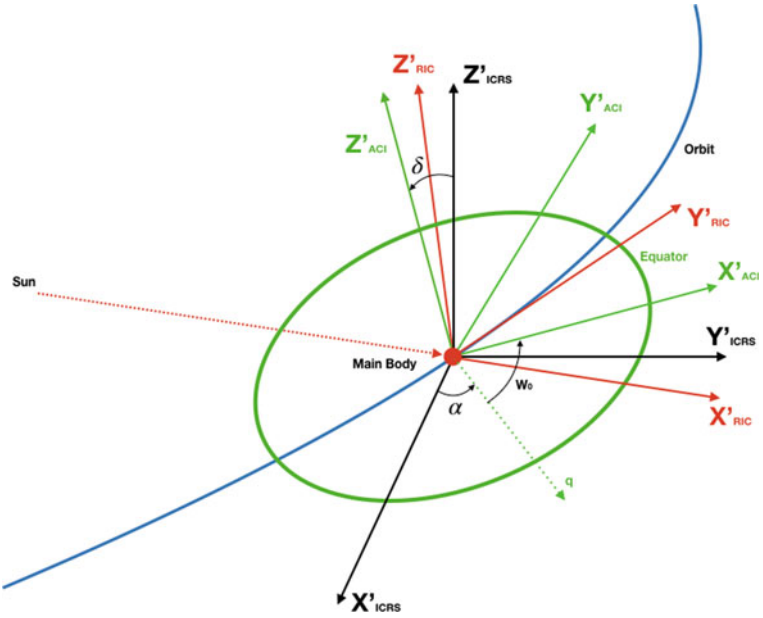

Fig. 2.4 Main body-centered reference frames: asteroid-centered inertial (ACI) and radial/in-track/cross-track (RIC)

2.3.1 Main Body-Centered Reference Frames

- Radial/in-track/cross-track (RIC) frame: r

The radial/in-track/cross-track (RIC) reference frame is the reference frame used to write the translation equations of motion. This is a non-inertial reference frame.

The RIC frame is defined as (see Fig. 2.4):

- O = origin at the main body center of mass
- X = axis directed away from the solar system barycenter (e.g., along the radial direction)
- Y = axis lying on the orbital plane and completing the right-handed orthogonal frame (e.g., along the in-track direction)
- Z = axis parallel to the orbital angular momentum vector (e.g., along the cross-track direction)

The RIC can be derived from the perifocal reference frame by translating it from the barycenter of the solar system to the main body center of mass and then by applying a rotation equal to the true anomaly of the main body.

$$^{r}\mathbf{R}_{p} = [\Theta(t)]_3 \tag{2.1}$$

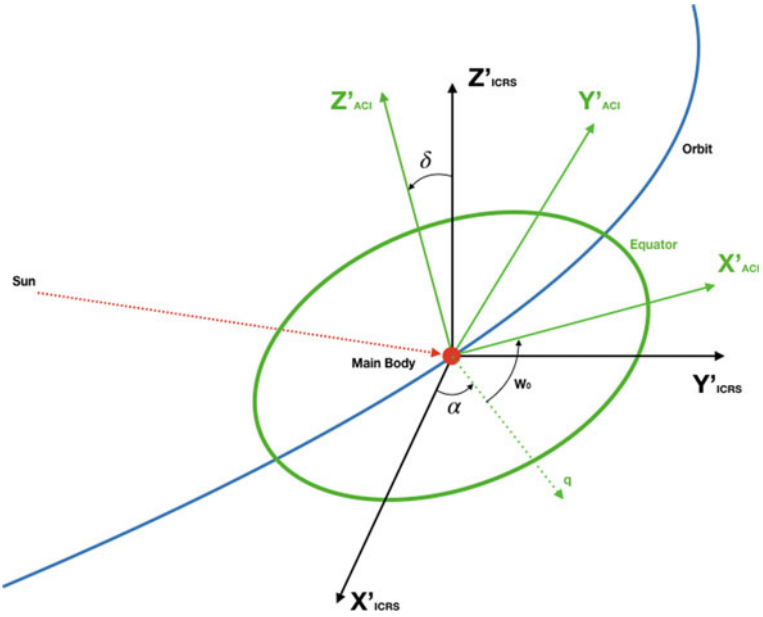

Fig. 2.5 ACI reference frame

- Asteroid-centered inertial (ACI) frame: a
  The Asteroid-Centered Inertial (ACI) reference frame helps to define the attitude and the rotations of both the spacecraft and the Main Body. This reference frame can be assumed to be inertial when the attitude refers to it (the non-inertial components are due to translation).

This reference frame can be defined as (see Fig. 2.5):

- O = origin at the main body center of mass
- X = axis lying on the equator and pointing towards the prime meridian at the reference epoch
- Y = axis lying on the equator and completing the right-handed orthogonal frame
- Z = axis directed as the main body rotation angular momentum vector

The ACI reference frame can be derived by translating the international celestial reference frame on the main body and then rotating it as

$$^{a}\mathbf{R}_{i} = [W_0]_3[\delta]_1[\alpha]_3 \tag{2.2}$$

where W_0 is the position of the prime meridian at a given epoch, δ is the declination of the positive pole, and α is the right ascension of the positive pole (see Fig. 2.5).

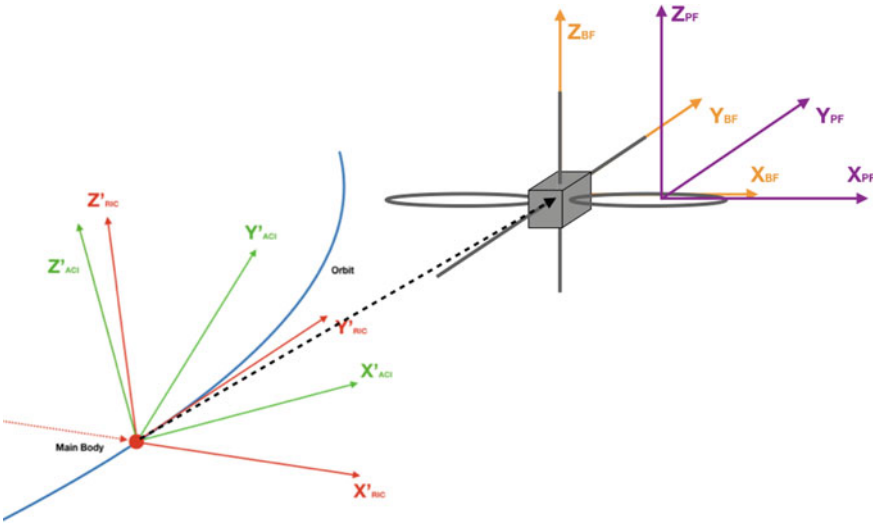

Fig. 2.6 Spacecraft-centered reference frames: body-fixed (BF) and post-fixed (PF)

2.3.2 Spacecraft-Centered Reference Frames

- Body-fixed (BF) frame: b
  The body-fixed (BF) reference frame is rigidly "attached" to the spacecraft. The propagation of the attitude equations of motion is carried out in this reference frame. We assumed the attitude and the rotation rates considered as expressed in the BF frame and related to the ACI frame.

The definition of the BF reference frame is (see Fig. 2.6) as follows:

- O = origin at the spacecraft center of mass
- Axes = defined by the geometry of the spacecraft (usually oriented towards the principal axes of inertia)

The attitude quaternion ${}^{b}\mathbf{q}_{a}$ defines the orientation with respect to the ACI frame.

2.4 Linearized Equations of Motion for Translational Motion

In the ensuing paragraph, we derive the equations of motion both for the case of the Clohessy–Wiltshire formulation, suitable for a main body with almost circular orbits, and for the case of the more accurate "full dynamic" formulation, which can be applied also to asteroids that are on orbits with high eccentricity.

The linearized equations of motion are obtained by considering the main body as a target and the E-Glider as the chaser, while the Sun is the third body in the full model case. The derivation of the equations of motion is in the RIC reference frame; thus, the distance of the target from the Sun and both the angular velocity and the angular acceleration with respect to the Sun are needed to derive the correct formulation. We assume the case of "proximity flight" (Scheeres and Marzari 2002) in the derivation of the equations of motion; thus, the distance of the spacecraft from the Sun and the distance of the main body from the Sun are comparable, and the distance of the spacecraft from the main body is much less than the previous two distances. By knowing the Keplerian parameters of the main body orbit around the Sun and $\theta = \theta(t)$, the equations applied in the computation of the distance d of the main body from the Sun, and the instantaneous asteroid orbital angular velocity and angular acceleration $\dot{\theta}$ and $\ddot{\theta}$ are

$$d = \frac{h_a^2}{\mu_s} \cdot \frac{1}{1 + e_a cos\theta} = \frac{P_a}{1 + e_a cos\theta} \tag{2.3}$$

$$\dot{\theta} = \frac{h_a^2}{d^2} = \frac{\sqrt{P_a \mu_s}}{d^2} \tag{2.4}$$

$$\ddot{\theta} = -2\sqrt{\frac{\mu_s}{P_a}} \cdot \frac{e_a sin\theta\dot{\theta}}{d} = -2\frac{e_a \dot{\theta}^2 sin\theta}{1 + e_a cos\theta} \tag{2.5}$$

The angular velocity vector of the main body about the Sun is $\mathbf{\Omega}$, and it has a constant direction taken to be in the Z-direction in the perifocal (PQW) frame; thus, $\mathbf{\Omega}$ is also the angular velocity of the RIC frame with respect to the PQW frame. The magnitude of $\mathbf{\Omega}$ follows Eq. (2.4). Moreover, ${}^r\mathbf{\Omega} = (0, 0, \dot{\theta})$ and ${}^r\dot{\mathbf{\Omega}} = (0, 0, \ddot{\theta})$ can be easily verified. We need the spacecraft acceleration in the RIC frame to write the translational equation of motion in this reference frame. Let $\mathbf{r}$ be the position vector of the spacecraft with respect to the main body, while $\mathbf{D}_s$ and $\mathbf{D}_a$ are the position vectors of the spacecraft with respect to the Sun and of the main body with respect to the Sun, respectively, as shown in Fig. 2.7. By knowing that $\mathbf{D}_s = \mathbf{D}_a + \mathbf{r}$, the absolute acceleration can be obtained after some mathematical steps as (Curtis 2010):

$$\ddot{\mathbf{D}}_s = \ddot{\mathbf{D}}_a + \mathbf{a} + \dot{\mathbf{\Omega}} \times \mathbf{r} + \mathbf{\Omega} \times \mathbf{\Omega} \times \mathbf{r} + 2\mathbf{\Omega} \times \mathbf{v} \tag{2.6}$$

where $\mathbf{r}$, $\mathbf{v}$, and $\mathbf{a}$ are in the RIC frame. $\dot{\mathbf{\Omega}} \times \mathbf{r}$ is the term related to the angular acceleration of the frame, while $\mathbf{\Omega} \times \mathbf{\Omega} \times \boldsymbol{r}$ and $2\mathbf{\Omega} \times \mathbf{v}$ are the centrifugal term and the Coriolis accelerations, respectively. By solving Eq. (2.6) for the relative acceleration $\mathbf{a}$ in the RIC frame and by knowing that $\ddot{\mathbf{r}} = \ddot{\mathbf{D}}_s - \ddot{\mathbf{D}}_a$, it results that

$$\mathbf{a} = {}^p\ddot{\mathbf{r}} - \dot{\mathbf{\Omega}} \times \mathbf{r} - \mathbf{\Omega} \times \mathbf{\Omega} \times \mathbf{r} - 2\mathbf{\Omega} \times \mathbf{v} \tag{2.7}$$

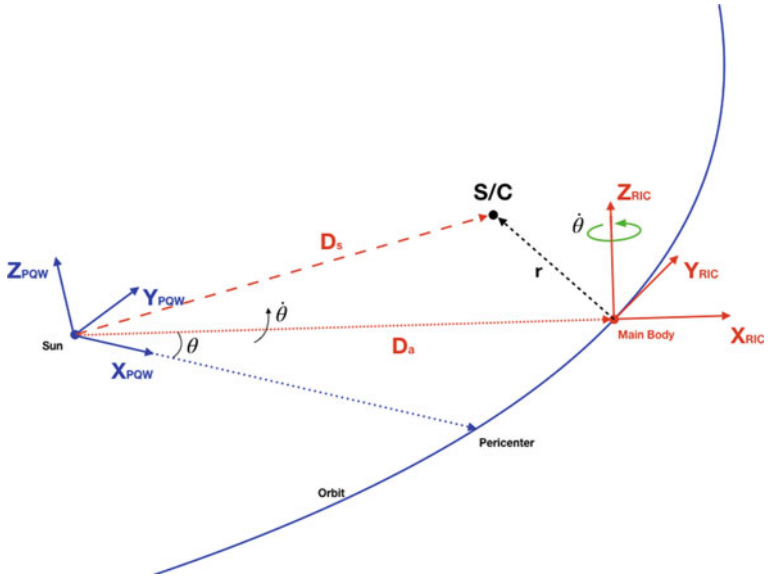

Fig. 2.7 Full model reference frames and vectors

The vector ${}^{p}\ddot{\mathbf{r}}$ measured in the inertial frame must be computed to define the relative acceleration in the RIC frame (the comoving one). To do that, a linearized model that is valid since $r \ll D_s, D_a$ can be used. By recalling that $\ddot{\mathbf{D}}_a = -\frac{\mu_s}{D_a^3}\mathbf{D}_a$, the equations of motion of the chaser relative to the target measured in the PQW inertial frame can be derived after some mathematical steps, assuming negligible the higher-order terms, as

$$\ddot{\mathbf{r}} = -\frac{\mu_s}{D_a^3}\left[\mathbf{r} - \frac{3}{D_a^2}\left(\mathbf{D}_a \cdot \mathbf{r}\right)\mathbf{D}_a\right] \tag{2.8}$$

By expressing $\mathbf{r}$ and $\mathbf{D}_a$ in the comoving RIC frame and by substituting the result into Eq. (2.7), the equation of motion for the translation for the full model in the RIC frame can be obtained by introducing the term $\frac{{}^{r}\mathbf{f}}{M}$, which gives the effects of the active forces acting on the spacecraft. Hence,

$${}^{r}\mathbf{a} = \frac{{}^{r}\mathbf{f}}{M} - \frac{\mu_s}{d^3}\begin{bmatrix}-2r_x\\+r_y\\+r_z\end{bmatrix} + \ddot{\theta}\begin{bmatrix}r_y\\-r_x\\0\end{bmatrix} + \dot{\theta}^2\begin{bmatrix}+r_x\\+r_y\\0\end{bmatrix} + 2\dot{\theta}\begin{bmatrix}+v_y\\-v_x\\0\end{bmatrix} \tag{2.9}$$

$${}^{r}\dot{\mathbf{r}} = {}^{r}\mathbf{v} \tag{2.10}$$

For the purposes of this work, the main body gravitational perturbation effects, the Solar radiation pressure force, and the spacecraft electrostatic interactions with the

plasma field are considered. The effects of the magnetic field $\boldsymbol{B}$ of both the asteroid and the Sun have been neglected in the following analyses by assumptions.

The Clohessy–Wiltshire formulation can be derived by assuming the target (the main body) to be on a circular unperturbed orbit around the third body (the Sun). This strong assumption allows to consider the mean motion of the main body as constant, hence $\dot{\theta} = N = \text{const}$. Moreover, $e = 0$ for a circular orbit; thus, the angular momentum can be written as $h_a = \sqrt{\mu_s D_a}$. By using these relations and by knowing that since $N = \text{const}$, the term related to $\dot{\Omega}$ is null, and the first cardinal equation in the RIC frame (Eq. (2.9)) can be rewritten by using the Clohessy–Wiltshire approximation as follows:

$$ {}^{r}\mathbf{a} = \frac{{}^{r}\mathbf{f}}{M} + 2N \begin{bmatrix} +v_y \\ -v_x \\ 0 \end{bmatrix} + N^2 \begin{bmatrix} +3r_x \\ 0 \\ -r_z \end{bmatrix} \tag{2.11} $$

$$ {}^{r}\dot{\mathbf{r}} = {}^{r}\mathbf{v} \tag{2.12} $$

2.5 Attitude Dynamics

The equation of motion for the attitude is the classical Euler's equation used for attitude propagation. This equation can be derived from the momentum equation written in an inertial reference frame. The Euler's equation in the BF frame is

$$ {}^{b}\boldsymbol{J}^{b}\dot{\boldsymbol{\omega}}_{ab} = {}^{b}\boldsymbol{J}^{b}\boldsymbol{\omega}_{ab} \times {}^{b}\boldsymbol{\omega}_{ab} + {}^{b}\mathbf{T} \tag{2.13} $$

${}^{b}\boldsymbol{\omega}_{ab}$ is the angular rate of the BF frame (thus the spacecraft angular rate) with respect to the inertial reference frame (ACI) expressed in the BF reference frame. The term ${}^{b}\mathbf{T}$ collects all the active torques applied to the spacecraft expressed in the BF reference frame. The active torques are given by the gravity field of the main body, the solar radiation pressure torque, and the electrostatic effects. The attitude dynamics equation must be completed by adding also the attitude kinematics. We used the quaternion representation in this work; thus, the quaternion kinematics equation can be written as

$$ {}^{b}\dot{\boldsymbol{q}}_{a} = \frac{1}{2} \begin{bmatrix} {}^{b}\boldsymbol{\omega}_{ab} \\ 0 \end{bmatrix} \otimes {}^{b}\mathbf{q}_{a} \tag{2.14} $$

Here, ${}^{b}\mathbf{q}_{a}$ is the attitude quaternion from the ACI to BF reference frame, and the symbol $\otimes$ stands for the quaternion products. The quaternion must be normalized after each integration step in order to avoid divergences.

2.6 Gravitational Forces and Moments

Two different gravity field models have been considered, the classical and simple point mass gravity model and a more complex and accurate model based on the spherical harmonics expansion model.

2.6.1 Point Mass Gravity Model

The point mass gravity model is suitable for bodies with a spherical/symmetric mass distribution. If we can assume that the mass of the main body is concentrated in the center of gravity of the body itself, then the point mass gravity model is valid. This model is singularity-free, and its computational cost is extremely low, such that the point mass gravity model can be used for feasibility studies and first approximation analysis. $\mathbf{f}_g$, the gravitational force acting on the spacecraft, can be simply derived by knowing that the gravitational force is conservative. Thus, the gravitational acceleration is $\mathbf{a}_g = \nabla U$, where U is the gravitational potential; thus, it results to be

$$\mathbf{a}_g = -\frac{\mu}{r^3}\mathbf{r} \tag{2.15}$$

The formulation for the gravity gradient tensor $\mathbf{G}_g$ is the following (Gottlieb 1993):

$$\mathbf{G}_g = \nabla \mathbf{a}_g = -\frac{\mu}{r^3}\left(\mathbf{I} - \frac{3}{r^2}\mathbf{r} \otimes \mathbf{r}\right) \tag{2.16}$$

Notice that the symbol $\otimes$ stands for the outer product.

2.6.2 Spherical Harmonics Model

The expansion in spherical harmonics of the gravitational field is a commonly used method to compute the gravitational potential U_g. This method offers the possibility to compute the tangential components of the gravitational and to achieve an accuracy level higher than the point mass model without introducing an excessively high computational load (e.g., as the FE MASCON method). For the analysis of an E-Glider, the terminator region can be of particular interest; thus, a singularity-free method is mandatory for the computation of the gravity field also at the poles. There are several singularity-free methods; the one used here is the method developed by Pines in 1973 (Pines 1973) due to its accuracy and fast computational capabilities. A modified recursion formula is needed for the computation of the Legendre polynomials to also achieve the stability required for high-order gravitational models since the one

originally proposed by Pines was unstable for high n (Eckman et al. 2011; Lundberg 1988). Hence, the gravitational potential can be rewritten as

$$U_g = \sum_{n=0}^{\infty} \rho_n \sum_{m=0}^{n} A_{n,m}(u) D_{n,m}(s,t) \tag{2.17}$$

The definition of ρ_n is Pines (1973) (see Eq. (2.26)) and $D_{n,m}(s,t)$ is a mass coefficient function. Equation (2.17) must be differentiated in Pines' reference frame in order to compute the gravitational acceleration $\mathbf{a}_g$; thus, the equations for the gravitational acceleration and for the gravity gradient tensor are

$$\mathbf{a}_g = \nabla U_g = a_1 \hat{\mathbf{i}} + a_2 \hat{\mathbf{j}} + a_3 \hat{\mathbf{k}} + a_4 \hat{\mathbf{r}} \tag{2.18}$$

$$\mathbf{G}_g = \nabla \mathbf{a}_g = \frac{\partial}{\partial \mathbf{r}} \left(a_1 \hat{\mathbf{i}} + a_2 \hat{\mathbf{j}} + a_3 \hat{\mathbf{k}} + a_4 \hat{\mathbf{r}} \right) \tag{2.19}$$

The equations to compute both the coefficients of Eq. (2.18) and the derived coefficients of Eq. (2.19) simply and efficiently are available in Pines (1973).

2.6.3 *Forces and Torques on an Extended Body*

The computation of both the gravitational forces and the gravitational torques acting on the spacecraft is mandatory, independently from the model assumed. The local acceleration $\mathbf{a}_g(\mathbf{r})$ and the local gravity gradient $\mathbf{G}_g(\mathbf{r})$ components can be computed as explained in the previous section.

In the analysis, the spacecraft can be considered or as an extended single body (hence with a single mass and a single inertia), or as an ensemble of parts (multibody approach) with their own mass localized at the center of gravity of the part itself. A linear model can be assumed for the case of a satellite modeled as an extended body. In this case, the vector $\boldsymbol{\rho} = \mathbf{r} - \mathbf{r}_0$, in which $\mathbf{r}_0$ is the position of the center of mass, gives the position of a point with respect to the center of mass of the spacecraft; thus, the approximated equation for the gravitational acceleration is

$$\mathbf{a}_g(\mathbf{r}) = \mathbf{a}_g(\mathbf{r}_0) + \mathbf{G}_g(\mathbf{r}_0)\boldsymbol{\rho} \tag{2.20}$$

By integrating Eq. (2.20) and by remembering that $\int_{S/C} \boldsymbol{\rho} dM$ is the first moment of mass about the center of mass itself, hence null by definition, the gravitational force results to be

$$\mathbf{f}_g = \mathbf{a}_g(\mathbf{r}_0) M \tag{2.21}$$

In the case of a spacecraft modeled as an ensemble of parts, the total gravitational force acting on the whole spacecraft can be computed as the summation of the forces acting on each part constituting the spacecraft; thus, by referring with the index i to the i-th part, the gravitational force is

$$\mathbf{f}_g = \sum_i \left(\int_{\text{i-th part}} \mathbf{a}_g(\mathbf{r}_i) dM_i \right) = \sum_i \left(\mathbf{a}_g(\mathbf{r}_i) M_i \right) \tag{2.22}$$

where $\mathbf{r}_i$ and M_i are the position of the center of mass and the mass of the i-th part, respectively. This method has a stronger impact on the computational load with respect to the previous one, but it allows us to achieve a higher level of precision for highly extended bodies (where the linearized model of the first case is no more valid).

For the case of a single extended body, by using the very same assumptions of the previous paragraph, the equation for the gravity torque is

$$\mathbf{T}_g = \int_{S/C} \boldsymbol{\rho} \times (\mathbf{a}_g(\mathbf{r}_0) + \mathbf{G}_g(\mathbf{r}_0)\boldsymbol{\rho}) dM \tag{2.23}$$

By remembering that, once again, $\int_{S/C} \boldsymbol{\rho} dM$ is the first moment of mass about the center of mass itself, hence null by definition, we can obtain

$$\mathbf{T}_g = \int_{S/C} \boldsymbol{\rho} \times \mathbf{G}_g(\mathbf{r}_0) dM \tag{2.24}$$

The total torque for the case of a spacecraft made by several parts can be expressed as the sum of the torques given by the gravitational forces acting on each part i, resulting in

$$\mathbf{T}_g = \sum_i \left(\int_{\text{i-th part}} \boldsymbol{\rho}_i \times \mathbf{a}_g(\mathbf{r}_i) dM_i \right) = \sum_i \left(\boldsymbol{\rho}_i \times \mathbf{a}_g(\mathbf{r}_i) M_i \right) \tag{2.25}$$

where $\boldsymbol{\rho}_i$ is the position of a point of the i-th part with respect to the center of mass of the i-th part itself. As before, this method is both more precise and more expensive from the computational point of view.

2.6.4 Irregular Asteroid Model

The asteroid is modeled as a homogeneous triaxial ellipsoid with semimajor axes R_a, R_b, and R_c ($R_a \geq R_b \geq R_c$). The mean radius of the asteroid is given as $R = 50\,\text{m}$, which satisfies $R^3 = R_a R_b R_c$, and the axis ratio is taken as a variable in later subsections. The asteroid is rotating uniformly about the shortest axis with the rotation period of $T_{rot} = 8\,\text{hr}$, and the rotation axis is assumed to be perpendicular to

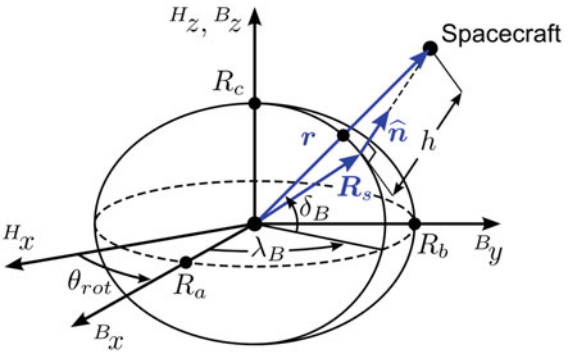

Fig. 2.8 Reference frames around an ellipsoidal asteroid

the ecliptic plane (Kryszczyńska et al. 2007). Then the asteroid body-fixed coordinate can be defined as shown in Fig. 2.8. Here, a left superscript "H" represents the Hill coordinate system, and "B" represents the asteroid body-fixed frame. The ${}^H z$ axis and ${}^B z$ are identical because of the assumption regarding the rotation axis. Henceforth, the position of a spacecraft is expressed in terms of the Hill coordinate as ${}^H \boldsymbol{r} = [x, y, z]^{\mathrm{T}}$ and in terms of the asteroid body-fixed frame as ${}^B \boldsymbol{r} = [x_B, y_B, z_B]^{\mathrm{T}}$.

Let ${}^H \boldsymbol{C}_B$ denote the rotational transformation matrix from the asteroid body-fixed coordinate to the Hill coordinate system. Then the coordinate transformation for an arbitrary state vector $\boldsymbol{u}$ is expressed as ${}^H \boldsymbol{u} = {}^H \boldsymbol{C}_B {}^B \boldsymbol{u}$, where ${}^H \boldsymbol{C}_B$ is given by the equation below.

$$ {}^H \boldsymbol{C}_B = \begin{bmatrix} \cos\theta_{rot} & -\sin\theta_{rot} & 0 \\ \sin\theta_{rot} & \cos\theta_{rot} & 0 \\ 0 & 0 & 1 \end{bmatrix} \tag{2.26} $$

Here, θ_{rot} is the rotation phase of an asteroid and given as a function of time by the following equation:

$$ \theta_{rot} = \frac{2\pi}{T_{rot}} t \tag{2.27} $$

2.6.5 *Irregular Gravitational Field*

The gravitational potential of an asteroid is calculated based on a triaxial ellipsoid model. The gravitational coefficients C_{mn} of its spherical harmonics expansion up to the fourth order are defined by the following equations (Scheeres 2012):

$$
\begin{aligned}
C_{20} &= \frac{1}{10R_a^2}\{2R_c^2 - (R_a^2 + R_b^2)\} \\
C_{22} &= \frac{1}{20R_a^2}(R_a^2 - R_b^2) \\
C_{40} &= \frac{15}{7}(C_{20}^2 + 2C_{22}^2) \\
C_{42} &= \frac{5}{7}C_{20}C_{22} \\
C_{44} &= \frac{5}{28}C_{22}^2
\end{aligned}
\tag{2.28}
$$

Using these coefficients, the gravitational potential is given by the equation below.

$$
\begin{aligned}
U_G = \frac{\mu}{r}\Bigg[1 &+ \left(\frac{R}{r}\right)^2\left\{\frac{1}{2}C_{20}(3\sin^2\delta_B - 1) + 3C_{22}\cos^2\delta_B\cos 2\lambda_B\right\} \\
&+ \left(\frac{R}{r}\right)^4\left\{\frac{1}{8}C_{40}(35\sin^4\delta_B - 30\sin^2\delta_B + 3)\right. \\
&\left.+\frac{15}{2}C_{42}\cos^2\delta_B(7\sin^2\delta_B - 1)\cos 2\lambda_B + 105C_{44}\cos^4\delta_B\cos 4\lambda_B\right\}\Bigg]
\end{aligned}
\tag{2.29}
$$

where δ_B and λ_B denote the latitude and longitude, respectively, defined in terms of the asteroid body-fixed frame. The relation between (δ_B, λ_B) and the position of a spacecraft can be expressed as follows:

$$
\begin{aligned}
\delta_B &= \sin^{-1}\left(\frac{z_B}{r}\right) \\
\lambda_B &= \tan^{-1}\left(\frac{y_B}{x_B}\right)
\end{aligned}
\tag{2.30}
$$

Then from Eq. (2.29), the gravitational acceleration from an ellipsoidal asteroid can be obtained.

2.6.6 *Gravitational Torque*

The gravitational torque $\mathbf{T}_G$ can be expressed as follows by applying the Taylor series expansion (Hughes 1986):

$$
\mathbf{T}_G \simeq \frac{3\mu}{r^5}\mathbf{r} \times \mathbf{Ir} \tag{2.31}
$$

It is important to note that both the gravity gradient torque and the electrostatic torque are dependent on the position of a spacecraft with respect to a small body, and therefore the orbital motion of a spacecraft exerts an influence on its attitude motion.

2.7 Solar Radiation Forces and Moments

The exchange of momentum between the photons and a surface results in solar radiation pressure. Each source of electromagnetic radiation has an effect on a solid surface, but the pressure given by the solar radiation is predominant at 1 AU (Lyon 2004); thus, the other terms are negligible in this analysis. In a macro-model approach, the incident radiation on a surface can be either absorbed, specularly reflected, or diffusely reflected (by assuming no transmission of radiation through the spacecraft). In the following, dA is the surface area with normal $\hat{\mathbf{n}}$ subjected to the incident flux Φ. The incident flux has an inclination α with respect to the normal $\hat{\mathbf{n}}$. The versor $\hat{\mathbf{s}}$ points towards the origin of the radiation. The summation of the three forces given by the absorption, the specular reflection, and the diffusive reflection of the incoming radiation gives the total resultant force over a flat surface dA:

$$d\mathbf{f}_p = d\mathbf{f}_{ps} + d\mathbf{f}_{pd} + d\mathbf{f}_{pa} = -\frac{\Phi}{c} dA cos\alpha \left[\left(2C_{ps} cos\alpha + \frac{2}{3} C_{pd} \right) \hat{\mathbf{n}} + \left(C_{pd} + C_{pa} \right) \hat{\mathbf{s}} \right] \quad (2.32)$$

The two models suitable for the computation of the solar radiation pressure effects are the cannonball model and the backward ray-casting model.

2.7.1 Cannonball Model

The cannonball model is a classical simplified approach to compute the resultant force and torque over the external surfaces of a spacecraft. The spacecraft can be approximated by a sphere of equivalent external area and with constant thermo-optical properties as an assumption of this model. The incoming flux of electromagnetic radiation is incident over the cross-sectional area, such that the total force results to be

$$\mathbf{f}_p = -\frac{\Phi}{c} \pi R^2 \left(C_{ps} + \frac{13}{9} C_{pd} + C_{pa} \right) \hat{\mathbf{s}} \quad (2.33)$$

With this model, the determination of the resulting torque is not possible (indeed $\mathbf{T}_p = 0$).

2.7.2 Backward Ray-Casting Model

This method relies on the generation of rays on the surfaces of the spacecraft. The propagation of these rays in the backward direction allows us to check if there are intersections and shadowing between surfaces. The spacecraft surfaces must be approximated as an ensemble of large arrays made by small "facets" to apply this method. Each facet acts as a source for a single ray; thus, if the facets are small enough, the total force can be computed as a summation instead of solving the integral over the entire surface. If $\hat{\mathbf{s}} \cdot \hat{\mathbf{n}} < 0$, the facet is certainly in shadow; hence, the ray and the facet can be discarded immediately from the computation.

A ray-casting intersection algorithm is needed to evaluate the rays that intercept one surface before reaching another one. The contribution must be discarded after the first intersection. The degree of precision depends on the number of facets used. The higher the number of facets, the higher the precision, but also the higher the computational cost. If thin wires or, more in general, thin features are present, the aliasing may arise (as in the case of forward ray casting), but the error introduced is usually not significant.

2.8 Plasma and Charging Interactions Around Small Asteroids

Without a global magnetic field, airless bodies such as asteroids are exposed directly to solar radiation, and space plasmas are thus electrically charged. To calculate the electrostatic force applied to an E-Glider, the plasma environment around an asteroid and the interactions between the E-Glider, asteroid, and plasma must be modeled appropriately. This section discusses such interactions and relevant modeling studies.

2.8.1 Plasma and Charging Environments Around Small Asteroids

Asteroids have a wide range of size. Typical near-earth asteroids (NEAs) have a size distribution from 1 m to ∼32 km. Most asteroids are irregular shaped and show significant macroporosity (Clark et al. 2002). Many asteroids are covered by a regolith layer, similar to the Moon. An asteroid is a dielectric object. While few direct measurements of asteroids' surface properties are currently available, one expects that the conductivity and dielectric constant of an asteroid's surface would be similar to that of the lunar surface, which are estimated to be 10^{-14}S/m - 10^{-9}S/m and 2–10, respectively (Olhoeft and Strangway 1975).

Solar wind (SW) is a mesothermal plasma (the directed plasma flow speed is larger than ion thermal speed but less than electron thermal speed). While the solar wind

plasma parameters can undergo substantial change, the parameters under the average solar wind condition at 1 AU relevant to this study are plasma density $n_0 \sim 5\,\mathrm{cm}^{-3}$; solar wind flow speed $V_{sw} \sim 400$ km/s; and solar wind electron temperature $T_e \sim 10$ eV. Based on these parameters, the solar wind Debye length is $\lambda_D \sim 10.5$ m, the ambient solar wind proton flux density is $\Gamma_{i0} \sim n_0 V_{sw} \simeq 2 \times 10^8\,\mathrm{cm}^{-2}\mathrm{s}^{-1}$ (current density $J_{i0} \sim 0.32\,\mu\mathrm{A/m}^2$), and the ambient solar wind electron flux density is $\Gamma_{e0} \sim n_0\sqrt{kT_e/m_e} \simeq 6.6 \times 10^8\,\mathrm{cm}^{-2}\mathrm{s}^{-1}$ (current density $J_{e0} \sim 1\,\mu\mathrm{A/m}^2$). Since the mean-free-path in the solar wind is typically on the order of 1 km or 10 s, the plasma flow around small asteroids (size smaller than 1km) can be considered collisionless.

Photoelectron emissions occurs at a sunlit surface. The photoelectron temperature is $T_{ph} \sim 2.2$eV. Under normal sunlight incidence at 1 AU, the photoelectron flux density is $\Gamma_{ph0} \sim n_{ph0}\sqrt{kT_{ph}/m_e} \simeq 39.8 \times 10^8\,\mathrm{cm}^{-2}\mathrm{s}^{-1}$ (current density $J_{ph0} \sim 6.4\,\mu\mathrm{A/m}^2$), the number density is $n_{ph0} \sim 64\,\mathrm{cm}^{-3}$, and the photoelectron Debye length is $\lambda_{D,ph0} \sim 1.38$ m. The photoelectron number density at the asteroid surface as a function of the local sun elevation angle α is $n_{ph}(\alpha) = n_{pho}\sin\alpha$. For surfaces with a small Sun incidence angle, the photoelectron Debye length would be significantly larger than $\lambda_{D,ph0}$, and the photoelectron flux density significantly smaller than Γ_{ph0} due to reduced photoelectron emission.

An asteroid in a mesothermal solar wind flow forms a plasma wake behind it in which only mobile electrons can penetrate (Fig. 2.14 Wang and Hastings 1992; Wang and Hu 2018). Since only the electrons can impinge on the dark side of the body, the wake side surface will charge negatively until the local electric field is strong enough to repel all impingement electrons. Depending on the solar wind condition, the potential on the dark side can thus reach negative values of tens to several hundreds of volts (Fig. 2.15) (Lee 1996; Mendis et al. 1981). On the sunlit side, while both ions and electrons can strike the surface, surface charging is mostly dominated by photoelectron emission. The emitted photoelectrons cause the surface to accumulate positive charges until its potential is high enough to impair photoelectron emission itself. The potential of the sunlit surface is therefore on the order of the photoelectron temperature, i.e., a few volts. One notes that the combined effects from the plasma flow and localized sunlit/shadow region on the asteroid surface can generate a complex plasma flow field around asteroids and differential charging on the asteroid surface.

Many studies have been carried out to investigate the interactions between asteroids and solar wind plasma and the dynamics of charged dust grains (Lee 1996; Nitter et al. 1998; Colwell et al. 2005; Han and Wang 2019; Yu et al. 2019). In this section, both analytical modeling and numerical simulations will be presented. Nitter in Nitter et al. (1998) carried out an analytical derivation of the mono-dimensional plasma sheath around an asteroid. From Nitter et al. (1998), we first derived a multi-sheath model that has been used also for preliminary study on the E-Glider concept (Quadrelli et al. 2017a, b; Kikuchi 2017). This derived model was obtained by relaxing some hypotheses (Hartzell 2012) and by including the effects of drifting electrons (Jeong 2008). The analytical approach is not capable of solving the equa-

tions for nonelementary cases unless strong assumptions and simplifications are taken into account (Corradino 2018). Hence, numerical simulations based on fully kinetic particle-in-cell (PIC) simulations are also carried out to obtain the electric field around small asteroids.

2.8.2 *Analytical Modeling of the Plasma and the Electric Field*

We first present a simplified analytical analysis. The relationship between particle densities and the electrostatic potential is described by Poisson's equation. Given that the asteroid has a spherical shape and the particle distribution is symmetrical about the subsolar line, the electrostatic potential is expressed as a function of the altitude h and the solar incident angle θ defined by the equations below.

$$\begin{aligned} h &= r - R \\ \theta &= \cos^{-1}\left(-\frac{x}{r}\right) \end{aligned} \tag{2.34}$$

Here, $R = D/2$ is the radius of an asteroid. Then the electrostatic potential around the asteroid is modeled using the following Poisson equation, which is expressed as a second-order differential equation in terms of h (Nitter et al. 1998; Jeong 2008; Hartzell 2012):

$$\frac{\partial^2 \phi(h,\theta)}{\partial h^2} = -\frac{e}{\varepsilon_0}(n_i - n_e - n_p) \tag{2.35}$$

where e is the elementary charge; ε_0 is the vacuum permittivity; and n_i, n_e, and n_p are number densities of the solar wind ions, the solar wind electrons, and the photoelectrons, respectively. Assuming that the solar wind ions are modeled as a mono-energetic beam, and that the solar wind electrons and the photoelectrons follow Maxwellian distributions, n_i, n_e, and n_p are given by analytical expressions, as presented in Jeong (2008). Based on this assumption, $\phi(h,\theta)$ can be solved numerically from Eq. (2.36).

Given that there is the direct relationship between (h,θ) and the position vector $\boldsymbol{r}$, the electrostatic potential can also be expressed in the Cartesian coordinate as $\phi(\boldsymbol{r})$. Therefore, the electrostatic force acting on a spacecraft with the charge Q is calculated from the equation below.

$$\boldsymbol{F}_E = Q \cdot \boldsymbol{E}(\boldsymbol{r}) = -Q\frac{\partial \phi(\boldsymbol{r})}{\partial \boldsymbol{r}} \tag{2.36}$$

Here, $\boldsymbol{E}(\boldsymbol{r})$ denotes the local electrostatic field. Although the Poisson's equation is decreased to a one-dimensional differential equation as shown in Eq. (2.36), this electrostatic force model can represent three-dimensional variation by numeri-

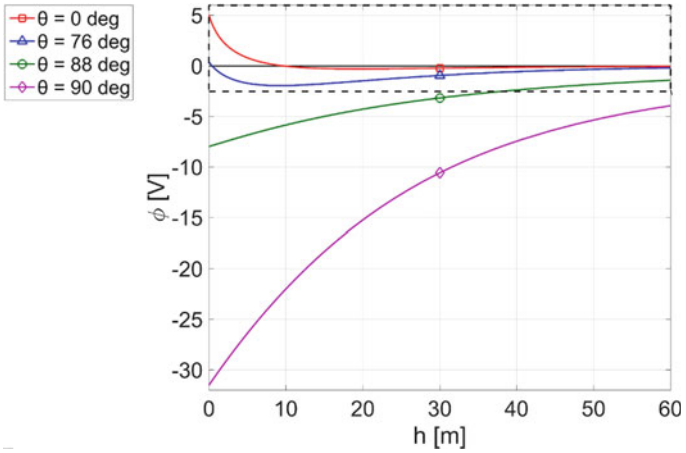

Fig. 2.9 Electrostatic potential profiles for different solar incident angles

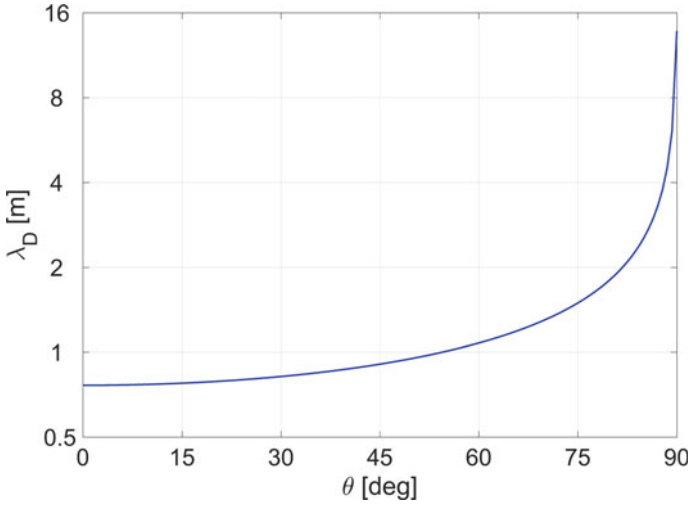

Fig. 2.10 Relationship between the solar incident angle and the Debye length

cally approximating the electrostatic field in longitudinal and latitudinal directions (Hartzell 2012).

Figure 2.9 depicts the electrostatic potential profiles computed from Eq. (2.35) for several different solar incident angles. It can be observed that the surface of the asteroid is positively charged when the solar incident angle is small (i.e., near the subsolar region), while the surface is negatively charged when the solar incident angle is large (i.e., near the terminator region). The enlarged view in Fig. 2.9 also shows that non-monotonic sheath profiles appear in some cases, which implies that the plasma structure around an asteroid is complex. Figure 2.10 shows the relationship between

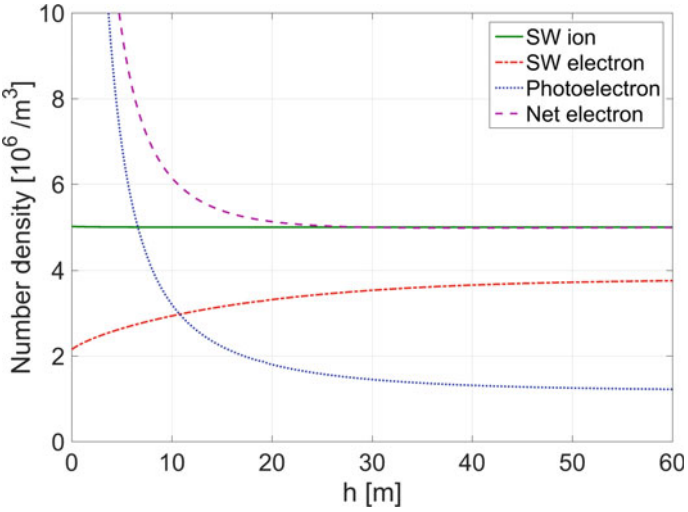

Fig. 2.11 Number densities of charged particles

the solar incident angle and the Debye length λ_D, which is defined in Nitter et al. (1998). The Debye length is an indication of how far from the asteroid surface the electrostatic effects can exert influence. Thus, Fig. 2.10 implies that the electrostatic force obtained in the terminator region is stronger than that of the subsolar region.

Figure 2.11 illustrates the distributions of the charged particles along the subsolar line ($\theta = 0$ deg). One of the remarkable features is that the number density of photoelectrons is considerably large near the surface. This dense photoelectron layer on the dayside involves a strong screening effect. Consequently, the Debye length near the subsolar point is comparatively short, as shown in Fig. 2.10. It is also shown in Fig. 2.11 that when the altitude increases, the density of the net electrons approaches that of solar wind ions, which indicates that the plasma is in a quasi-neutral state.

Figure 2.12 illustrates a contour map of the electrostatic potential around the asteroid, which is expressed in the x–y plane (please note that the symbol [S] is used in the figures of this chapter to mark the direction of the Sun). The broken line in the enlarged view corresponds to the potential level of zero volts, and it is evident that the dayside region close to the surface has positive potential; on the other hand, there exists a strong negative potential region on the nightside and around the terminator. Note that the wake streams of the solar wind behind the asteroid are not considered in this simulation, which can exert a strong influence on the nightside electrostatic potential (Han et al. 2016a; Yu et al. 2016); however, the current model is regarded to be valid for the analysis of plasma structures on the dayside and in the terminator region, which is our major interest as mentioned in the introduction. The visual representation of the electrostatic field is displayed in Fig. 2.13. The direction and magnitude of the electrostatic field are expressed by the arrows and their colors,

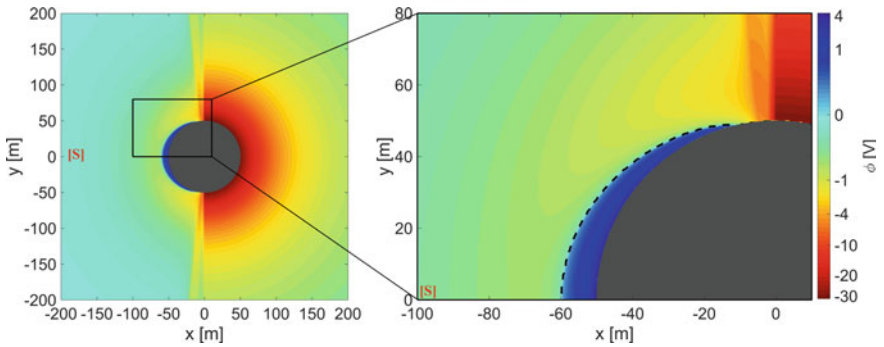

Fig. 2.12 Electrostatic potential around the asteroid

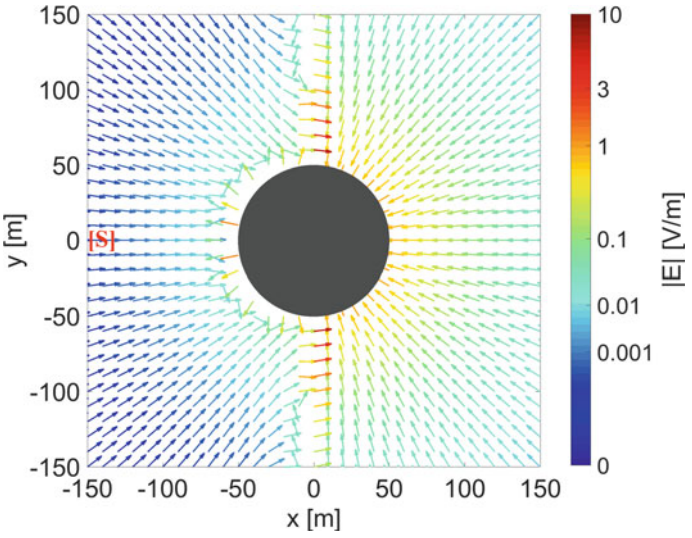

Fig. 2.13 Electrostatic field vector components around the asteroid

respectively. This figure is useful to understand the behavior of electrostatic force acting on an E-Glider and to make effective use of it.

These unique characteristics regarding the plasma environment around an asteroid, which are provided in Figs. 2.9, 2.10, 2.11, 2.12 and 2.13, have been revealed in previous studies as well and are consistent with them (Nitter et al. 1998; Poppe 2011; Han et al. 2016a; Yu et al. 2016). From these observations, it can be concluded that the plasma model used in this study is valid and can be applied for E-Glider simulations.

Besse and Rubin presented in Besse and Rubin (1980) a very clear and simple model of dipole charging, with an insight on the definition of the photoelectron sheath for a sphere. Besse and Rubin (1980) shows the possible issues with a trapping region

for photoelectrons on the sunward side of a charged sphere, and the model used in Besse and Rubin (1980) would be of interest in future studies. For instance, a cross-comparison of the analytical model described in this section coupled with the model presented in Besse and Rubin (1980) with the more accurate but time-consuming numerical simulations using the *USC-IFEPIC* (presented in the next section) will be carried out for E-Glider charging in plasma. Once calibrated, the analytical method can be used to quickly estimate the effects of the photoelectron emission from the E-Glider, making it possible to easily include the effects of spacecraft material properties in the analyses presented in this work. As the spacecraft material selection has not been finalized yet, detailed material properties were not included in E-Glider charging calculations in this paper but will be assessed in future study.

2.8.3 PIC Simulations of the Plasma and Electric Field

As discussed in Section 8.1, the plasma environment around small asteroid is that of a collisionless, mesothermal plasma flow. Furthermore, since the photoelectrons dominate the charging of the sunlit surface and the solar wind electrons dominate the charging of the wake side surface, the detailed dynamics of both the solar wind electrons and the photoelectrons play an important role in asteroid charging. Thus, full kinetic numerical simulations are usually required to correctly model the plasma environment and electric field around a small asteroid.

The collisionless nature of plasma flow around small asteroids renders the particle-in-cell (PIC) method (Birdsall and Langdon 1991), which solves plasma particle trajectory, space charge, and the Poisson equation self-consistently, as the preferred modeling method. To resolve the electron dynamics and the photoelectron sheath correctly, we apply a full particle PIC simulation model, which uses macro-particles to represent both electrons and ions. To maintain the correct mesothermal velocity ratio, full particle simulations must also be carried out using the correct ion to electron mass ratio.

In this study, the simulation model used to resolve the plasma environment and electric field is a recently developed immersed-finite-element particle-in-cell code, *USC-IFEPIC*, Han et al. (2016a, b). The USC-IFEPIC code is a three-dimensional (3D) full particle electrostatic PIC code designed to simulate plasma interactions involving complex boundary conditions. All plasma species (solar wind protons and electrons, photoelectrons, and secondary electrons) are represented by macro-particles. The electric potential Φ, the space charge, and the trajectories of each macro-particle are solved self-consistently from Poisson's equation and Newton's second law:

$$\nabla \cdot (\epsilon \nabla \Phi) = -e(n_i - n_e - n_{ph} - n_{se}), \quad m\frac{d\mathbf{v}}{dt} = q(\mathbf{E} + \mathbf{v} \times \mathbf{B}) \tag{2.37}$$

where ϵ is the relative permittivity, n_i, n_e, n_{ph}, and n_{se} are the number densities of the solar wind ion, solar wind electron, photoelectron, and secondary electron, respectively. In this study, the contribution of secondary electrons emitted from the asteroid surface is ignored because the secondary density is orders of magnitude smaller than that of the other species (Han 2015; Lee 1996; Whipple 1981). Application of the E-Glider is for small asteroids. As the size of most small asteroids is smaller than the ion gyro-radius, the effect of the interplanetary magnetic field is also ignored.

In plasma charging studies, the object surface is typically treated as the boundary to the ambient plasma, and surface charging is handled through a boundary condition coupled with a current balance calculation. Such an approach, which is used in standard spacecraft charging software, is not always sufficient for asteroid charging because asteroids are dielectric objects. The asteroid capacitance is often not trivial, and the combined effects from plasma flow and localized sunlit/shadow regions also generate complex differential charging on the surface. In the USC-IFEPIC code, the asteroid is considered as part of the simulation domain with material conductivity explicitly included. The relative permittivity of the asteroid surface is taken to be similar to that of the lunar regolith, $\epsilon \sim 4$. The electric field is solved for both inside and outside of the asteroid; and asteroid charging is calculated directly from local charge deposition at the surface (Han et al. 2016b).

Full particle PIC simulations using the real ion-to-electron mass ratio are computationally expensive. A critical aspect in this modeling study is to resolve the electric field accurately for complex asteroid shapes while still maintaining an efficient computing speed. *USC-IFEPIC* applies a novel field solution algorithm, the non-homogeneous interface flux jump immersed-finite-element PIC (IFE-PIC) algorithm (Han et al. 2016a, b), to solve the electric field. In this algorithm, the boundary is treated as an interface between two mediums. The solution mesh can be generated regardless of the location of the interface. Poisson's equation is solved using a finite element (FE) method with a bases function designed to resolve the discontinuity of the electric field flux at the interface (Han et al. 2016b). This approach allows one to use a Cartesian-based mesh to solve the electric field in the presence of complex boundaries with the same accuracy as a body-fitting mesh FE solver (Kafafy et al. 2005; Kafafy and Wang 2006). This approach also preserves the standard particle-search and particle-mesh interpolation in PIC, thus maintaining the standard PIC computation speed (Wang et al. 2006).

The USC-IFEPIC model was validated against the one-dimensional (1D) analytical solutions of Nitter et al. (1998), Jeong (2008) in Ref. Han (2015) and was previously applied to simulate lunar surface charging (Han et al. 2018), asteroid charging (Han and Wang 2019), and charged dust dynamics around small asteroids (Yu et al. 2019). Figures 2.14 and 2.15 show a typical set of asteroid–plasma interaction simulations using USC-IFEPIC. The asteroid is taken to be a spherical object that has a rock core and an outer layer of dust grains. The radius of the rock core is about 12.62 m, the outer dust layer thickness is $d_{layer} \simeq 1.38$ m, and the total asteroid radius is $r_A = 14$ m. The asteroid size is similar to that of the near-Earth asteroids 1998 KY26, 2004 FH, 367943 Duende, and 2014 RC.

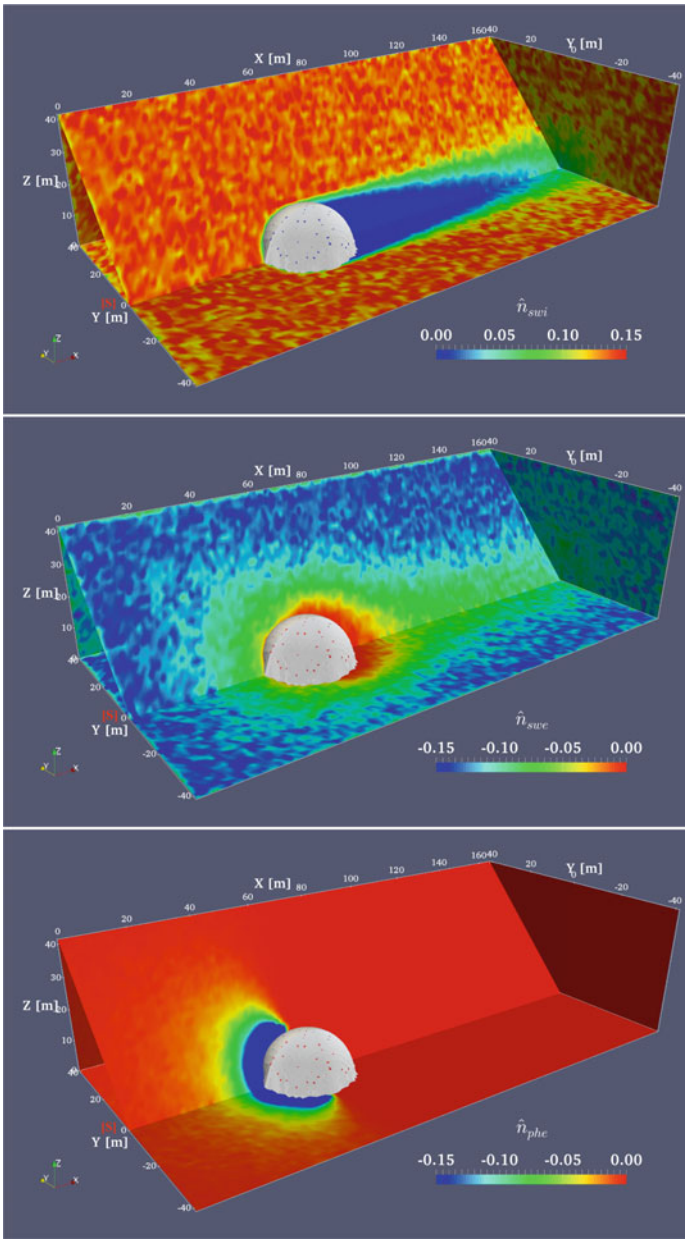

Fig. 2.14 USC-IFEPIC simulations of solar wind–asteroid interactions. From top to bottom: solar wind ions, solar wind electrons, and photoelectrons

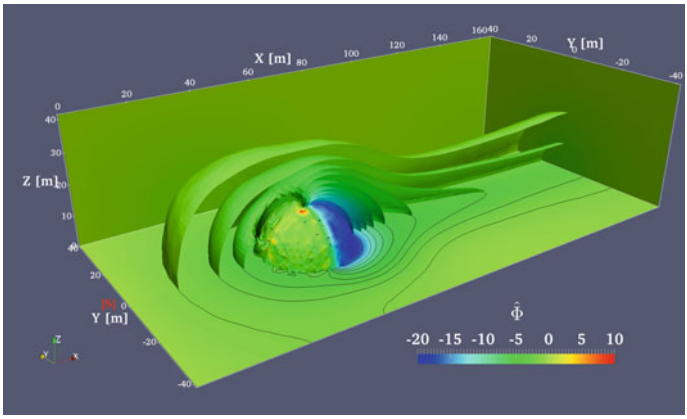

Fig. 2.15 USC-IFEPIC simulations of solar wind–asteroid interactions: electrostatic potential

The species density distribution (Fig. 2.14) shows very clearly the presence of a marked and well-defined plasma wake. The general rarefaction in proximity of the asteroid surface can be attributed to the overall negative net charge acquired by the body. The photoelectrons show a typical diffusion pattern from the sunlit side, and their density rapidly decays to zero with increasing heights. While the species densities of course determine the whole plasma environment and electrostatic fields, *per se* they only come into play in the E-Glider model when calculating current collection and power expenditure. The electrostatic potential, on the other hand, directly influences the spacecraft dynamics, and it is therefore perhaps the most important result of the simulations.

As shown in Fig. 2.15, the near-surface field resembles that of a dipole, which is consistent with the differential charging phenomenon, while the far field decays radially (except in the wake region). The surface potential is in the range of −20 V on the dark side and slightly negative on the sunlit side. This relatively low and negative potential on the sunlit side indicates that, at least for this size of the asteroid, the increased solar wind electron flux is sufficient to offset the positive charge generation caused by the photoelectrons. The potential profile obtained from the simulation also shows that the Nitter model implemented in the past (Nitter et al. 1998; Hartzell 2012) does not provide accurate estimates, especially for small asteroids, being derived from an infinite planar surface 1D model. The main drawbacks of this model are the inability to correctly capture the wake and its underestimation of the radial decay (Fig. 2.16). Both inaccuracies lead to an excessively optimistic and nonconservative estimate of the electric fields.

The electrostatic field intensity, of which the PIC-derived data is shown in Fig. 2.17, offers virtually the same data as the potential, but in a more easily readable form. The electrostatic force on the E-Glider is then calculated by interpolating the electric field obtained from USC-IFEPIC.

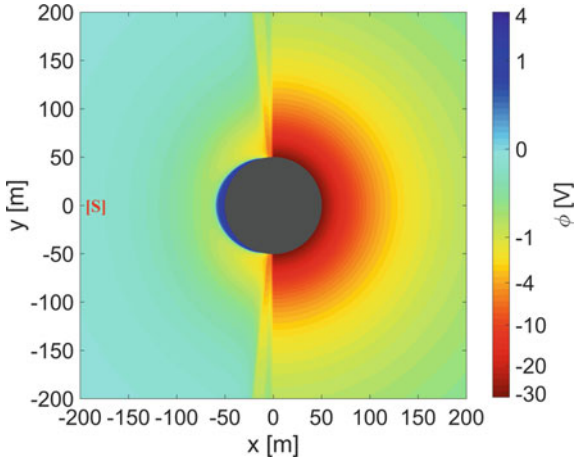

Fig. 2.16 Obsolete electrostatic potential calculated with the Nitter model

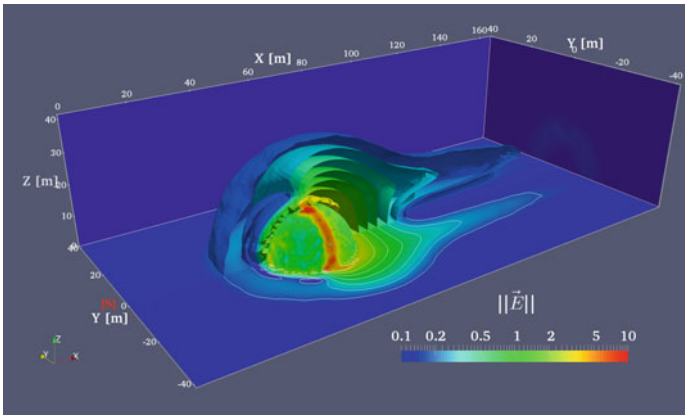

Fig. 2.17 Electrostatic field magnitude

2.9 Electrostatic Forces and Moments

The electrostatic acceleration can be expressed as

$$\boldsymbol{a}_E = \frac{\boldsymbol{F}_E}{M} = \frac{Q}{M}\frac{\partial \phi(\boldsymbol{r})}{\partial \boldsymbol{r}} \tag{2.38}$$

where $\boldsymbol{F}_E$ is the electrostatic force, Q is the charge of an E-Glider, and ϕ is the electrostatic potential. Finally, the SRP acceleration is obtained from the following equation:

$$\boldsymbol{a}_{SRP} = a_{SRP} \cdot \widehat{\boldsymbol{d}} = \frac{(1+\zeta) P_0 A}{d^2 M} \widehat{\boldsymbol{d}} \tag{2.39}$$

where $P_0 \simeq 1 \times 10^{17}$ kg.m/s^2 is the solar flux constant; d is the distance from the Sun expressed in AU; and $\zeta \equiv C_s + 2/3 C_d$ is the reflectivity of the surface of a spacecraft. This model, which is the so-called cannonball model, assumes that a spacecraft has a spherical shape and that the SRP force consists of only a radial component. It should be also noted that the effect of the solar eclipse is not included in this SRP model.

The electrostatic torque applied to a spacecraft is defined by the equation below.

$$\mathbf{T}_E = \int \boldsymbol{\rho} \times d\mathbf{F}_E(\mathbf{R}) \tag{2.40}$$

Here, $\mathbf{R}$ denotes the relative position vector of a mass element with respect to the center of mass of the small body. $\mathbf{R}$ can be expressed as follows:

$$\mathbf{R} = \mathbf{r} + \boldsymbol{\rho} \tag{2.41}$$

where $\mathbf{r}$ is the relative position vector of the center of mass of the spacecraft relative to that of the small body, and $\boldsymbol{\rho}$ is the relative position vector of the element relative to the center of mass of the spacecraft. Considering the vector form of the Taylor series, the following equation can be derived when $\boldsymbol{\rho} \ll \mathbf{r}$:

$$f(\mathbf{R}) = f(\mathbf{r} + \boldsymbol{\rho}) \simeq f(\mathbf{r}) + \nabla f(\mathbf{r}) \cdot \boldsymbol{\rho} \tag{2.42}$$

where $\nabla = \partial / \partial \mathbf{r}$ (see Fig. 2.18).

The electrostatic potential ϕ_E is expressed as a function of the radial distance r and the solar incident angle α. Therefore, the partial derivative of the electrostatic potential is given by the equation below.

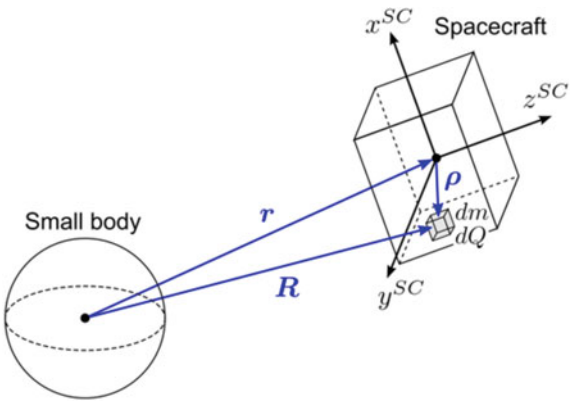

Fig. 2.18 Mass element of the spacecraft modeled as a rigid body

$$\frac{\partial \phi_E}{\partial \mathbf{r}} = \frac{\partial \phi_E}{\partial r}\mathbf{e}_r + \frac{1}{r}\frac{\partial \phi_E}{\partial \alpha}\mathbf{e}_\alpha \tag{2.43}$$

where $\mathbf{e}_r$ is a unit vector along the radial direction, and $\mathbf{e}_\alpha$ is a unit vector along a transverse direction that exists in the same plane as the subsolar line and $\mathbf{e}_r$. According to the definitions, $\mathbf{e}_r$ and $\mathbf{e}_\alpha$ are expressed as follows:

$$\begin{aligned} \mathbf{e}_r &= -\frac{\mathbf{r}}{r} \\ \mathbf{e}_\alpha &= -\frac{\cos\alpha}{r\sin\alpha}\mathbf{r} - \frac{1}{\sin\alpha}\hat{\mathbf{d}} \end{aligned} \tag{2.44}$$

Note that $\hat{\mathbf{d}}$ is a unit vector pointing from the Sun to a small body, which satisfies $\mathbf{r}\cdot\hat{\mathbf{d}} = r\cos\alpha$. Then substitution of Eq. (2.44) into Eq. (2.43) yields the following equation:

$$\begin{aligned} \frac{\partial \phi_E}{\partial \mathbf{r}} &= \left(\frac{1}{r}\frac{\partial \phi_E}{\partial r} + \frac{\cos\alpha}{r^2\sin\alpha}\frac{\partial \phi_E}{\partial \alpha}\right)\mathbf{r} - \frac{1}{r\sin\alpha}\frac{\partial \phi_E}{\partial \alpha}\hat{\mathbf{d}} \\ &\equiv f_1\mathbf{r} + f_2\hat{\mathbf{d}} \end{aligned} \tag{2.45}$$

where f_1 and f_2 are functions of r and α, which are calculated numerically based on the electrostatic potential model. In the same manner, the derivatives of f_1 and f_2 can be expressed as

$$\frac{\partial f_1}{\partial \mathbf{r}} \equiv -g_1\mathbf{r} - g_2\hat{\mathbf{d}}, \quad \frac{\partial f_2}{\partial \mathbf{r}} \equiv -g_2\mathbf{r} - g_3\hat{\mathbf{d}} \tag{2.46}$$

where g_1, g_2, and g_3 are also computed numerically. Consequently, the electrostatic torque can be obtained from Eqs. (2.40)–(2.46) as follows.

$$\begin{aligned} \mathbf{T}_E &= -\int \boldsymbol{\rho} \times \nabla\phi_E(\mathbf{R})\, dQ \\ &= -\int \boldsymbol{\rho} \times (f_1(\mathbf{R})\mathbf{R} + f_2(\mathbf{R})\hat{\mathbf{d}})\, dQ \\ &\simeq -\int \boldsymbol{\rho} \times \{(f_1(\mathbf{r}) + \nabla f_1(\mathbf{r})\cdot\rho)(\mathbf{r}+\boldsymbol{\rho}) + (f_2(\mathbf{r}) + \nabla f_2(\mathbf{r})\cdot\rho)\hat{\mathbf{d}}\}\, dQ \\ &= -\int \boldsymbol{\rho} \times \{(f_1 + g_1\mathbf{r}\cdot\rho - g_2\hat{\mathbf{d}}\cdot\boldsymbol{\rho})(\mathbf{r}+\boldsymbol{\rho}) + (f_2 + g_2\mathbf{r}\cdot\rho - g_3\hat{\mathbf{d}}\cdot\boldsymbol{\rho})\hat{\mathbf{d}}\}\, dQ \\ &\simeq g_1\mathbf{r}\times\mathbf{J}\mathbf{r} + g_2(\mathbf{r}\times\mathbf{J}\hat{\mathbf{d}} + \hat{\mathbf{d}}\times\mathbf{J}\mathbf{r}) + g_3\hat{\mathbf{d}}\times\mathbf{J}\hat{\mathbf{d}} \end{aligned} \tag{2.47}$$

where $\mathbf{J}$ is the tensor defined by the equation below.

$$\mathbf{J} \equiv \int \left(|\boldsymbol{\rho}|^2\mathbf{E} - \boldsymbol{\rho}\boldsymbol{\rho}^T\right)\, dQ \tag{2.48}$$

When it is assumed that the mass distribution and the charge distribution of a spacecraft are identical, the following relationship holds.

$$\frac{dQ(\boldsymbol{\rho})}{Q} = \frac{dm(\boldsymbol{\rho})}{m} \tag{2.49}$$

Based on this assumption, the electrostatic torque in Eq. (2.47) can be rewritten as follows:

$$\mathbf{T}_E = \frac{Q}{m}\{g_1\mathbf{r}\times\mathbf{I}\mathbf{r} + g_2(\mathbf{r}\times\mathbf{I}\hat{\mathbf{d}} + \hat{\mathbf{d}}\times\mathbf{I}\mathbf{r}) + g_3\hat{\mathbf{d}}\times\mathbf{I}\hat{\mathbf{d}}\} \tag{2.50}$$

where $\mathbf{I}$ is the moment of inertia tensor defined by the equation below.

$$\mathbf{I} \equiv \int \left(|\boldsymbol{\rho}|^2\mathbf{E} - \boldsymbol{\rho}\boldsymbol{\rho}^T\right) dm \tag{2.51}$$

The detailed electrostatic torque model derived in this subsection is used for numerical simulations.

Figure 2.12 shows that the gradient of the electrostatic potential is broadly directed to/from the center of the small body. Based on this observation, it can be approximated that the electrostatic force applied to a spacecraft has only a radial component, yielding the equation below.

$$\frac{\partial\phi_E}{\partial\alpha} \equiv 0 \tag{2.52}$$

Based on this approximation, the following equations hold.

$$g_1 = \Gamma, \quad g_2 = g_3 = 0 \tag{2.53}$$

Here, Γ can be numerically computed from the equation below.

$$\Gamma(r) \equiv \frac{1}{r^3}\frac{\partial\phi_E}{\partial r} - \frac{1}{r^2}\frac{\partial^2\phi_E}{\partial r^2} \tag{2.54}$$

From Eqs. (2.50), (2.52), and (2.53), the electrostatic torque can be approximated by the following simplified form:

$$\mathbf{T}_E \simeq \frac{Q\Gamma}{m}\mathbf{r}\times\mathbf{I}\mathbf{r} \tag{2.55}$$

Comparing Eqs. (2.31) and (2.55), it is evident that the electrostatic torque is expressed in the same form as the gravity gradient torque. This similarity enables analytical analyses for the attitude motion of an E-Glider by extending conventional analysis methods. The simplified electrostatic torque model derived in this subsection is used for analytical studies.

2.9.1 Finite Element Electrostatic Force Modeling

To include the plasma wake effects is one of the biggest issues in modeling the electrostatic field, and all the analytical models seem to be inadequate for this purpose. For this reason, the electrostatic field and the electrostatic potential are external input data. These data represent the electrostatic field and potential sampled on a 3D Cartesian mesh of points. The data (both for the electrostatic potential and the electrostatic field) are given in the RIC reference frame, and they are time-invariant (Corradino 2018) by assumption. The time-invariant nature of the data is a strong assumption, but otherwise, the implementation of a dynamic model for the data will result in a high computational load, and it will imply also the need for storage capabilities for a huge amount of data.

The computation of both the force $\mathbf{f}_e$ and the torque $\mathbf{T}_e$ exerted on the spacecraft is possible by starting from the input files containing the values of the electrostatic field of the asteroid under analysis.

We can consider the spacecraft as an extended body characterized by a net charge and first and second moment of charge, or as an ensemble of parts, each one characterized by a net charge localized in the center of charge of the part (which could be not coincident with the center of mass of the part itself). If the assumption of a unique extended body is valid for the spacecraft, the electric field is linear by assumption (as done for the gravity field in a previous section); thus, by defining $\boldsymbol{\rho}$, the electric field can be expressed as

$$\mathbf{E}(\mathbf{r}) = \mathbf{E}(\mathbf{r}_0) + \mathbf{G}_e(\mathbf{r}_0)\boldsymbol{\rho} \tag{2.56}$$

in which $\mathbf{G}_e(\mathbf{r}_0)$ is the electrostatic field gradient computed in the center of mass of the spacecraft. The derivation of an analytical expression is not possible for the electrostatic field gradient; thus, it is numerically computed starting from the data of the electrostatic field. The tensor $\mathbf{G}_e(\mathbf{r}_0)$ is obtained by taking the vector of the gradient of the electrostatic field along the three directions shaped column-wise into a matrix. Hence, the electrostatic force is

$$\begin{aligned}\mathbf{f}_e &= \int_{S/C} \left[\mathbf{E}(\mathbf{r}_0) + \mathbf{G}_e(\mathbf{r}_0)\boldsymbol{\rho}\right] dq = \mathbf{E}(\mathbf{r}_0)\int_{S/C} dq + \mathbf{G}_e(\mathbf{r}_0)\int_{S/C} \boldsymbol{\rho} dq \\ &= \mathbf{E}(\mathbf{r}_0)q + \mathbf{G}_e(\mathbf{r}_0)\mathbf{S}_q\end{aligned} \tag{2.57}$$

The left integral cannot be canceled out because, as specified before, the center of charge may not coincide with the center of mass of the spacecraft. In analogy with the mass-related cases, this term is the first moment of charge $\mathbf{S}_q$ about the center of mass. This term is negligible if the center of mass and the center of charge are coincident. If the spacecraft is an ensemble of i parts, the summation of the force acting on each part is the total force given by the electrostatic field. By naming $\mathbf{r}_i$ the position of the center of mass of each part, the total electrostatic force is

$$\mathbf{f}_e = \sum_i \left(\int_{i-thpart} \mathbf{E}(\mathbf{r}_i) dq_i \right) = \sum_i \left(\mathbf{E}(\mathbf{r}_i) \int_{i-thpart} dq_i \right) = \sum_i \left(\mathbf{E}(\mathbf{r}_i) q_i \right) \tag{2.58}$$

As for the previous case, this method allows us to achieve a higher accuracy (especially in those cases in which the spacecraft is very extended and thus the linear approximation is no more valid) but has as a drawback higher computational cost.

The torque due to the electric field on an extended spacecraft with respect to the center of mass of the spacecraft itself is

$$\mathbf{T}_e = \int_{S/C} \boldsymbol{\rho} \times \mathbf{E}(\mathbf{r}) dq \tag{2.59}$$

By considering the spacecraft as a single extended body, the linear approximation for the local variation of the electric field is valid; thus, Eq. (2.59) can be rewritten as

$$\begin{aligned} \mathbf{T}_e &= \int_{S/C} \boldsymbol{\rho} \times \left[\mathbf{E}(\mathbf{r}_0) + \mathbf{G}_e(\mathbf{r}_0) \boldsymbol{\rho} \right] dq \\ &= \int_{S/C} \boldsymbol{\rho} dq \times \mathbf{E}(\mathbf{r}_0) + \int_{S/C} \boldsymbol{\rho} \times \mathbf{G}_e(\mathbf{r}_0) \boldsymbol{\rho} dq \\ &= \mathbf{S}_q \times \mathbf{E}(\mathbf{r}_0) + \mathbf{T}_{eG} \end{aligned} \tag{2.60}$$

where $\mathbf{T}_{eG}$ involves the computation of the second moment of charge $\mathbf{I}_q$, which is similar to the computation of the mass inertia tensor $\mathbf{J}$, with charges instead of masses. If the spacecraft is made of parts, the transport theorem can be applied to translate all the contributions of each part to a reference point, and then the summation of these contributions gives the second moment of charge of the entire spacecraft. $\mathbf{T}_{eG}$ can be computed as the gravitational torque; thus,

$$\mathbf{T}_{eG} = \begin{bmatrix} G_{e,yz}(I_{q,zz} - I_{q,yy}) + G_{e,xz} I_{q,xy} - G_{e,xy} I_{q,xz} + I_{q,yz}(G_{e,zz} - G_{e,yy}) \\ G_{e,xz}(I_{q,xx} - I_{q,zz}) - G_{e,yz} I_{q,xy} + G_{e,xy} I_{q,yz} + I_{q,xz}(G_{e,xx} - G_{e,zz}) \\ G_{e,xy}(I_{q,yy} - I_{q,xx}) + G_{e,yz} I_{q,xz} - G_{e,xz} I_{q,yz} + I_{q,xy}(G_{e,yy} - G_{e,xx}) \end{bmatrix} \tag{2.61}$$

with $\mathbf{G}_e(\mathbf{r}_0)$ computed in the center of mass. If the spacecraft is an ensemble of parts by assumption, the total torque acting on the spacecraft is the summation of the torques generated by the electrostatic field on each part i. By calling $\mathbf{r}_i$ the position of the center of mass of the *i-th* part, Eq. (2.59) becomes

$$\mathbf{T}_e = \sum_i \left(\boldsymbol{\rho}_i \times \mathbf{E}(\mathbf{r}_i) q_i \right) \tag{2.62}$$

This last formulation offers a more accurate estimation of the torque given by the electrostatic field, but the computational load is higher, as in the previous cases.

2.10 Electrostatic Orbiting and its Stability

Dayside equilibrium points can be created by inducing electrostatic force; however, electrostatic hovering at such an equilibrium point will consume a large amount of power. For this reason, this section proposes the electrostatic orbiting method as an alternative strategy for an E-Glider operation and identifies a new class of periodic orbits around asteroids called *electrostatic periodic orbits*.

2.10.1 Orbit Design Methodology

Electrostatic periodic orbits are designed by using the symmetry inherent in the equations of motion, Eq. (2.9), which can be expressed as follows (Broschart et al. 2009; Hénon 1969):

$$(t, x, y, z) \rightarrow (-t, x, -y, z) \tag{2.63}$$

If the set of variables on the left-hand side of Eq. (2.63) satisfy Eq. (2.9), then that on the right-hand side also satisfies the equation. This symmetry is known to hold for the circular restricted three-body problems subject to SRP, and it holds for an E-Glider system as well because the electrostatic potential is assumed to have symmetry about the x axis. Because of the symmetry, if an initial position on the x–z plane is given as $\boldsymbol{r} = [x_0, 0, z_0]^{\mathrm{T}}$ and an initial velocity perpendicular to this plane is given as $\dot{\boldsymbol{r}} = [0, \dot{y}_0, 0]^{\mathrm{T}}$, then the spacecraft trajectories obtained through forward and backward propagation are symmetrical to each other about the x–z plane (Fig. 2.19a). Thus, when a spacecraft perpendicularly intersects the x–z plane again, a periodic orbit solution is obtained as a closed continuous trajectory (Fig. 2.19b).

Then a set of initial conditions, with three degrees of freedom, are expressed as $(x_0, z_0, \dot{y}_0)$. On the other hand, terminal constraints, $\dot{x} = \dot{z} = 0$, must be satisfied when a trajectory intersects the x–z plane after half a period. Consequently, an electrostatic periodic orbit solution, which is obtained by numerical computation, has one degree of freedom. To systematically analyze the solution space, an initial altitude h_0 and an initial phase ψ_0, which are alternative parameters for describing the initial position in place of x_0 and z_0, are introduced as follows:

$$\begin{aligned} h_0 &= \sqrt{x_0^2 + z_0^2} - R \\ \psi_0 &= \tan^{-1}\left(-\frac{z_0}{x_0}\right) \end{aligned} \tag{2.64}$$

Note that $\psi_0 = 0$ and 90° correspond to the subsolar point and the terminator point, respectively. Among the three initial variables $(h_0, \psi_0, \dot{y}_0)$, an initial altitude h_0 is designated as a free parameter to search for periodic orbit solutions.

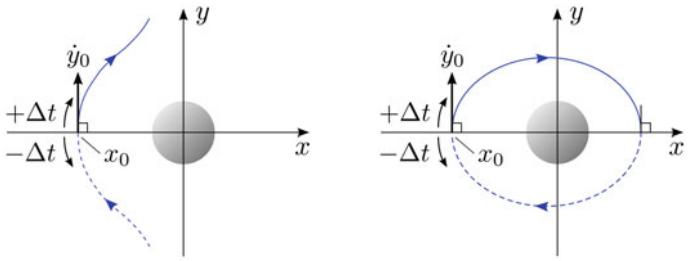

a) General trajectory b) Periodic orbit

Fig. 2.19 Orbit design methodology of electrostatic periodic orbits

2.10.2 Electrostatic Periodic Orbit

Figure 2.20 provides an example of a natural periodic orbit (i.e., $Q = 0$), which is commonly referred to as a terminator orbit, and Fig. 2.21 provides examples of electrostatic periodic orbits for two different charge levels. These orbits are obtained with $h_0 = 15$ m. Note that these figures are expressed in the Hill coordinate, and thus, the negative direction of the x axis corresponds to the direction of the Sun. According to the definition of the coordinate system, these orbits can also be classified as Sun-synchronous orbits that do not experience an eclipse. Here, the periods of the orbits shown in Figs. 2.20, 2.21a, and b are $T = 3.5$, 4.9, and 7.3 hr, respectively.

Figure 2.20 shows that the orbital plane is displaced from the terminator plane in the anti-Sun direction due to the effect of SRP. This observation indicates that this natural periodic orbit is located on the nightside of the asteroid; thus, it is not suitable for optical observations. This is the primary drawback of terminator orbits around asteroids. By contrast, as shown in Fig. 2.21, electrostatic periodic orbits are located on the dayside. Therefore, these orbits offer a significant advantage for optical observations. Moreover, these orbits are Sun-synchronous and achieve constant illumination from the Sun, which is advantageous for solar power generation and thermal design. Broadly speaking, when the magnitude of a charge increases, an orbit achieves larger displacement from the terminator plane in the direction of the Sun, as depicted in Fig. 2.21a and b. Another important fact is that these orbits are accomplished by inducing negative charging, thereby requiring only a small amount of power, as will be pointed out in Sect. 2.15.3.

Figure 2.22 illustrates the history of the magnitudes of forces acting on a spacecraft during one orbital period in the orbit provided in Fig. 2.21a. The magnitude of the electrostatic force was computed as 1–10 μ N in this simulation. While the electrostatic force is weaker than the gravitational force, it has the same order of magnitude as that of the SRP force. This result indicates that an electrostatic periodic orbit with displacement in the direction of the Sun can be achieved without fully compensating for the gravitational force, leading to energy-efficient operation compared with electrostatic hovering.

2.10.3 Evolution of Periodic Orbit Solutions

Shape transitions of electrostatic periodic orbits are depicted in Fig. 2.23. These orbits are computed for different charge values, $-200\,\mu\text{C} \leq Q \leq -3\,\mu\text{C}$, and a constant initial altitude, $h_0 = 15\,\text{m}$, by applying the numerical continuation method (Seydel 2009). The vertical axis represents an initial phase ψ_0 obtained as a result of the numerical calculation. This figure shows intriguing structures of both the entire solution space and orbital shapes themselves. The orbit that is expressed as the diamond marker at $Q = 0$ corresponds to the natural periodic orbit, which is also shown in Fig. 2.20, and it has an initial phase larger than 90°. By contrast, all of the electrostatic periodic orbit solutions depicted in this figure are obtained with initial phases smaller than 90°. It can be inferred from this result that these electrostatic periodic orbits are placed on the dayside, unlike natural terminator orbits. Interestingly, bifurcation appears in the region with a comparatively small magnitude of charge, and it involves several different orbit solutions with exactly the same charge value. As already mentioned, an orbit with a larger magnitude of a charge appears to have larger displacement from the terminator plane.

Figure 2.24 illustrates electrostatic periodic orbits computed for different initial altitudes, $10\,\text{m} \leq h_0 \leq 80\,\text{m}$, and a constant charge, $Q = -50\,\mu\text{C}$. The vertical axis represents an initial velocity $\dot{y}_0$ obtained as a result of the numerical calculation. As observed from the figure, a higher initial altitude does not necessarily result in

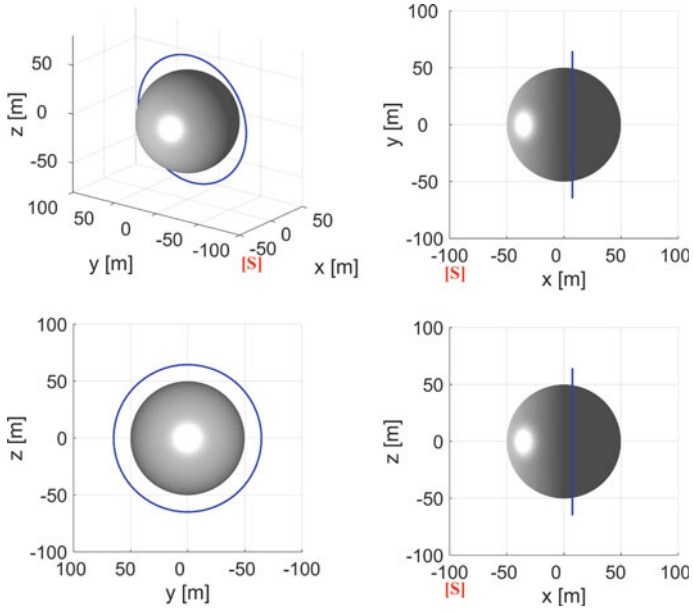

Fig. 2.20 Natural periodic orbit

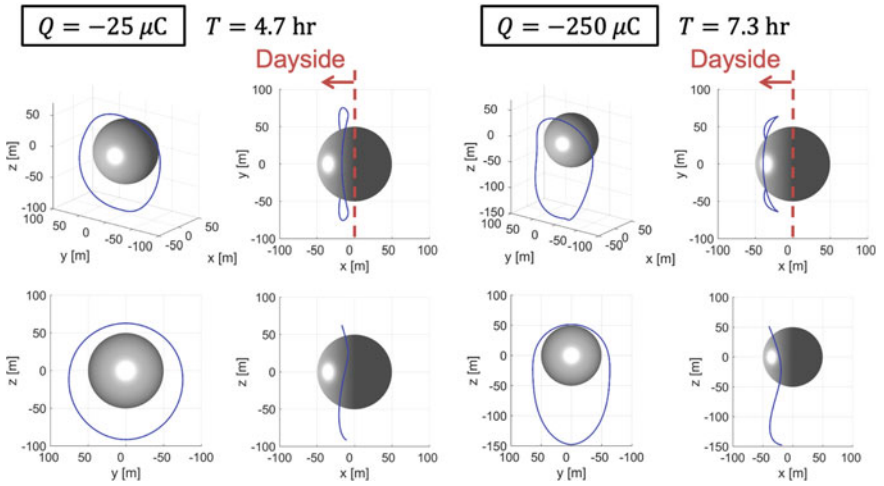

a) $Q = -10\,\mu$C b) $Q = -250\,\mu$C

Fig. 2.21 Electrostatic periodic orbits

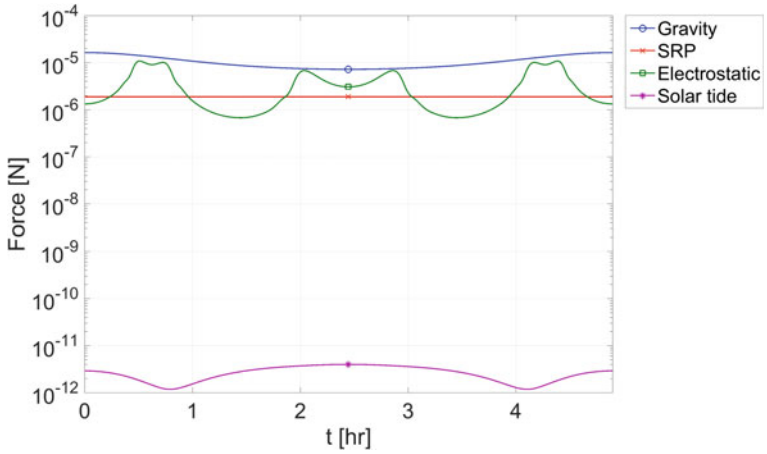

Fig. 2.22 Forces acting on the spacecraft during one orbital period

a larger periodic orbit. Moreover, the orbits on the left side and the right side are almost symmetric to each other about the x–z plane. This result implies that the size of an electrostatic periodic orbit is limited by the charge level because electrostatic force cannot exert influence on the motion of a spacecraft at a high altitude.

It is to be noted that Figs. 2.23 and 2.24 merely show examples of electrostatic periodic orbit families but not the entire orbit solutions. There probably exist other orbit families that are not presented in this study, because multiple equilibrium points are present in this system.

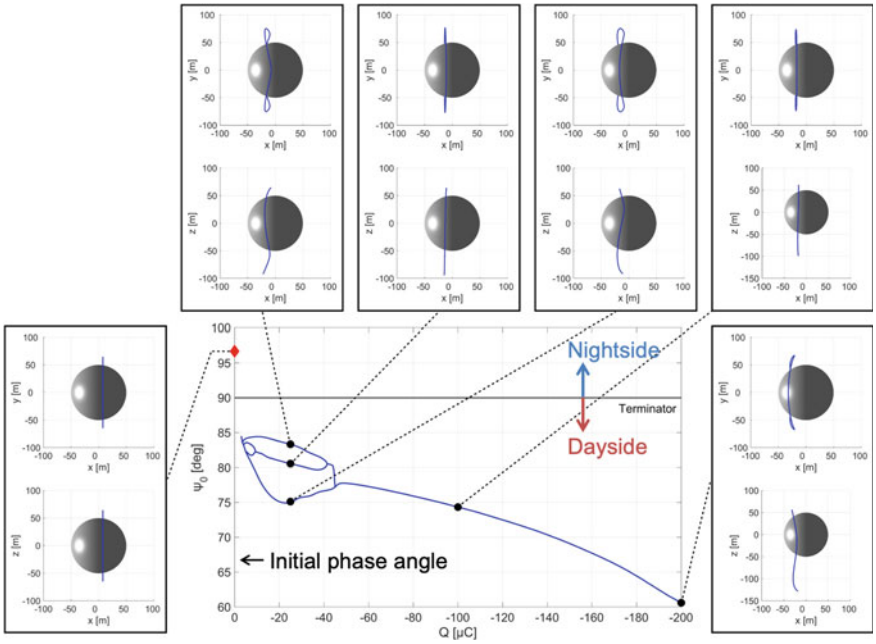

Fig. 2.23 Electrostatic periodic orbit solutions for different charge levels

2.10.4 Effects of Shape Irregularity

Analysis results that have been presented in previous sections are based on the spherical asteroid model. However, asteroids have irregular shapes in general, and the motion of a spacecraft around such an asteroid can be strongly perturbed due to its irregular gravitational field. Moreover, considering an E-glider system, irregularly shaped asteroids form irregular electrostatic fields around them, posing an additional perturbation on the spacecraft. This section evaluates the effects of these perturbations on spacecraft dynamics.

2.10.4.1 Irregular Electrostatic Field

Electrostatic potential around an asteroid is obtained from Eq. (2.35) as a function of the altitude h and the solar incident angle θ. In the case of a spherical asteroid, there exists an explicit relationship between (h, θ) and the position vector $\boldsymbol{r}$, as presented in Eq. (2.34). On the other hand, in the case of an ellipsoidal asteroid, there is no such explicit expression because the position vector and the normal vector to the surface are not parallel, as shown in Fig. 2.8. Therefore, this subsection derives the implicit relationship (h, θ) and the position vector $\boldsymbol{r}$ to compute the electrostatic potential around an ellipsoid.

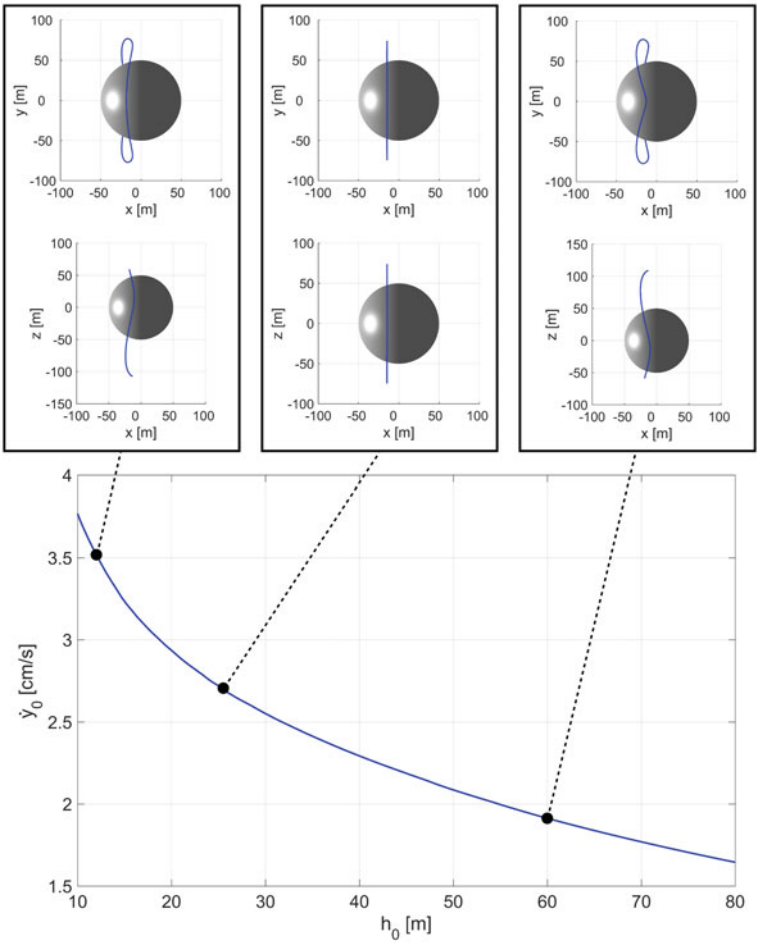

Fig. 2.24 Electrostatic periodic orbit solutions for different initial distances

An arbitrary position on the surface of the ellipsoid is defined as

$$^{B}\boldsymbol{R}_s = [x_s, y_s, z_s]^{\mathrm{T}} \tag{2.65}$$

Then these position variables satisfy the equation below.

$$f(x_s, y_s, z_s) = \frac{x_s^2}{R_a^2} + \frac{y_s^2}{R_b^2} + \frac{z_s^2}{R_c^2} - 1 = 0 \tag{2.66}$$

The normal vector with respect the surface of the ellipsoid at (x_s, y_s, z_s) can be derived as follows:

$$
\begin{aligned}
{}^{B}\boldsymbol{n} &= \left[\frac{\partial f}{\partial x_s}, \frac{\partial f}{\partial y_s}, \frac{\partial f}{\partial z_s}\right]^{\mathrm{T}} = \left[\frac{2x_s}{R_a^2}, \frac{2y_s}{R_b^2}, \frac{2z_s}{R_c^2}\right]^{\mathrm{T}} \\
{}^{B}\widehat{\boldsymbol{n}} &= \frac{{}^{B}\boldsymbol{n}}{|{}^{B}\boldsymbol{n}|}
\end{aligned}
\tag{2.67}
$$

where $\widehat{\boldsymbol{n}}$ represents a unit normal vector. The position vector can be expressed by the following equation:

$$
{}^{B}\boldsymbol{r} = {}^{B}\boldsymbol{R}_s + h \cdot {}^{B}\widehat{\boldsymbol{n}} \tag{2.68}
$$

The coordinate transformation from the asteroid body-fixed coordinate to the Hill coordinate yields the equations below.

$$
{}^{H}\boldsymbol{r} = {}^{H}\boldsymbol{C}_B\,{}^{B}\boldsymbol{r}, \quad {}^{H}\widehat{\boldsymbol{n}} = {}^{H}\boldsymbol{C}_B\,{}^{B}\widehat{\boldsymbol{n}} \tag{2.69}
$$

Finally, the solar incident angle can be calculated as

$$
\theta = \cos^{-1}\left(-{}^{H}\widehat{\boldsymbol{n}} \cdot {}^{H}\widehat{\boldsymbol{d}}\right) \tag{2.70}
$$

where ${}^{H}\widehat{\boldsymbol{d}} = [1, 0, 0]^{\mathrm{T}}$. Based on these equations, h and θ can be calculated implicitly, which can be expressed as follows:

$$
\begin{aligned}
h &= f_1(t, x, y, z) \\
\theta &= f_2(t, x, y, z)
\end{aligned}
\tag{2.71}
$$

Note that these implicit functions are time-dependent because the coordinate transformation ${}^{H}\boldsymbol{C}_B$ is a function of the asteroid rotation phase θ_{rot}. Once h and θ are obtained from Eq. (2.71), the electrostatic potential around an ellipsoidal asteroid can be computed based on Eq. (2.35). The calculation process described above is presented in Fig. 2.25.

Figure 2.26 provides simulation results of the electrostatic potential around an asteroid modeled as a triaxial ellipsoid with an axis ratio of $R_a : R_b : R_c = 2.0 : 1.5 : 1.0$. The electrostatic potentials were calculated for four different rotation angles. These figures demonstrate that a time-varying irregular electrostatic field has been successfully simulated based on the proposed method. It appears that the structure of the electrostatic potential changes dynamically in accordance with the rotation phase of the asteroid. Moreover, this analysis method is performed by mapping an electrostatic potential from a spherical coordinate to an ellipsoidal coordinate based

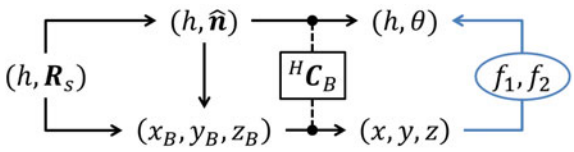

Fig. 2.25 Process of calculating the altitude and the solar incident angle for an ellipsoid

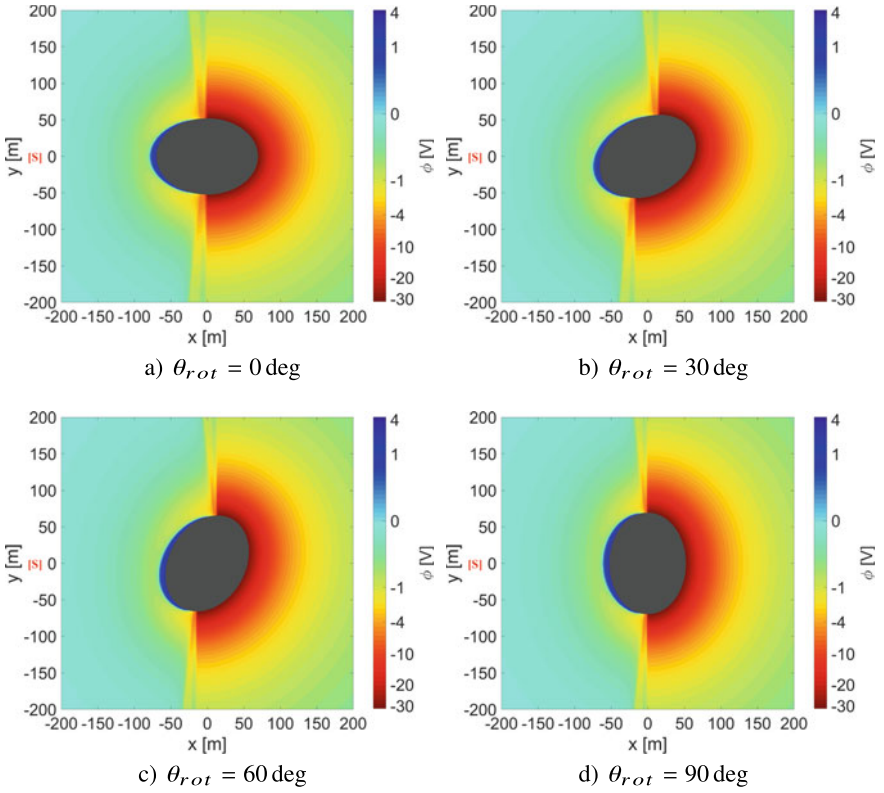

Fig. 2.26 Electrostatic potential around the ellipsoidal asteroid

on the geometrical relationship between them; therefore, it can emulate the time-varying behavior with relatively low computational cost compared with the classical particle-in-cell method.

2.10.4.2 Orbital Motion around an Irregularly Shaped Asteroid

Figure 2.27 provides the simulation results of the orbital motion of an E-glider around an ellipsoidal asteroid. The initial position and velocity used in these simulations are that of the periodic orbit solution around a spherical asteroid which is depicted in Fig. 2.21a. The equation of motion is the same as the one used for a spherical asteroid, but the gravitational potential U_G and the electrostatic potential ϕ are replaced by the models incorporating irregularly shaped effects, as discussed in Sects. 2.6.5 and 2.10.4.1. Note that the directions of asteroids illustrated in Fig. 2.27 merely show the initial states of them, and the asteroids are rotating with respect to the Hill coordinate.

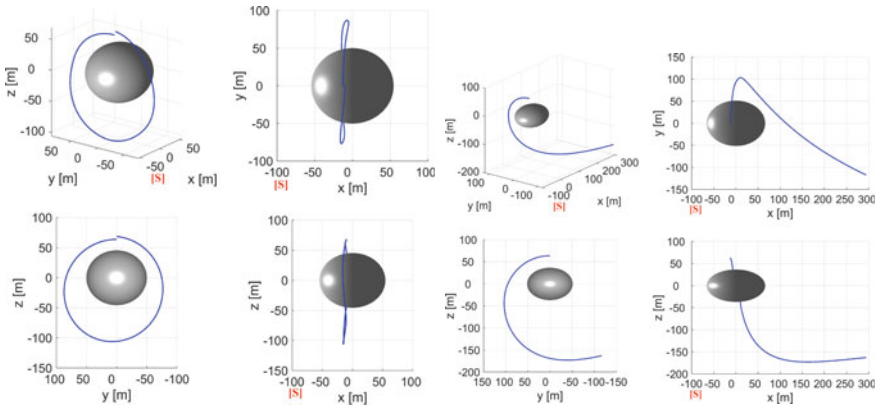

a) $R_a : R_b : R_c = 1.2 : 1.1 : 1.0$ b) $R_a : R_b : R_c = 1.8 : 1.4 : 1.0$

Fig. 2.27 Orbital motion around an irregularly shaped asteroid

Figure 2.27a shows the case for an asteroid with a relatively small oblateness, such as Bennu and Ryugu (1999 JU3) (Nolan et al. 2013; Bellerose and Yano 2010). Although the simulated orbit is perturbed from the reference orbit, the position of the spacecraft after one period is close to the initial position. This result demonstrates that electrostatic orbits obtained for a spherical asteroid can serve as good approximations around a nearly spherical asteroid. On the other hand, the simulation result for an asteroid with a highly irregular shape, such as Itokawa (Fujiwara et al. 2006), is depicted in Fig. 2.27b. It is evident that the spacecraft escapes from the asteroid and is pushed away in the anti-Sun direction by the SRP.

In conclusion, it has been demonstrated that the motion around an irregularly shaped asteroid is perturbed because of the irregular gravitational and electrostatic field effects, and the perturbations might cause escape or collision in the worst-case scenario. This problem can be solved with two different approaches. The first one is to redesign a reference orbit by taking into account the effects of the shape irregularity. The other approach would be the implementation of feedback control of the electrostatic force. The magnitude of forces acting on the spacecraft orbiting around the ellipsoidal asteroid is presented in Fig. 2.28, which corresponds to the simulation provided in Fig. 2.27a. Here, the labels "J2" and "J4" represent the higher-order gravitational forces due to the $J_2 (= -C_{20})$ and $J_4 (= -C_{40})$ terms, respectively. As observed from this figure, the electrostatic force is stronger than the higher-order gravity and the SRP force. This result implies the perturbations can potentially be compensated for by applying the feedback control of electrostatic force via the spacecraft charge.

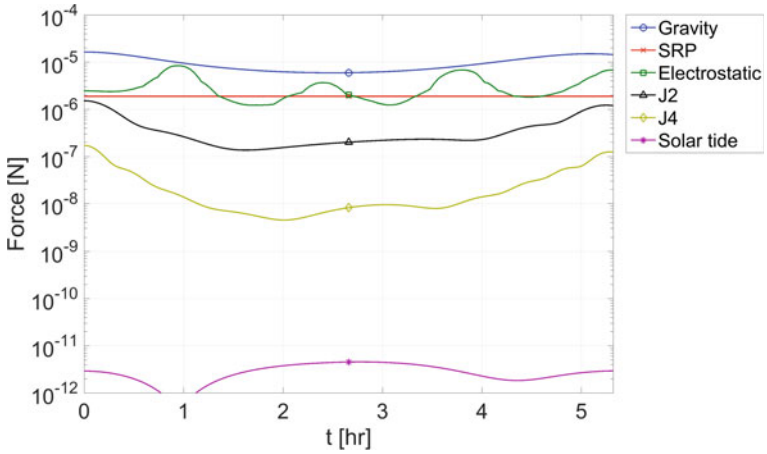

Fig. 2.28 Forces acting on the spacecraft orbiting around an irregularly shaped asteroid

2.11 Attitude Stability

2.11.1 Linearized Euler Equation

The attitude motion of a spacecraft significantly depends on the orbit around a small body. This chapter assumes that a spacecraft is orbiting in a circular electrostatic periodic orbit with a slight displacement in the Sun's direction. Then the orbital coordinate system can be defined as shown in Fig. 2.29.

The origin is at the center of the spacecraft; the z axis points in the direction of the center of the small body; the y axis is perpendicular to both the z axis and the velocity vector of the spacecraft; and the x axis completes a right-handed Cartesian coordinate system. Note that the direction of the x axis is identical to that of the velocity vector of the spacecraft when the orbit is circular. In terms of the orbital coordinate, the attitude of the spacecraft can be expressed by Euler angles (ϕ, θ, ψ), considering a 2–1–3 rotation sequence from the orbital coordinate to the body-fixed

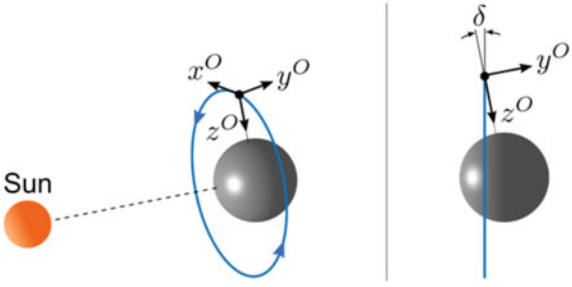

Fig. 2.29 Orbital coordinate system

coordinate. Note that the x, y, and z axes are called the roll, pitch, and yaw axes, respectively.

The angular velocity vector is expressed in the spacecraft-fixed frame as

$$^{SC}\boldsymbol{\omega}_{SC/I} = {}^{SC}\boldsymbol{\omega}_{SC/O} + {}^{SC}\mathbf{C}_O\,{}^{O}\boldsymbol{\omega}_{O/I} \tag{2.72}$$

where ${}^{SC}\mathbf{C}_O$ denotes the rotational transformation from the orbital coordinate to the spacecraft-fixed coordinate given by the equation below.

$$^{SC}\mathbf{C}_O = \mathbf{R}_z(\psi)\mathbf{R}_x(\phi)\mathbf{R}_y(\theta) \tag{2.73}$$

Considering a 2–1–3 rotation sequence, the angular velocity vector of the spacecraft-fixed frame relative to the orbital coordinate can be calculated from the following equation (Hughes 1986):

$$^{SC}\boldsymbol{\omega}_{SC/O} = \begin{bmatrix} \dot{\phi} - \dot{\psi}\sin\theta \\ \dot{\theta}\cos\phi + \dot{\psi}\sin\phi\cos\theta \\ -\dot{\theta}\sin\phi + \dot{\psi}\cos\phi\cos\theta \end{bmatrix} \tag{2.74}$$

Assuming that the orbit offset angle illustrated in Fig. 2.29 is sufficiently small ($\delta \ll 1$) and that the mean motion of a small body is negligible compared with that of a spacecraft orbit ($N \ll n$), the angular velocity vector of the orbital coordinate relative to the inertial coordinate can be calculated from the following equation:

$$^{O}\boldsymbol{\omega}_{O/I} \simeq -n\begin{bmatrix} 0 \\ \cos\delta \\ \sin\delta \end{bmatrix} \simeq -n\begin{bmatrix} 0 \\ 1 \\ \delta \end{bmatrix} \tag{2.75}$$

where n represents the mean motion of an orbit around a small body. Under the approximation that the mean motion of an electrostatic periodic orbit is identical to that of a Keplerian orbit with a radius of r, the following relationship is obtained.

$$n \simeq \sqrt{\frac{\mu}{r^3}} \tag{2.76}$$

The position vector $\mathbf{r}$ and the moment of inertia tensor $\mathbf{I}$ are expressed in the spacecraft-fixed frame as

$$^{SC}\mathbf{r} = {}^{SC}\mathbf{C}_O\,{}^{O}\mathbf{r} = {}^{SC}\mathbf{C}_O\begin{bmatrix} 0 \\ 0 \\ -r \end{bmatrix} \tag{2.77}$$

$$^{SC}\mathbf{I} = \begin{bmatrix} I_x & 0 & 0 \\ 0 & I_y & 0 \\ 0 & 0 & I_z \end{bmatrix} \tag{2.78}$$

Let the Euler angles and their derivatives be given as follows:

$$\phi = \bar{\phi},\ \theta = \psi = \dot{\phi} = \dot{\theta} = \dot{\psi} = 0 \tag{2.79}$$

Here, $\bar{\phi}$ is a roll angle that satisfies $\bar{\phi} \ll 1$. Then by substituting Eqs. (2.72)–(2.79) into the Euler equation, it can be easily observed the equations of pitch motion about the y axis and yaw motion about the z axis are satisfied, which means that these motions are in equilibrium. The remaining equation about the roll axis must satisfy the equation below to achieve the equilibrium attitude.

$$\begin{aligned} &(I_z - I_y)n^2(\bar{\phi} - \delta) + (I_z - I_y)\left(\frac{3\mu}{r^5} + \frac{Q\Gamma}{m}\right)r^2\bar{\phi} = 0 \\ &\Leftrightarrow (I_z - I_y)n^2\{(4+\xi)\bar{\phi} - \delta\} = 0 \end{aligned} \tag{2.80}$$

Here, ξ is a nondimensional scalar value that represents the effect of electrostatic torque and is defined by the equation below.

$$\xi \equiv \frac{Qr^5\Gamma(r)}{m\mu} \tag{2.81}$$

By solving Eq. (2.80), the equilibrium roll angle is obtained from the next equation.

$$\bar{\phi} = \frac{\delta}{4+\xi} \tag{2.82}$$

If the equilibrium attitude given by Eq. (2.79) is stable, an E-Glider system can achieve passive stabilization using gravity gradient torque and electrostatic torque. Given that the attitude of a spacecraft has a small deviation from its equilibrium state, the Euler angles can be expressed as $(\phi + \bar{\phi},\ \theta,\ \psi)$, where $\phi, \theta, \psi \ll 1$. On the basis of this assumption, Eqs. (2.73) and (2.74) are approximated by the equation below:

$${}^{SC}\mathbf{C}_O \simeq \begin{bmatrix} 1 & \psi & -\theta \\ -\psi & 1 & \phi + \bar{\phi} \\ \theta & -(\phi + \bar{\phi}) & 1 \end{bmatrix},\ {}^{SC}\boldsymbol{\omega}_{SC/O} \simeq \begin{bmatrix} \dot{\phi} \\ \dot{\theta} \\ \dot{\psi} \end{bmatrix} \tag{2.83}$$

Consequently, the following linearized Euler equations can be derived:

$$\begin{aligned} &I_x\ddot{\phi} - (I_x - I_y + I_z)n\dot{\psi} + (4+\xi)(I_y - I_z)n^2\phi = 0 \\ &I_y\ddot{\theta}(3+\xi)(I_x - I_z)n^2\theta = 0 \\ &I_z\ddot{\psi} + (I_x - I_y + I_z)n\dot{\psi} - (I_x - I_y)n^2\psi = 0 \end{aligned} \tag{2.84}$$

2.11.2 Stability Conditions

This subsection derives stability conditions of the attitude motion of an E-Glider based on the linearized equations of motion. Let the inertia ratio parameters be defined as

$$\sigma_1 = \frac{I_y - I_z}{I_x},\ \sigma_2 = \frac{I_x - I_z}{I_y},\ \sigma_3 = \frac{I_y - I_x}{I_z} \tag{2.85}$$

By using these parameters, Eq. (2.84) can be rewritten as the equation below.

$$\begin{aligned} &\ddot{\phi} - (1-\sigma_1)n\dot{\psi} + (4+\xi)\sigma_1 n^2\phi = 0 \\ &\ddot{\theta} + (3+\xi)\sigma_2 n^2\theta = 0 \\ &\ddot{\psi} + (1-\sigma_3)n\dot{\phi} + \sigma_3 n^2\psi = 0 \end{aligned} \tag{2.86}$$

These linearized equations show that the roll motion and the yaw motion are coupled with each other, whereas the pitch motion is independent.

When the eigenvalue of this system is expressed as λ, the characteristic equation regarding the pitch motion is given by the equation below.

$$\lambda^2 + (3+\xi)\sigma_2 n^2 = 0 \tag{2.87}$$

In the same manner, the characteristic equation regarding the roll and yaw motions is derived from the first and the third equations of Eq. (2.86), as expressed by the equation below.

$$\lambda^4 + \{1 + (3+\xi)\sigma_1 + \sigma_1\sigma_3\}n^2\lambda^2 + (4+\xi)\sigma_1\sigma_3 n^4 = 0 \tag{2.88}$$

Given the form of the characteristic equations presented in Eqs. (2.87) and (2.88), the pitch motion is stable when the eigenvalues are a conjugate pair of pure imaginary values, and the roll–yaw motion is stable when the eigenvalues have two conjugate pairs of pure imaginary values. Accordingly, the stability condition of the pitch motion is given by the following inequality, considering the relationship between the inertia ratio parameters.

$$(3+\xi)\sigma_2 > 0 \ \Leftrightarrow\ (3+\xi)(\sigma_1 - \sigma_3) > 0 \tag{2.89}$$

The stability conditions of the roll–yaw motion are given by the three inequalities below.

$$\begin{aligned} &(4+\xi)\sigma_1\sigma_3 > 0 \\ &1 + (3+\xi)\sigma_1 + \sigma_1\sigma_3 > 0 \\ &\{1 + (3+\xi)\sigma_1 + \sigma_1\sigma_3\}^2 - 4(4+\xi)\sigma_1\sigma_3 > 0 \end{aligned} \tag{2.90}$$

Table 2.2 Classification of the stability domain based on the ξ value

Category	Condition
Class 1	$0 < \xi$
Class 2	$-3 < \xi < 0$
Class 3	$-4 < \xi < -3$
Class 4	$\xi < -4$

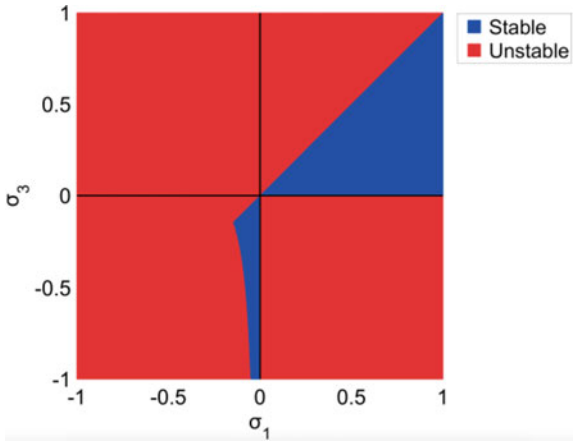

Fig. 2.30 The stability domain of the attitude motion subject to gravity gradient torque

Consequently, when the four inequalities given by Eqs. (2.89) and (2.90) are satisfied, the attitude motion of a spacecraft subject to the gravity gradient torque and the electrostatic torque exhibits stability. It is to be noted that these inequalities are expressed as the conditions on σ_1 and σ_3. Another important fact is that the stability condition is dominated by the nondimensional parameter ξ. According to the definition given by Eq. (2.81), this parameter is an index of the magnitude of the electrostatic torque relative to the gravity gradient torque, and $\xi = 0$ corresponds to the classical attitude problem, in which the attitude motion is influenced solely by the gravity gradient torque (Hughes 1986).

In accordance with the ξ value, the stability behavior of the attitude motion of a spacecraft can be categorized into four types, as indicated in Table 2.2. Figure 2.30 shows the stability domain expressed in the σ_1–σ_3 plane when the electrostatic torque is not considered. The blue region represents the cases where the spacecraft achieves stable libration around an equilibrium state. On the other hand, Fig. 2.31 illustrates the stability domains for the cases where the electrostatic is induced by using an E-Glider system. This figure shows examples of the four different types of stability diagrams, which are categorized based on Table 2.2. Comparing Figs. 2.30, 2.31a, and b, the class 1 system has a smaller stable region than that of the conventional system, while the class 2 system has a larger stable region. Intriguingly, the stability domain changes drastically in the class 3 and class 4 systems, as depicted in Fig. 2.31c

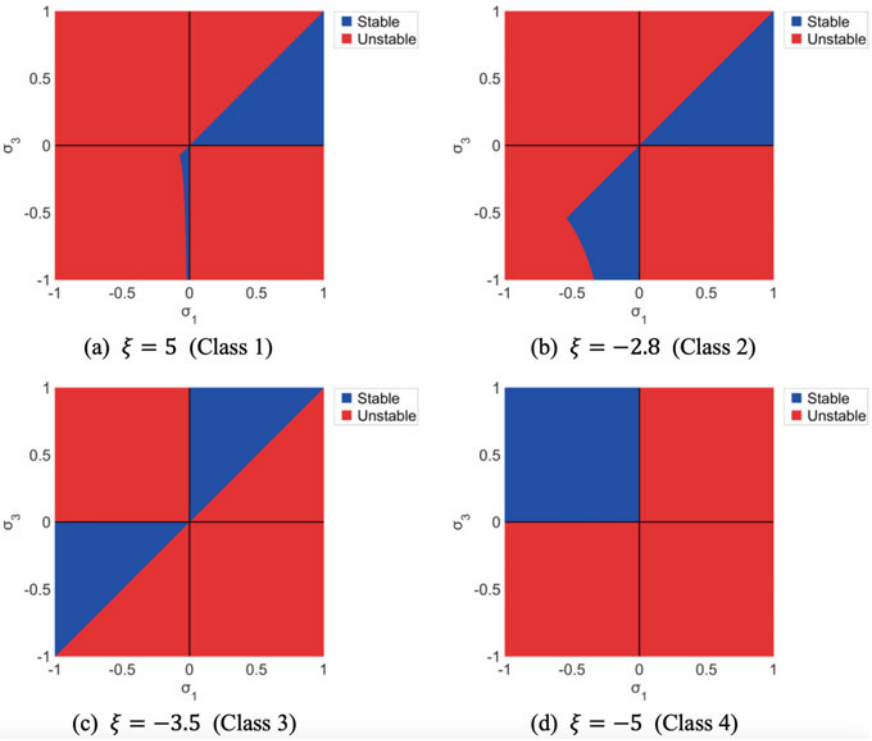

Fig. 2.31 The stability domain of the attitude motion subject to gravity gradient and electrostatic torques

and d. These results imply that the use of electrostatic torque enables a spacecraft to stabilize its attitude even when the spacecraft is originally unstable under the effect of the gravity gradient torque.

Since the attitude stability behavior of an E-Glider significantly depends on the ξ value, it is of great importance to analyze the possible range of ξ. As given by Eq. (2.87), the ξ value is a function of the charge Q and the distance r. Therefore, a contour map of ξ can be created in the $Q - h$ plane, as illustrated in Fig. 2.32. Here, h is the altitude, and the orbit offset angle is specified as $\sigma = 10°$. This figure indicates that ξ varies widely enough to allow all of the possible four stability types. Based on this contour map and Table 2.2, the categorization of the attitude stability can be expressed in the $Q - h$ plane, as shown in Fig. 2.33. Each category is displayed in four different colors. This color map enables easy identification of the attitude stability behavior of a spacecraft orbiting in the corresponding electrostatic periodic orbit. A category transition appears at the altitude of approximately $h = 18$ m, which corresponds to the minimum-potential altitude of a non-monotonic sheath profile.

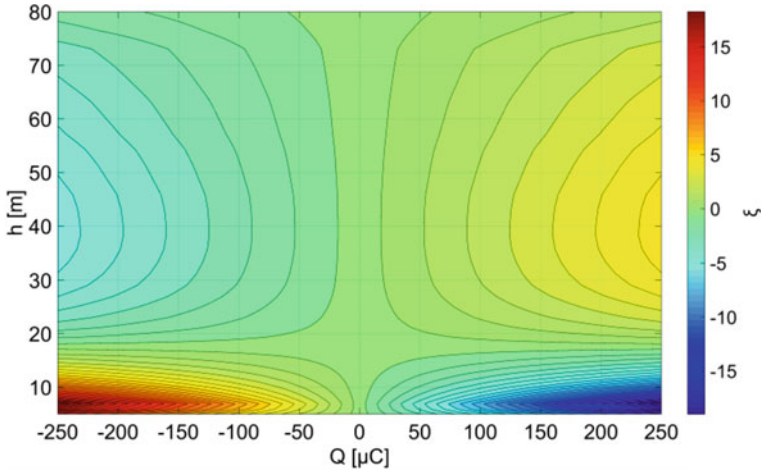

Fig. 2.32 Contour map of the ξ value

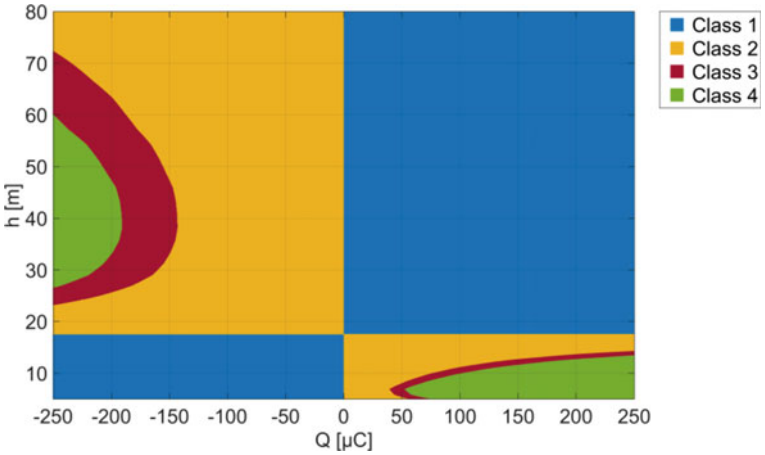

Fig. 2.33 Classification of the attitude stability based on the ξ value

2.11.3 Pitch Motion and Phase Diagram

Consider the situation where the offset of an orbital plane from the terminator plane is sufficiently small, and thus $\delta \simeq 0$ holds. In this case, if the roll and yaw motions are initially in equilibrium, these motions and the pitch motion do not influence each other. The independent pitch motion can be analyzed from the governing equations by substituting $\phi = \psi = \dot{\psi} = \dot{\phi} = 0$. This condition yields the equation below.

$$^{SC}\mathbf{C}_O = \begin{bmatrix} \cos\theta & 0 & -\sin\theta \\ 0 & 1 & 0 \\ \sin\theta & 0 & \cos\theta \end{bmatrix}, \quad ^{SC}\boldsymbol{\omega}_{SC/I} = \begin{bmatrix} 0 \\ \dot{\theta} - n \\ 0 \end{bmatrix} \tag{2.91}$$

Consequently, the equation of pitch motion is derived from Euler's equation as follows:

$$\ddot{\theta} = (3 + \xi)\sigma_2 n^2 \sin\theta \cos\theta = 0 \tag{2.92}$$

By integrating this equation, the following equation is obtained:

$$\dot{\theta}^2 + (3 + \xi)\sigma_2 n^2 \sin^2\theta = C_\theta \tag{2.93}$$

where C_θ is an integration constant. Let τ denote a time unit defined by the equation below.

$$\tau \equiv \frac{1}{n\sqrt{(3 + \xi)\sigma_2}} \tag{2.94}$$

By using this time unit, Eq. (2.93) can be normalized as

$$\left(\frac{d\theta}{d\hat{t}}\right)^2 + \sin^2\theta = \hat{C}_\theta \tag{2.95}$$

where

$$\hat{t} = \frac{t}{\tau}, \quad \hat{C}_\theta = C_\theta \times \tau^2 \tag{2.96}$$

Once $\hat{C}_\theta$ is specified by an initial condition, the pitch angle θ and its change rate $d\theta/d\hat{t}$ are governed by Eq. (2.95). In other words, Eq. (2.95) describes the law of the conservation of energy. Note that it is assumed that Eqs. (2.89) and (2.90) are satisfied, and thus the attitude motion is in a stable state.

Figure 2.34 illustrates the phase plane plot for the pitch motion described by Eq. (2.95). This figure is displayed as a contour map of the $\hat{C}_\theta$ value. It is to be noted that the values in this figure are normalized by the time unit. A stable equilibrium appears at $\theta = 0°$, and unstable equilibria appear at $\theta = \pm 90°$. It can also be observed that the pitch motion exhibits two modes of behavior depending on the $\hat{C}_\theta$ value: libration motion when $\hat{C}_\theta < 1$ and tumbling motion when $\hat{C}_\theta > 1$. The boundary between these two modes is a separatrix defined as $\hat{C}_\theta = 1$, which is represented as a bold contour line in the figure. This phase plane does not depend on the system parameters because it is scaled by the time unit τ, which is a function of the ξ value. The proposed analytical method enables comprehending the mode of the pitch motion of an E-Glider subject to electrostatic torque.

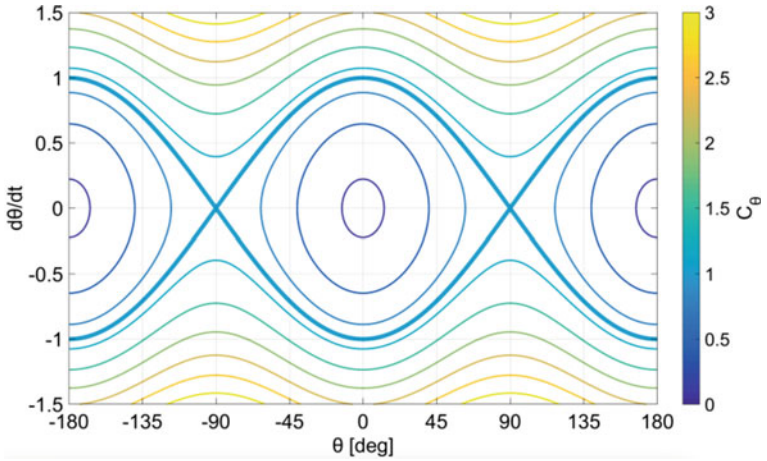

Fig. 2.34 Phase plane for the pitch motion

2.12 Coupled Orbital Attitude Stability

The stability of the attitude motion of a spacecraft subject to electrostatic torque has been analyzed using an analytical approach. Although these analyses enable an understanding of the dynamical structure of the attitude motion, they are performed based on linearization and approximations. This section, therefore, investigates the attitude motion through numerical simulations to verify the validity of the analytical theories established in the previous section.

2.12.1 Coupled Orbit–Attitude Equations of Motion

Let $(\mathbf{e}_{O,x}, \mathbf{e}_{O,y}, \mathbf{e}_{O,z})$ denote a set of unit vectors of the orbital coordinate. From the definition of the orbital coordinate, $\mathbf{e}_{O,x}$, $\mathbf{e}_{O,y}$, and $\mathbf{e}_{O,z}$ are calculated as

$$\mathbf{e}_{O,z} = -\frac{\mathbf{r}}{|\mathbf{r}|},\ \mathbf{e}_{O,y} = \frac{\mathbf{e}_{O,z} \times \mathbf{v}}{|\mathbf{e}_{O,z} \times \mathbf{v}|},\ \mathbf{e}_{O,x} = \mathbf{e}_{O,y} \times \mathbf{e}_{O,z} \tag{2.97}$$

By using these basis vectors, the rotational transformation matrix from the Hill coordinate system to the orbital coordinate system can be expressed as follows (Hughes 1986):

$${}^{O}\mathbf{C}_{H} = \left[{}^{H}\mathbf{e}_{O,x}\ {}^{H}\mathbf{e}_{O,y}\ {}^{H}\mathbf{e}_{O,z}\right]^{T} \tag{2.98}$$

Considering a 2–1–3 rotation sequence from the orbital coordinate to the spacecraft-fixed coordinate, the attitude of a spacecraft is expressed by Euler angles (ϕ, θ, ψ). Then the following kinematic equation is derived.

$$\begin{aligned}\begin{bmatrix}\dot{\phi}\\ \dot{\theta}\\ \dot{\psi}\end{bmatrix} &= \begin{bmatrix}1 & \sin\phi\tan\theta & \cos\phi\tan\theta\\ 0 & \cos\phi & -\sin\phi\\ 0 & \sin\phi\sec\theta & \cos\phi\sec\theta\end{bmatrix}\begin{bmatrix}\tilde{\omega}_x\\ \tilde{\omega}_y\\ \tilde{\omega}_z\end{bmatrix}\\ &= \begin{bmatrix}1 & \sin\phi\tan\theta & \cos\phi\tan\theta\\ 0 & \cos\phi & -\sin\phi\\ 0 & \sin\phi\sec\theta & \cos\phi\sec\theta\end{bmatrix}\begin{bmatrix}\omega_x-\Omega_x\\ \omega_y-\Omega_y\\ \omega_z-\Omega_z\end{bmatrix}\end{aligned} \tag{2.99}$$

where ${}^{SC}\boldsymbol{\omega}_{SC/I} = \left[\omega_x,\ \omega_y,\ \omega_z\right]^T$, ${}^{SC}\boldsymbol{\omega}_{SC/O} = \left[\tilde{\omega}_x,\ \tilde{\omega}_y,\ \tilde{\omega}_z\right]^T$, and ${}^{SC}\boldsymbol{\omega}_{O/I} = \left[\Omega_x,\ \Omega_y,\ \Omega_z\right]^T$. The angular velocity ${}^{SC}\boldsymbol{\omega}_{O/I}$ is given by the equation below.

$${}^{SC}\boldsymbol{\omega}_{O/I} = {}^{SC}\mathbf{C}_O\left({}^{O}\boldsymbol{\omega}_{O/H} + {}^{O}\mathbf{C}_H\,{}^{H}\boldsymbol{\omega}_{H/I}\right) \tag{2.100}$$

Here, ${}^{H}\boldsymbol{\omega}_{H/I} = [0, 0, N]^T$ holds from the definition; ${}^{SC}\mathbf{C}_O$ and ${}^{O}\mathbf{C}_H$ are obtained from Eqs. (2.73) and (2.98), respectively; and ${}^{O}\boldsymbol{\omega}_{O/H}$, which is the angular velocity vector of the orbital coordinate with respect to the Hill coordinate, is obtained from the relationship below.

$$\left[{}^{O}\boldsymbol{\omega}_{O/H}\right]^x = {}^{O}\mathbf{C}_H\left({}^{O}\dot{\mathbf{C}}_H\right)^T \tag{2.101}$$

${}^{O}\dot{\mathbf{C}}_H$ can be computed by numerically integrating the position and velocity of a spacecraft. Here, the notation $[\mathbf{u}]^x$ requires the formation of a skew-symmetric matrix from the elements of $\mathbf{u}$ according to the following equation.

$$[\mathbf{u}]^x \equiv \begin{bmatrix}0 & -u_3 & u_2\\ u_3 & 0 & -u_1\\ -u_2 & u_1 & 0\end{bmatrix} \tag{2.102}$$

The equation of attitude motion given by the Euler equation can be expressed in the spacecraft-fixed frame as follows:

$$\begin{bmatrix}I_x\dot{\omega}_x\\ I_y\dot{\omega}_y\\ I_z\dot{\omega}_z\end{bmatrix} = \begin{bmatrix}(I_y-I_z)\omega_y\omega_z\\ (I_z-I_x)\omega_z\omega_x\\ (I_x-I_y)\omega_x\omega_y\end{bmatrix} + {}^{SC}\mathbf{T}_G + {}^{SC}\mathbf{T}_E \tag{2.103}$$

The gravity gradient torque $\mathbf{T}_G$ is calculated from Eq. (2.31), and the electrostatic torque $\mathbf{T}_E$ is calculated from Eq. (2.50) based on the detailed model. Both $\mathbf{T}_G$ and $\mathbf{T}_E$ are dependent on the position of a spacecraft in addition to its attitude, and thus the attitude motion is coupled with the orbital motion. Consequently, Eqs. (2.9), (2.99), (2.103), and the relationship between position and velocity provide a total of 12 equations; thus, the following 12 variables can be calculated via numerical integration:

$$(x, y, z, \dot{x}, \dot{y}, \dot{z}, \phi, \theta, \psi, \dot{\phi}, \dot{\theta}, \dot{\psi}) \tag{2.104}$$

2.12.2 Stable and Unstable Attitude Motion

The attitude motion of an E-Glider is simulated for four cases that are listed in Table 2.3. Numerical simulations are performed for two different periodic orbits with two different sets of moment of inertia parameters. Figure 2.35 shows the reference electrostatic periodic orbits for the numerical simulations. The orbit illustrated in Fig. 2.35a has a ξ value of –0.18, and thus the attitude stability mode is categorized as class 2, as shown in Fig. 2.36a. On the other hand, the orbit illustrated in Fig. 2.35b has a ξ value of –3.86, exhibiting the class 3 stability mode, as presented in Fig. 2.37a. Figures 2.36b and 2.37b show that one set of moment of inertia parameters is a stable case and that the other set is unstable. Initial conditions are given such that the state variables are in the equilibrium state, but small errors are added in the initial ϕ and θ values.

The simulation results are presented in Fig. 2.38. The history of the Euler angles (ϕ, θ, ψ) is provided in this figure. Figure 2.38a and b correspond to the simulations for the orbit illustrated in Fig. 2.35a, c and d illustrate the results for the orbit shown in Fig. 2.35b. Figure 2.38a indicates that each Euler angle oscillates about an equilibrium state without diverging. Note that the broken line in the figure represents the

Table 2.3 Simulation conditions for stable and unstable attitude motions

	Charge	Altitude	ξ	Category	I_x, I_y, I_z	Stability
Case A	–30 μC	20 m	–0.18	Class 2	4, 5, 2 $\times 10^{-3} Kg/m^2$	Stable
Case B	–30 μC	20 m	–0.18	Class 2	2, 5, 4 $\times 10^{-3} Kg/m^2$	Unstable
Case C	–280 μC	58 m	–3.86	Class 3	2, 5, 4 $\times 10^{-3} Kg/m^2$	Stable
Case D	–280 μC	58 m	–3.86	Class 3	4, 5, 2 $\times 10^{-3} Kg/m^2$	Unstable

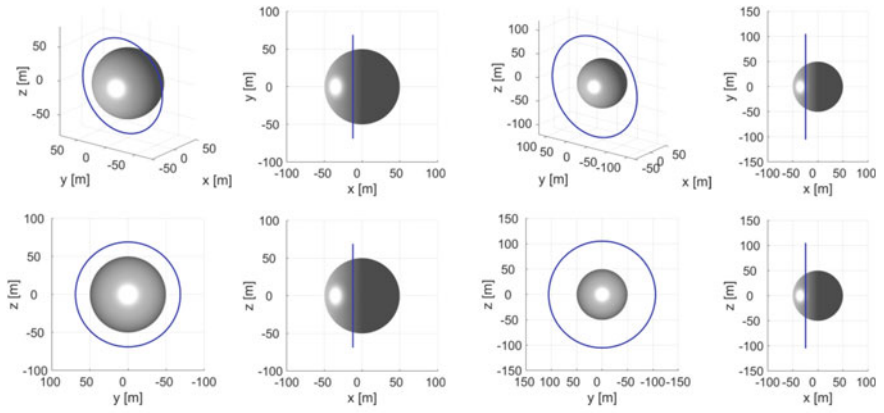

(a) $Q = -30\,\mu C,\ h_0 = 20$ m (b) $Q = -280\,\mu C,\ h_0 = 58$ m

Fig. 2.35 Reference electrostatic periodic orbits for simulations of the attitude motion

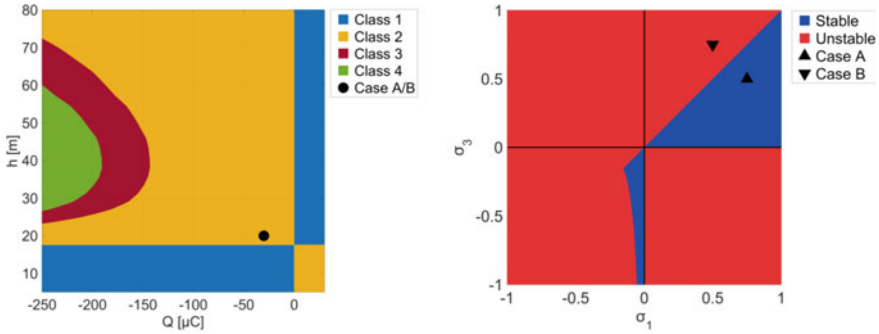

Fig. 2.36 The stability of the attitude motion for cases A and B

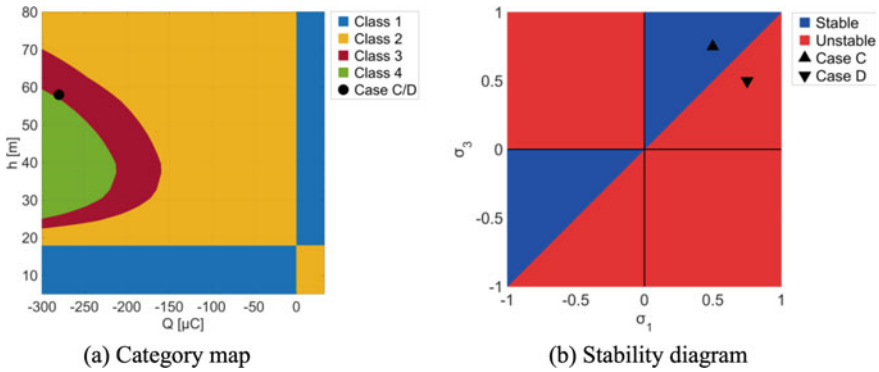

Fig. 2.37 The stability of the attitude motion for cases C and D

equilibrium roll angle that is calculated numerically based on the nonlinear equations of motion. This result demonstrates that an E-Glider can orbit around a small body with a stable attitude motion even under the influence of electrostatic torque. In contrast, Fig. 2.38b illustrates that an unstable set of moment of inertia parameters leads to a large deviation in the Euler angles. Therefore, the shape or orientation of an E-Glider must be designed properly to achieve a stable attitude motion.

Another intriguing result is presented in Fig. 2.38c and d. It can be observed from Fig. 2.38c that although the spacecraft configuration is unstable for the orbit given in Fig. 2.35a, it can achieve a stable attitude motion for the orbit presented in Fig. 2.35b. This result demonstrates that even when the attitude motion of a spacecraft is unstable under gravity gradient torque, it can be stabilized by inducing electrostatic torque. Figure 2.38d shows that a spacecraft that is stable for gravity gradient torque can exhibit an unstable attitude behavior under the electrostatic environment. The simulation results have revealed that the attitude motion of an E-Glider exhibits unique characteristics that cannot be observed in classical attitude dynamics subject

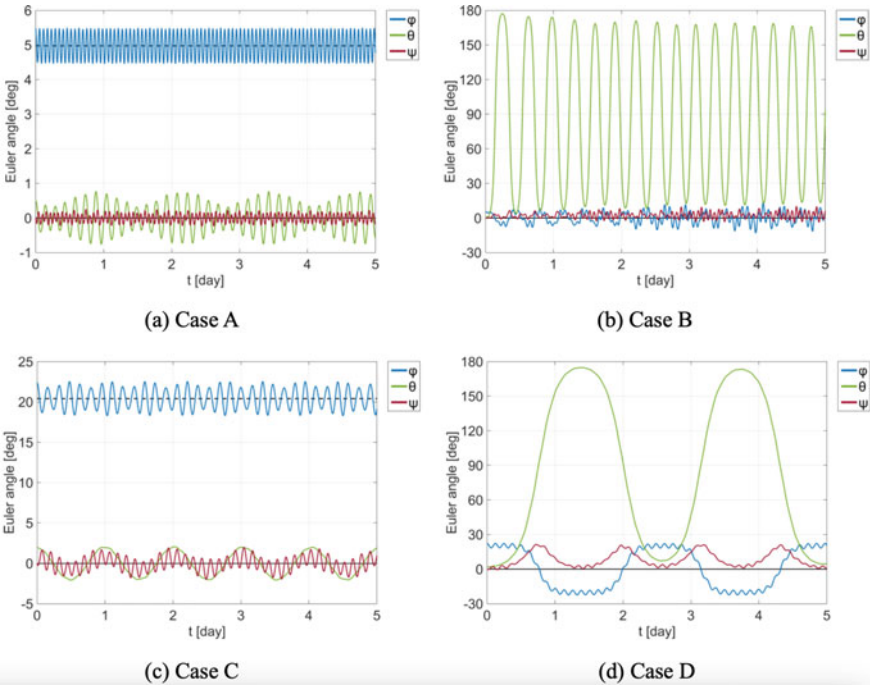

Fig. 2.38 Numerical simulation results of stable and unstable attitude motions

Table 2.4 Simulation conditions for libration and tumbling in the pitch motion

	$\dot{\theta}_0$	$\hat{C}_\theta$	Pitch motion
Figure 2.39a	2×10^{-4} rad/s	0.19	Libration
Figure 2.39b	6×10^{-4} rad/s	1.73	Tumbling

only to gravity gradient torque. Moreover, the simulation results confirm that the numerical simulations agree with the analytical theories discussed in the previous section.

2.12.3 Libration and Tumbling in the Pitch Motion

As described in Sect. 2.11.3, when the roll and yaw motions are in equilibrium states, the pitch motion can be solved independently based on an analytical theory. This section demonstrates the validity of the analytical analysis by performing numerical simulations.

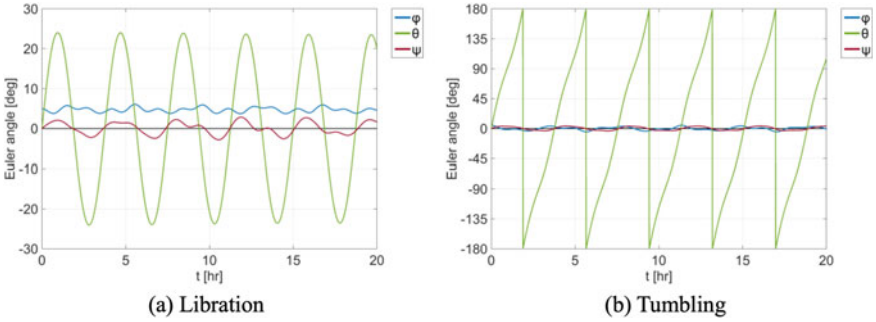

Fig. 2.39 Numerical simulation results of libration and tumbling in the pitch motion

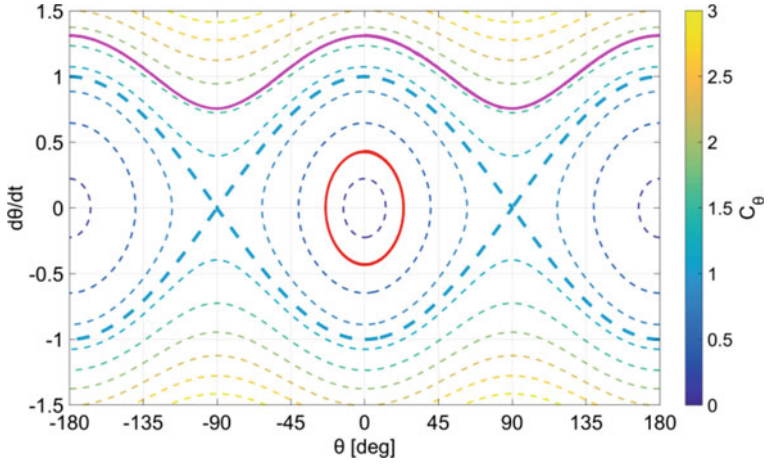

Fig. 2.40 Simulated trajectories in the phase plane for the pitch motion

The simulation is performed for the case A condition presented in Table 2.3, which provides a stable attitude motion. Equation (2.95) indicates that the $\hat{C}_\theta$ value is conserved for the pitch motion, and $\hat{C}_\theta < 1$ corresponds to libration, while $\hat{C}_\theta > 1$ corresponds to tumbling motion. The attitude motion of an E-Glider is numerically simulated for two cases with different initial pitch rates $\dot{\theta}_0$ that involve different pitch motion modes. Table 2.4 provides the simulation conditions, and Fig. 2.39 depicts the simulation results. It can be observed from Fig. 2.39a that when the initial pitch rate is relatively small, the pitch motion exhibits stable libration. On the contrary, Fig. 2.39b shows that a larger initial pitch rate results in tumbling about the pitch axis.

Figure 2.40 illustrates the histories of the pitch motion that are displayed in the phase plane. The trajectories represented as the solid red and magenta lines correspond to Fig. 2.39a and b, respectively. The broken lines show a contour map of the analytically calculated $\hat{C}_\theta$ value, which is also illustrated in Fig. 2.34. Figure

2.40 demonstrates that the numerically calculated trajectories approximately follow the contour lines, and reasonable agreement is found between the analytical theory and the numerical simulations. It is to be noted that both $d\theta/d\hat{t}$ and $\hat{C}_\theta$ described in the figure are nondimensional values that are scaled by the time unit τ given in Eq. (2.94). Because τ is a function of the ξ parameter, the effect of the electrostatic torque implicitly appears in Fig. 2.40. Therefore, these simulation results confirm that the attitude motion of an E-Glider subject to electrostatic torque can be analyzed based on classical approaches by introducing the ξ parameter.

2.13 Hovering and Its Stability

Hovering is a type of active control in which a continuous control thrust cancels out the nominal accelerations acting on the spacecraft (Broschart and Scheeres 2005; Kominato et al. 2006). For the E-Glider, the net charge Q of the spacecraft itself generates thrust or better, a continuous force. The solar radiation pressure has a strong influence on the shape of the orbits near a small body like an asteroid (leading also to the instability in some cases Scheeres and Marzari 2002), due to the weak gravitational attraction. Hovering can be a solution to avoid these problems by eliminating through an active control the accelerations of the spacecraft, thus creating an artificial equilibrium point at a desired location. Until now, fuel restrictions have limited hovering applications, but for the E-Glider, these limitations do not apply, since only the power constraints of the spacecraft will set a limit and not the fuel level. The case of fixed hovering with respect to the Sun has been analyzed in Bechini et al. (2021), Bechini (2020) and discussed here, while the case of hovering over a specific location of an asteroid is not considered (this scenario will be by far more complex due to the alternance of sunlit/shadow phases). Before approaching the hovering problem, we analyzed the zero-velocity curves to better understand the potential field near the asteroid. The equations of motion contain the electrostatic potential term to make this analysis relevant to the E-Glider case. The analysis points out that the Nitter model, used up to now, is not adequate to describe the electrostatic field in close proximity of an asteroid since by using the more refined model provided by the PIC analysis, the identification of new and more equilibrium points with respect to the ones predicted by the Nitter model is possible. This led also to the possibility of identifying stable equilibrium points in subsolar hovering on the sunlit side which is at an altitude of about $10-100$ m from the surface of the asteroid. An E-Glider can hover on these points by using a charge level lower than the one predicted by using the Nitter model. The sensitivity analysis shows that the charge over mass ratio needed to hover grows quadratically with the radius of the spacecraft.

Next, we list the assumptions used to define the case study and under which the obtained results are valid. The bodies in the system under investigation are the Sun, a reference asteroid (considered as the main body) in a heliocentric orbit, and a spacecraft orbiting in close proximity to the asteroid. The main body has a circular

Table 2.5 Reference spacecraft characteristics

Parameter	Value
Shape	Sphere
Radius	0.065 m
Mass	1.33 Kg
C_{pa}	0.14
C_{ps}	0.43
C_{pd}	0.43

heliocentric orbit by assumption; thus, the equations of motion can be written by using the Clohessy–Wiltshire approximation (Curtis 2010).

We assumed the spacecraft as a solid sphere. The mass of the spacecraft is constant and equal to 1.33 Kg (as for a 1U CubeSat CubeSat 2019). The radius of the reference spacecraft is equal to 0.065 m (it is computed from the volume of a sphere equivalent to a 1U CubeSat). The computation of the SRP properties of the spacecraft can be performed by assuming a layer of Mylar with a coefficient of absorptance (C_{pa}) equal to 0.14 (Finckenor 1999) that covers the surface. The coefficients of specular (C_{ps}) and diffuse (C_{pd}) reflection have the same value, equal to 0.43, by assumption. The SRP force is modeled by using the backward ray-casting model. The charge Q is considered as fixed and modeled as a point charge concentrated in the center of mass of the spacecraft; thus, the first moment of charge is zero. Table 2.5 summarizes the spacecraft characteristics.

The main body of these simulations is the reference asteroid used also for the PIC (particle-in-cell) analysis (Yu et al. 2016). The reference main body is a spherical asteroid with a radius of 14 m. The gravity model used is the point mass model with $\mu = 0.0017\ \mathrm{m}^3/\mathrm{s}^2$. The circular heliocentric orbit of the asteroid has a radius of 1 AU and a period of 365.25 days at epoch 2451545 JD. The rotational parameters are assumed to be measured at the same epoch of the orbital parameter. The right ascension of the rotational axis is set to 0°, and the declination is set to 90° with a rotational period of 1°/day. Table 2.6 summarizes the orbital and the rotational parameters of the asteroid.

2.13.1 Zero Velocity Curves

The Clohessy–Wiltshire equations (see Eqs. (2.11) and (2.12)) can be rewritten in the RIC frame as (Curtis 2010):

Table 2.6 Reference asteroid characteristics

Orbital parameters		Rotational parameters	
Epoch	2451545JD	Epoch	2451545JD
Epoch offset	0	Epoch offset	0
Mean anomaly	0	Rotational axis RA	0
Orbital period	365.25 days	Rotational axis DE	90 deg
Semimajor axis	1 AU	Prime meridian position	0
Eccentricity	0	Rotational period	1 deg/day
Inclination	0	**Geometry**	
RA of ascending node	0	Shape	Sphere
Argument of periapsis	0	Radius	14 m
Gravity		**Plasma**	
Gravity model	Point mass	Plasma field	True
Gravitational parameter	$0.0017\,\mathrm{m}^3/\mathrm{s}^2$		

$$\begin{aligned} \ddot{x} - 2N\dot{y} &= -\frac{\partial U}{\partial x} \\ \ddot{y} + 2N\dot{x} &= -\frac{\partial U}{\partial y} \\ \ddot{z} &= -\frac{\partial U}{\partial z} \end{aligned} \tag{2.105}$$

In Eq. (2.105), U is the potential as a function of the position of the spacecraft $\mathbf{r}$. For the case under analysis, the contributions to the total potential are the gravitational effect, the centrifugal effect, and the equivalent potential given by the solar radiation pressure and by the electrostatic potential. Thus,

$$\begin{aligned} -\frac{\partial U}{\partial x} &= 3N^2 x + a_{g,x} + a_{p,x} + \frac{Q}{M}E_x \\ -\frac{\partial U}{\partial y} &= a_{g,y} + a_{p,y} + \frac{Q}{M}E_y \\ -\frac{\partial U}{\partial z} &= -N^2 z + a_{g,z} + a_{p,z} + \frac{Q}{M}E_z \end{aligned} \tag{2.106}$$

By integrating and by assuming a simplified case in which the potential of the SRP force is $U_p = \mathbf{a}_p \cdot \mathbf{r}$ as in Scheeres (1999), the potential can be written as

$$U(\mathbf{r}) = -U_g(\mathbf{r}) - \frac{N^2}{2}\left(3x^2 - z^2\right) + \frac{Q}{M}\phi_e(\mathbf{r}) - \mathbf{a}_p \cdot \mathbf{r} \tag{2.107}$$

where $U_g(\mathbf{r})$ is the gravitational potential (resulting from $\mathbf{a}_g = \nabla U_g$), and $\phi_e(\mathbf{r})$ is the electrostatic potential in $\mathbf{r}$ resulting from $\mathbf{E} = -\nabla\phi_e$. Equation (2.105) can be

written in a more compact form; thus,

$$\frac{\partial^2 \mathbf{r}}{\partial t^2} = -\nabla U \tag{2.108}$$

But

$$\frac{\partial \mathbf{r}}{\partial t} \cdot \frac{\partial^2 \mathbf{r}}{\partial t^2} = -\frac{\partial \mathbf{r}}{\partial t} \cdot \nabla U \tag{2.109}$$

where

$$\frac{\partial \mathbf{r}}{\partial t} \cdot \frac{\partial^2 \mathbf{r}}{\partial t^2} = \mathbf{v} \cdot \dot{\mathbf{v}} = \frac{1}{2}\frac{d^2}{dt} v^2 \tag{2.110}$$

where $\mathbf{v}$ and $\dot{\mathbf{v}}$ are computed in the co-moving frame relative to the co-moving frame. Moreover, we can notice that

$$\frac{\partial \mathbf{r}}{\partial t} \cdot \nabla U = \frac{\partial \mathbf{r}}{\partial t} \nabla U^T = \frac{\partial U}{\partial x}\frac{\partial x}{\partial t} + \frac{\partial U}{\partial y}\frac{\partial y}{\partial t} + \frac{\partial U}{\partial z}\frac{\partial z}{\partial t} = \frac{dU}{dt} \tag{2.111}$$

Thus,

$$\frac{1}{2}\frac{d}{dt} v^2 = -\frac{dU}{dt} \Rightarrow \frac{1}{2}\frac{d}{dt} v^2 + \frac{dU}{dt} = 0 \Rightarrow \frac{d}{dt}(v^2 + 2U) = 0 \tag{2.112}$$

This leads to $v^2 + 2U \doteq C_j$ which is constant and corresponds to an integral of motion (or the Jacobi integral). The total energy can be written as $\frac{1}{2}v^2 + U = E_{TOT}$. Since $v^2 \geq 0$ is always true, $U(\mathbf{r}) \leq C_j$ must hold. This last equation defines a constraint for the allowable regions of the spacecraft. The boundaries of these regions are the zero-velocity curves. The potential $U(\mathbf{r})$ is affected by the spacecraft charge Q (see Eq. (2.107)); thus, an analysis for different levels of Q in proximity to the asteroid allows better understanding of the presence of equilibrium points and the U transitions. The equilibrium points can be obtained by imposing $\frac{d}{dt} = 0$ in Eq. (2.105), resulting in the equilibrium conditions $\frac{\partial U}{\partial x} = \frac{\partial U}{\partial y} = \frac{\partial U}{\partial z} = 0$. The analysis here presented is reduced to the *xy plane* in which the negative x is the sunlit side of the asteroid, with the sunlight coming from the -x-direction.

First, we analyzed the case for $Q = 0\,\mu\text{C}$. The results obtained and shown in Fig. 2.41 are consistent with the ones already presented in Kikuchi (2017). Only one equilibrium point exists in proximity to the asteroid on the dark side. In the equilibrium point, the effect of the SRP plus the centrifugal force (both acting in the +x-direction) counter the effect of the gravitational acceleration of the asteroid. The potential is negative, with negative peaks in proximity to the planet.

Next, we analyzed the case when the spacecraft has a positive charge. In this case, the influence of the charge itself on the potential field is not strong. On average, if the positive charge is increased, the potential field is "pushed" through more negative values. The main behavior in close proximity to the asteroid is not strongly affected by the charge as the potential keeps decreasing through highly negative values as in

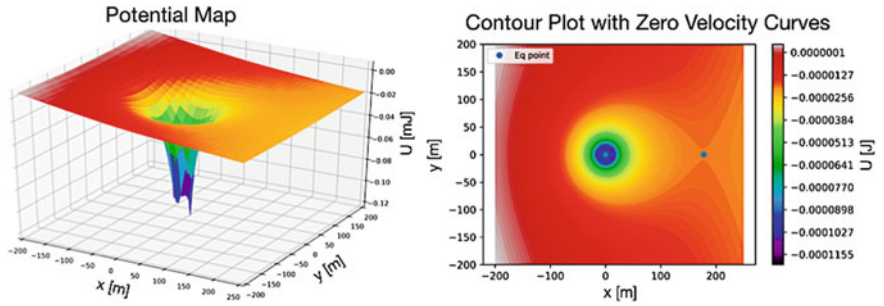

Fig. 2.41 Potential map and zero-velocity curves for Q = 0 μC

the case for $Q = 0$. Figure 2.42 shows the zero-velocity curves plots for the cases of $Q = 15\,\mu\text{C}$ (top), $Q = 25\,\mu\text{C}$ (mid), and $Q = 75\,\mu\text{C}$ (bottom).

The blue dots are the equilibrium positions. The plots on the right column of Fig. 2.42 are the details of the plots on the left computed only for the sunlit region ($-55 \leq x \leq 0$ and $0 \leq y \leq 40$) with a more refined mesh. By looking first at the plots on the left column, we can notice that different levels of positive charge do not have a strong impact on the shape of the potential field. Moreover, the effects of the plasma wake are evident (obviously, they are not present if $Q = 0$, see Fig. 2.41). The modifications in the potential field given by the influence of the plasma are different from the results previously obtained by using the Nitter model (Kikuchi 2017), especially in the terminator line (transition between sunlit side and dark side) and in close proximity to the asteroid surface. By neglecting the infeasible equilibrium point located at $x = y = z = 0$, there is at least one collinear ($y = 0$) equilibrium position on the dark side, far from the surface at about 105−110 m. These equilibrium points disappear (as shown in Fig. 2.42 for $Q = 75\,\mu\text{C}$) if the level of charge reaches high values, in this case, higher than 50 μC. Due to the presence of a photoelectron sheath near the surface of the asteroid, the presence of equilibrium points can be hypothesized for a positively charged spacecraft in this region. To detect these points, we needed an extremely refined mesh, for this reason, the plots on the right column of Fig. 2.42 were produced. These analyses indicated the presence of more equilibrium points. These new equilibrium points are non-collinear (they have $y \neq 0$), and there are more than one non-collinear equilibrium points for the same level of charge Q. This result is the consequence of the complex shape of the electric field near the surface of the asteroid. These points were not detectable with the Nitter model, since it uses an oversimplified model for the electric field computation with respect to the PIC results. The mesh used does not allow us to find collinear equilibrium on the sunlit side, but their presence can be predicted by considering again the photoelectron sheath. The mesh must be extremely fine to detect these points, leading to a strong increment in the computational time. The analyses restricted to the case $y = z = 0$ and $x \neq 0$ reported in the following sections confirm the presence of these equilibrium points at an altitude below ≈ 2 m (altitude at which the electrostatic potential has a minimum, thus an inversion of the sign in E_x), but with a strong

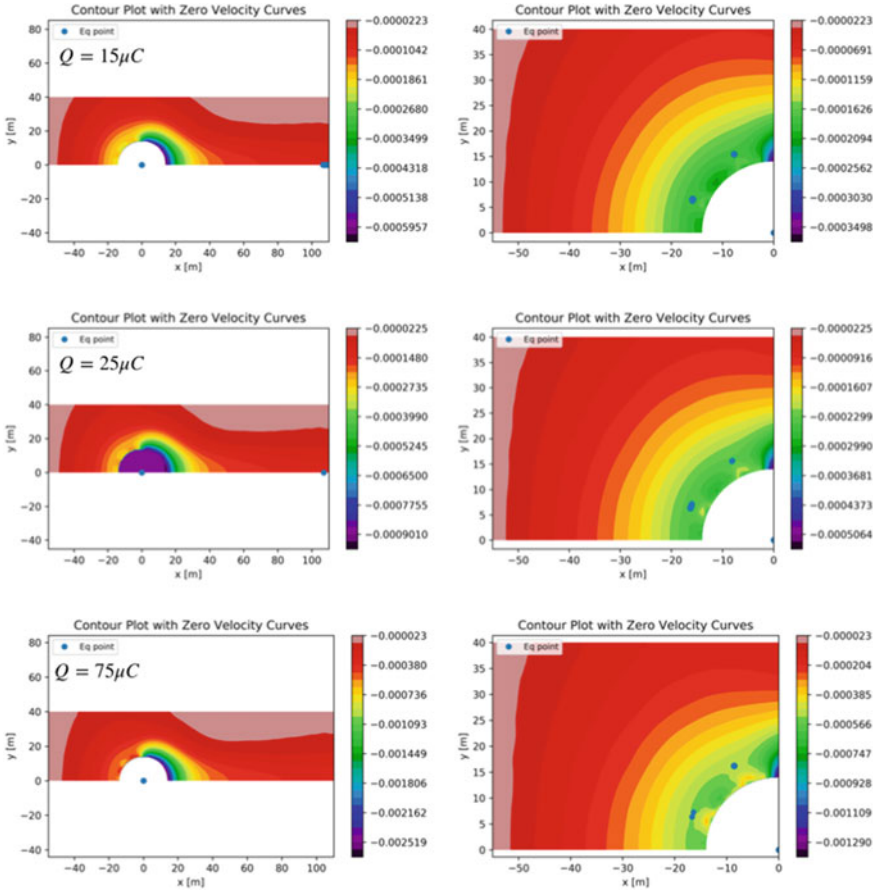

Fig. 2.42 Zero-velocity curves for Q > 0 μC

gradient of variation of Q for small variation in the position x. The non-collinear points obtained are not very sensitive to variations in the charge levels; furthermore, they are still present even for levels of charge in which the dark side equilibrium point has already disappeared. The coexistence (at least for a low level of positive charge) of equilibrium points both on the sunlit side and on the dark side is ensured, with both collinear and non-collinear points on the sunlit side.

Second, we analyzed the case in which the spacecraft has a negative charge. The charge of the spacecraft affects the potential field in a way such that the potential on the sunlit side falls to extremely negative values, while on the dark side, the potential becomes strongly positive in close proximity to the surface. Figure 2.43 shows the zero-velocity curves for the cases of $Q = -5\,\mu C$ (left) and $Q = -10\,\mu C$ (right).

The equilibrium conditions are present both on the sunlit side and on the dark side even for a low level of charge; moreover, there is more than one equilibrium

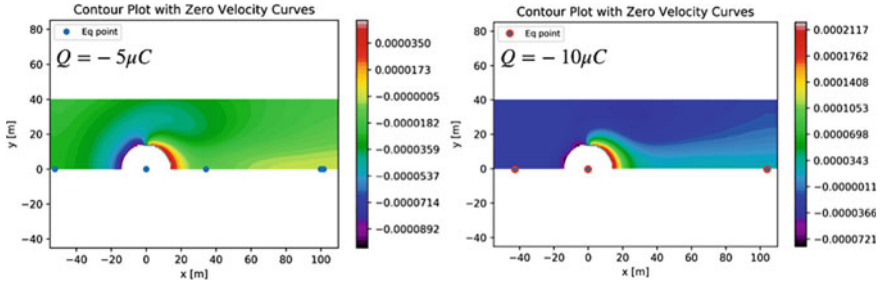

Fig. 2.43 Zero-velocity curves for Q < 0 μC

condition on the same side for the same level of charge. This result is in contrast with the previous study (Kikuchi 2017) based on the Nitter model. By using the Nitter model, the equilibrium conditions were obtained only on one side per time with a negatively charged spacecraft; moreover, the equilibrium conditions on the sunlit side were obtained only for extremely high levels of charge (Kikuchi 2017). A comparison between the equilibrium points on the sunlit side for the two cases reported indicated that the equilibrium points are closer to the asteroid surface for a charge higher in modulus. Also, this result is in contrast with the Nitter theory, where an augmenting negative charge moves the spacecraft far away from the asteroid towards the direction of the Sun (Kikuchi 2017). The detection of equilibrium positions on the sunlit side is affected by the dimensions of the mesh, thus, in this case, to also augment the number of points in the grid without strongly affecting the computational time, some analyses have been performed for the case in which $-55 \leq x \leq 0$ and $0 \leq y \leq 40$ with a more refined mesh. The results are in Fig. 2.44.

There are more equilibrium positions, for the same level of charge, on the subsolar axis, as deduced before. Moreover, several noncollinear equilibrium points (equilibrium points with both x and y different from zero) are present also for a low level of charge. A comparison between the three cases reported in Fig. 2.44 indicated a drift of the equilibrium points for different levels of charge. By making the charge more negative, the collinear equilibrium points move towards the surface of the asteroid until they disappear (see the case of $Q = -25\,\mu C$), while the non-collinear points seem to drift away, and some of them seem to appear and then disappear (a better understanding of this phenomenon can be obtained by using an extremely refined mesh). These results cannot be obtained by using the Nitter model; in particular, the presence of more than one non-collinear equilibrium position has not been assessed before.

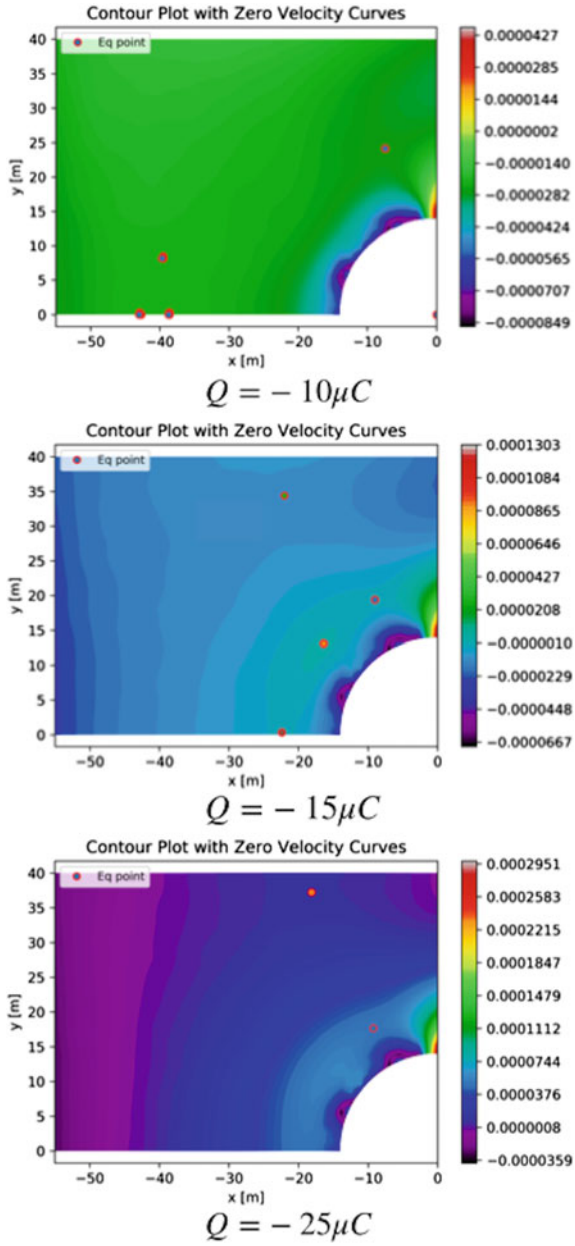

Fig. 2.44 Zero-velocity curves for Q < 0 μC on sunlit side

2.13.2 Subsolar Hovering

The analysis of the zero-velocity curves points out that there are several points of equilibrium dependent from the charge. The analysis was restricted to only the subsolar axis (thus only along the x-direction, with $y = 0$ and $z = 0$) in order to better characterize the equilibrium conditions in this region by achieving a higher accuracy without strongly refining the mesh. The equation for the hovering along the x-axis (Eq. (2.113)) can be derived from the general equation of motion written under the Clohessy–Wiltshire assumptions; thus,

$$3N^2 x + \frac{f_{g,x}}{M} + \frac{f_{p,x}}{M} + E_x \frac{Q}{M} = 0 \tag{2.113}$$

The solution of Eq. (2.113) for Q/M gives the charge over mass ratio needed to hover at each position along the x-axis. The stability has been evaluated for each equilibrium condition. The stability conditions for the case under exam are

$$\frac{\partial U}{\partial x} = 0 \tag{2.114}$$

$$\left.\frac{\partial^2 U}{\partial x^2}\right|_{eq} > 0 \tag{2.115}$$

where the selected Q/M always verifies Eq. (2.114). The x derivative of Eq. (2.113) leads to

$$\frac{\partial^2 U}{\partial x^2} = -3N^2 - \frac{\partial^2 U_g}{\partial x^2} - \frac{\partial a_p}{\partial x} - \frac{Q}{M}\frac{\partial E_x}{\partial x} \tag{2.116}$$

The second derivative of the gravitational potential is computed by using Pines' algorithm with a modified recursion formula (Gottlieb 1993; Pines 1973; Lundberg 1988; Fantino and Casotto 2009). The derivative of the electric field can be numerically computed as the x-component of the gradient of the electrostatic field. The term $\frac{\partial a_p}{\partial x}$ can be neglected since the E-Glider is supposed to fly in close proximity with respect to the asteroid; thus, $\frac{\partial a_p}{\partial x} \approx 0$ can be assumed. The results of this first analysis are reported in Fig. 2.45.

The central gray band in Fig. 2.45 represents the asteroid, and the blue dotted line represents the limit of the nominal photoelectron sheath (which corresponds to the nominal photoelectron Debye length, equal to 1.38 m). Only a few points of stable hovering over the sunlit face exist. These points are at about 42 m from the center of the asteroid and can be interesting from a "real mission" point of view. A negatively charged spacecraft could achieve almost all the hovering conditions, except some positions on the dark side (at more than 100 m of distance from the center of the asteroid) and for altitude below the photoelectron sheath (which are not reported in the figure for scale issues, since these points are located at values even equal to $Q/M = 0.0024$ C/Kg). This analysis, in agreement with the results obtained in

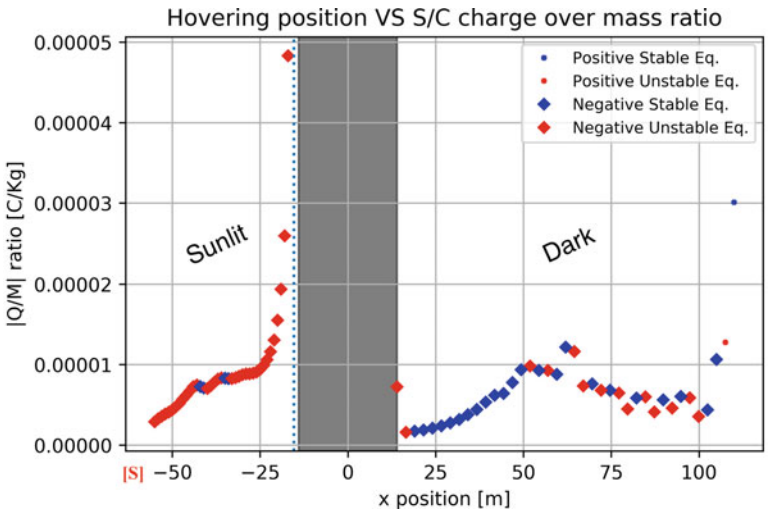

Fig. 2.45 Subsolar hovering conditions

Table 2.7 Radius values for simulations

Reference [m]	Values [m]
0.065	0.1 0.25 0.5 0.75 1.0 2.0 5.0 7.5 10

Corradino (2018), confirmed that in the nominal case, for the assumed spacecraft and main body parameters, the Q/M ratio required for the hovering over the sunlit face is in the order of 10^{-5} C/Kg. A stable hovering at about $10 - 100$ m of altitude is possible by assuming that the levels of power and voltage required are achievable. Moreover, the level of charge needed to achieve the hovering condition in subsolar positions is lower than the one predicted by using the Nitter model (Kikuchi 2017).

A sensitivity analysis of the equilibrium conditions has been performed by changing the value of the equivalent radius of the sphere which represents the spacecraft to improve the characterization of the hovering conditions. The values used for the simulations are reported in Table 2.7.

The reference value is equal to the radius used for the previous analysis. The other parameters are kept fixed, such that only the radius changes. An analytical study has been performed before the numerical analysis. The Q/M equation can be written as

$$\frac{Q}{M} = \left[-3N^2 x - \frac{f_{g,x}}{M} - \frac{f_{p,x}}{M} \right] \frac{1}{E_x} \tag{2.117}$$

By considering the spacecraft as a "point" concentrated in the center of mass of the equivalent sphere, the only term dependent on the radius of the sphere R_{SC} is the SRP force. By using the simple cannonball model (only for the analytical formulation), the derivative of Eq. (2.117) with respect to R_{SC} is

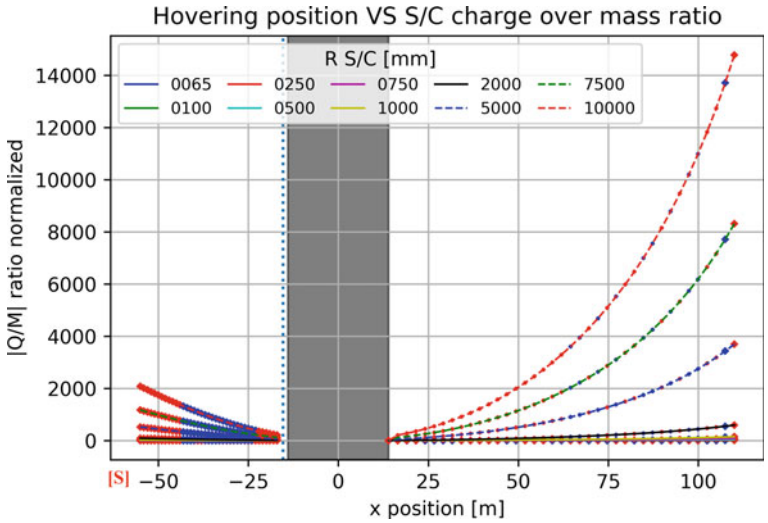

Fig. 2.46 Variation of normalized |Q/M| as a function of R_{SC}

$$\begin{aligned}\frac{\partial Q/M}{\partial R_{SC}} &= \frac{\partial}{\partial R_{SC}}\left(\frac{\Phi}{c}\pi R_{SC}^2\left(C_{ps}+\frac{13}{9}C_{pd}+C_{pa}\right)\hat{\mathbf{s}}\right)\\ &= \frac{\Phi}{c}\pi 2R_{SC}\left(C_{ps}+\frac{13}{9}C_{pd}+C_{pa}\right)\hat{\mathbf{s}}\end{aligned} \tag{2.118}$$

$\frac{\partial Q/M}{\partial R_{SC}}$ is linearly increasing for positive values of R_{SC}; thus, the Q/M needed for the hovering in proximity to an asteroid increases quadratically with the increment of the equivalent radius of the spacecraft (the minimum is achieved for $R_{SC} = 0$ which is a infeasible solution). The numerical results are reported in Fig. 2.46.

The big red marker stands for unstable equilibrium positions achievable with a negative spacecraft charge, while the big blue marker stands for the stable equilibrium positions obtained with a negative charge. The small markers stand for the equilibrium conditions achieved with positive charges (the color code for stable and unstable equilibria is the same). The simplified analytical approach is compliant with the numerical results. The Q/M needed to achieve the hovering condition increases with a quadratic law with the radius of the spacecraft. The Q/M ratios reported in Fig. 2.46 are the absolute value of the ones computed with a prefixed radius in a defined position normalized by the Q/M ratio obtained at the very same position for the reference radius. The normalized $|Q/M|$ increases both on the sunlit and on the dark side by moving away from the surface. The variation of the spacecraft radius does not affect the stable equilibrium region. Figure 2.47 shows that the behavior on the dark side seems to be quite different from the predicted one.

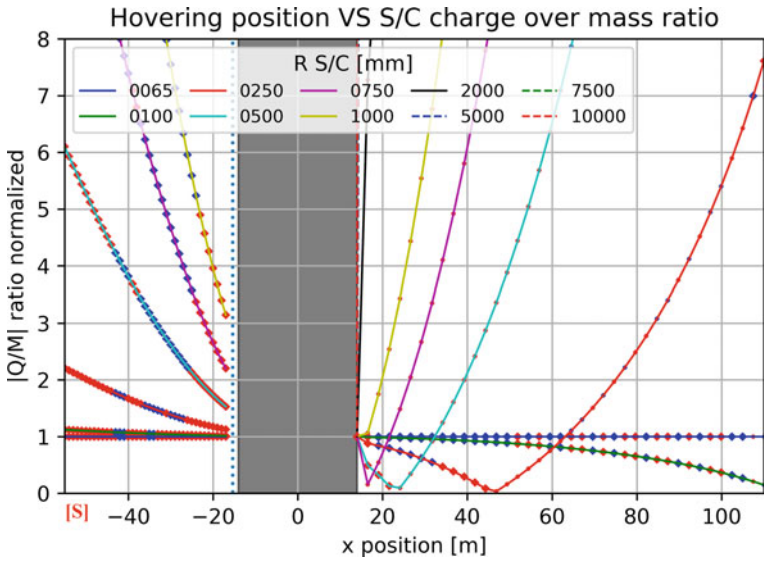

Fig. 2.47 Detail of Fig. 2.46

Table 2.8 Main body positions

Position [AU]	Reason
0.4	Mercury orbit
1.0	Earth orbit
1.5	Mars orbit
2.2	Inner asteroid belt radius
2.75	Mid asteroid belt radius
3.3	Outer asteroid belt radius

The behavior of these curves is due to the fact that the normalized $|Q/M|$ is computed as the ratio between two absolute values. If the radius of the spacecraft increases, the transition from a negative to a positive Q/M ratio (obviously the sign is dictated by the charge Q) is anticipated, as can be seen in Fig. 2.48; For $R_{SC} = 0.065$, the transition happens at ≈ 105 m, while for $R_{SC} = 0.5$ m, the transitions happens at about 25 m from the center of the asteroid. For a radius higher than 1 m, the Q/M needed for the hovering on the dark side is positive for regions close to the asteroid. A second transition region located at about 105 m can be identified in Fig. 2.48. This is due to the electric field x-component that becomes positive.

A sensitivity analysis to evaluate the effects of the position of the main body with respect to the Sun on the $|Q/M|$ ratio has been performed. The five different positions reported in Table 2.8 are considered in this analysis.

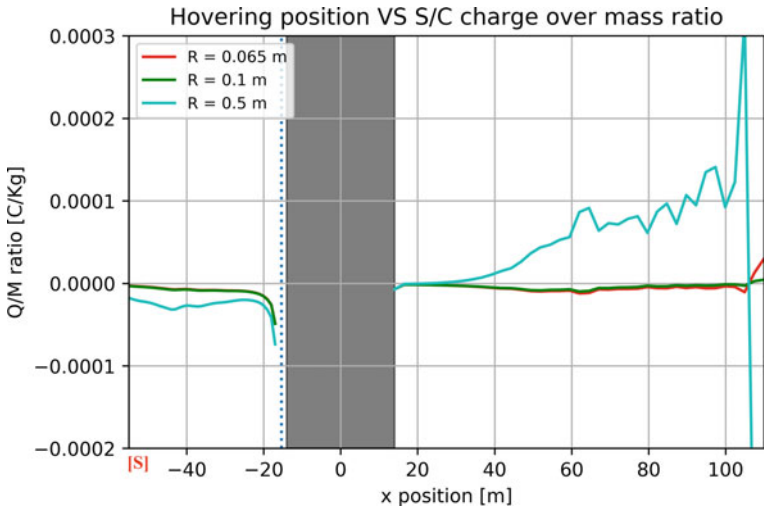

Fig. 2.48 Q/M for the first three cases examined

The positions considered are selected by considering the regions interesting for possible applications of an E-Glider. The case of an asteroid at 1 AU is the reference for the analysis. By changing the distance with respect to the planet, the orbital period (computed in agreement with the selected semimajor axis) and the plasma parameters (the solar wind density and the solar wind ions and electrons temperature) change. The variation of the plasma parameters strongly affects the current collected by the electrodes and the power needed to maintain the charge, but these effects are not considered in this analysis. The results of the numerical analysis are available in Fig. 2.49.

The absolute values of the Q/M obtained for each planet are normalized by the absolute value of the Q/M computed for the reference case. Figure 2.49 indicates that the normalized $|Q/M|$ increases on the sunlit side in the case of an inner asteroid, while it decreases in the case of outer asteroids. Moreover, the increment is higher if compared to the decrements obtained in each case of an outer asteroid. This is due to the strongest effects of the solar wind acting on the sunlit side. By moving away from the asteroid in the direction of the Sun, the difference with the reference case increases by following an exponential law. On the dark side, the trend is the opposite. For an inner asteroid, the Q/M needed switching from negative to positive closer to the surface with respect to both the reference case and the outer asteroids; thus, there is a region (just before the transition) in which the Q/M required is effectively reduced in modulus (see Fig. 2.50). Also, in this case, there is a second transition position located at about 105 m (see Fig. 2.50) from the center of the asteroid, on the dark side region due to the inversion of the sign in E_x. Figure 2.50 confirms that hovering on the sunlit regions requires a higher level of charge for inner asteroids, while on the dark side, the charge required for these asteroids is lower. The solar wind

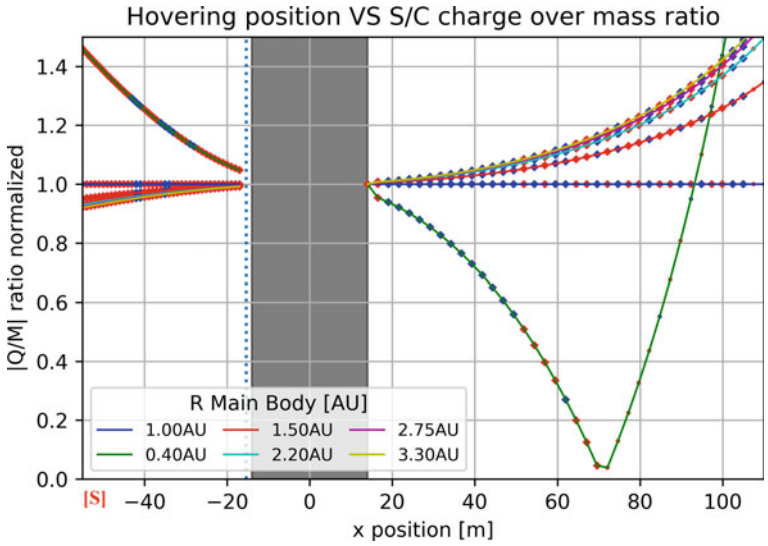

Fig. 2.49 Variation of normalized |Q/M| as function of the asteroid position

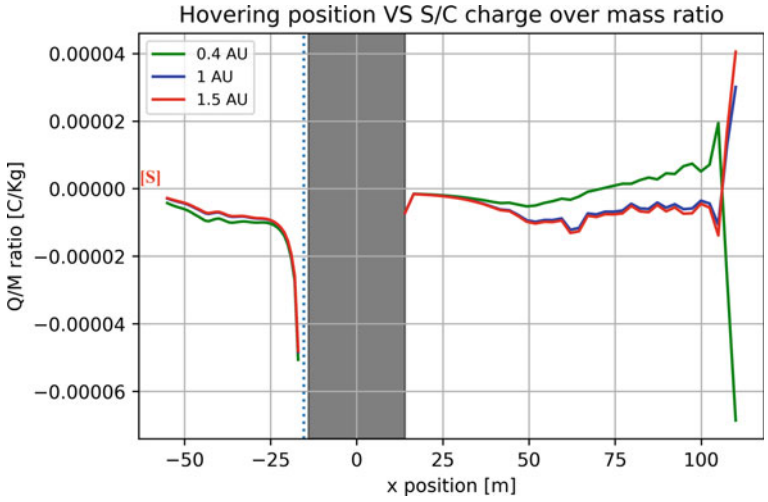

Fig. 2.50 Variation of Q/M as function of the asteroid position

effects on the dark side hovering are quite low for an outer asteroid, since the $|Q/M|$ increment switching from 1.5 AU to 2.2 AU is much stronger than the one computed from 2.2 AU to 3.3 AU (see Fig. 2.49). The positions of the stable equilibria are almost not changed with respect to the reference case (the legend for the equilibrium point is the same of the previous cases).

2.13.3 Electrostatic Periodic Orbit

2.13.3.1 Introduction

Previous works assessed the presence of a class of periodic orbits, called *electrostatic periodic orbits* Quadrelli et al. (2017b), Kikuchi (2017), under the assumption of an electrostatic field modeled with the Nitter model. The previous work that used the PIC results (Corradino 2018) only hypothesized the possibility of achieving the electrostatic periodic orbits without defining them. The electrostatic periodic orbits computed by using the Nitter model are found to have different shapes as a function of the charge. Moreover, assessed was the possibility to have more than one periodic orbit for the same level of charge starting from different initial positions (Kikuchi 2017). These orbits are found to be displaced through the direction of the Sun, allowing the E-Glider to orbit the central asteroid on the sunlit side, thus in a more favorable position with respect to the periodic neutral orbit, which is found to be displaced through the dark side of the asteroid (this can have drawbacks from the mission viewpoint). These orbits, as said, were computed by assuming the Nitter model for the electrostatic field close to the main body. As shown above, the electrostatic field described by the PIC results is much more complex than the one obtained by using the Nitter model, especially for a negatively charged spacecraft on the sunlit side (which is the case for which the electrostatic periodic orbits have been obtained); thus, it is necessary to evaluate if these orbits are still present even if the PIC results are used and/or if they have some modifications from the results obtained by using the Nitter model.

2.13.4 Neutral Periodic Orbit

The natural periodic orbits determination has been used as a benchmark case for testing the algorithm. The natural periodic orbits are periodic orbits in the RIC reference frame characterized by a neutral total charge $Q = 0\,\mu\text{C}$, referred to in the literature as terminator orbits (Quadrelli et al. 2017b; Kikuchi 2017). These orbits are known to be displaced through the dark side of the asteroid. They are Sun-synchronous orbits with the characteristics of being perpendicular to the subsolar axis. Since the neutral orbits are characterized by a charge equal to zero, they are influenced only by the gravitational effects and by the Solar radiation pressure. In Fig. 2.51, shown is an example of a neutral terminator orbit found with the previously described algorithm computed in the RIC reference frame for about $(2.1, 0, 39.94)^T$ as initial position (in meters) and $(0, 0.00656, 0)^T$ as initial velocity (in m/s) propagated for a period of time equal to 10 Earth days using the full-model equation of motion described in Eq. (2.9). From the plot, it can be noticed that the drifting of these orbits is low indeed, and the displacements from the reference initial orbit (the orbit obtained for the first orbital period) are small. The period of the orbit is about 5.48 h. To test

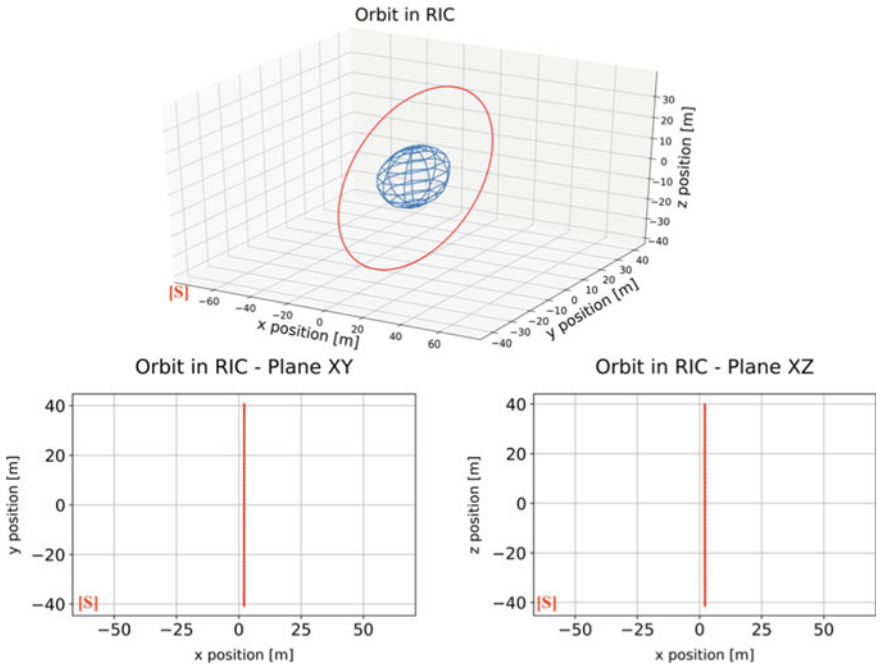

Fig. 2.51 Example of a neutral terminator orbit

the iterative process, the initial conditions that allow us to obtain a neutral periodic orbit have been evaluated. Since the shape and the position of the neutral orbit are influenced only by the gravitational effects and by the SRP, it is expected that a drift of the initial position is needed to obtain a periodic neutral orbit towards the dark side (positive x-direction in the RIC reference frame) if the distance from the center of the asteroid increases. This expectation is fully confirmed by the initial positions computed and reported in Fig. 2.52. The blue line in Fig. 2.52 represents the surface of the asteroid. The maximum displacement computed in the x-direction is about 2.2 m, obtained for $r_0 = 40$ m. These positions are computed by using $\varphi_0 < 90°$ as an initial guess.

2.13.5 Connection with the Electrostatic Periodic Orbit

Once the algorithm was proven to work properly for a neutral orbit, it was used to find the initial condition that allows us to obtain an electrostatic periodic orbit, thus connecting with the previous section where the periodic orbits are described analytically. It has been noticed that the computational cost of this algorithm is extremely high; thus, we reduced the zone of interest in which to select the initial guess con-

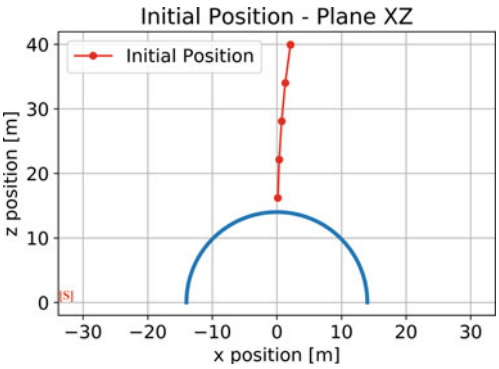

Fig. 2.52 Neutral terminator orbit's initial positions

ditions. The periodicity of an electrostatic orbit can be achieved by exploiting the spacecraft charge level to cancel out the force component along the x-direction in the RIC reference frame. To identify the level of charge over mass ratio needed to cancel out the x-component of the force, it is possible to use Eq. (2.117), here reported for completeness.

$$\frac{Q}{M} = \left[-3N^2 x - \frac{f_{gx}}{M} - \frac{f_{SRPx}}{M} \right] \frac{1}{E_x} \tag{2.119}$$

By evaluating Eq. 2.119 on a domain such that both the x- and the z-directions in the RIC reference frame are different from zero, the searched level of Q/M is obtained. The results of this analysis are reported in Fig. 2.53, while Fig. 2.54

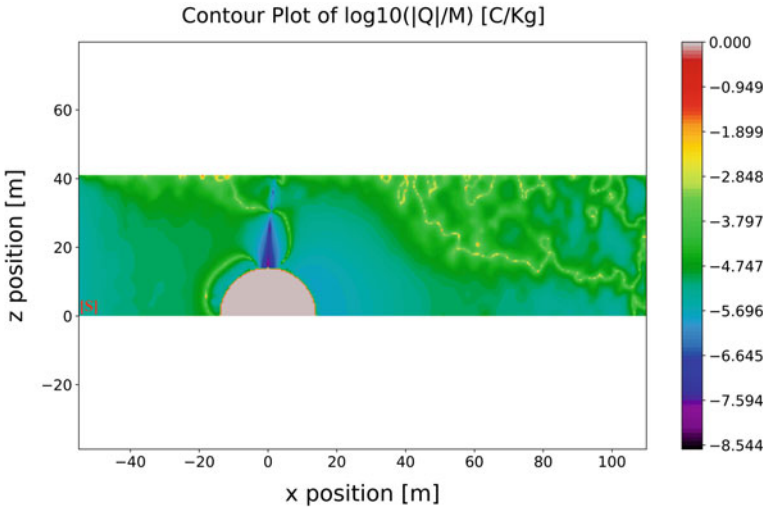

Fig. 2.53 Charge over mass ratio required for orbiting

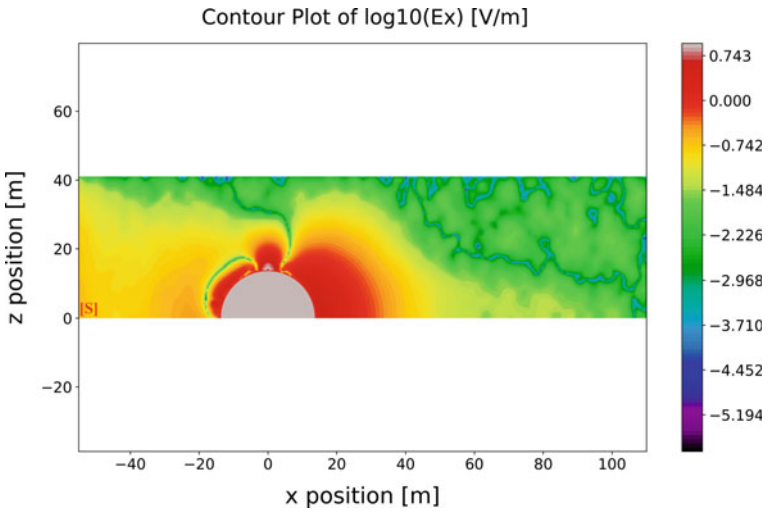

Fig. 2.54 Axial electrostatic field in the xz-plane

presents the level of the axial electric field (along the x-direction) on each point of the evaluation domain of the Q/M ratio.

Figure 2.53 allows us to identify those regions in which the charge over mass ratio required for the orbiting is less than the one required for the subsolar hovering, resulting in a more efficient strategy that can also enable the achievement of more interesting observation points. The sunlit regions that allow for a smaller charge over mass ratio with respect to the hovering case are few and located near the terminator region. This result is expected since the highest strength of the axial electrostatic field is computed above this region (as demonstrated in Fig. 2.54). In Fig. 2.53, the region in which it is possible to establish a periodic neutral orbit can be also found (colored in violet in the figure). It can be noticed that the neutral orbit region obtained in Fig. 2.53 is coincident with the one computed with the previously discussed algorithm and reported in Fig. 2.52. By exploiting these "low-charge" regions, it could be possible to "tug" the orbit in the sunlit direction. It is possible to identify also some regions of low required charge near the subsolar position, in close proximity to the equilibrium points identified when the charge is negative. Anyway, orbiting in these regions can be extremely risky since the favorable regions are surrounded by extremely adverse regions, in which the electrostatic field is weak, thus requiring a high level of charge. Moreover, these regions are close to the surface of the asteroid; thus, in a real case, the perturbations given by the irregularity of the surface itself can be dangerous for the mission. In conclusion, it can be stated that the electrostatic orbiting is advantageous (from the charge over mass ratio point of view) and mainly feasible near the terminator region. Therefore, the selection of the guess initial point can be limited to this region. Furthermore, the charge can also be limited to a level of Q/M lower than the one required for the hovering. This reduction of the zone of interest allows speeding up

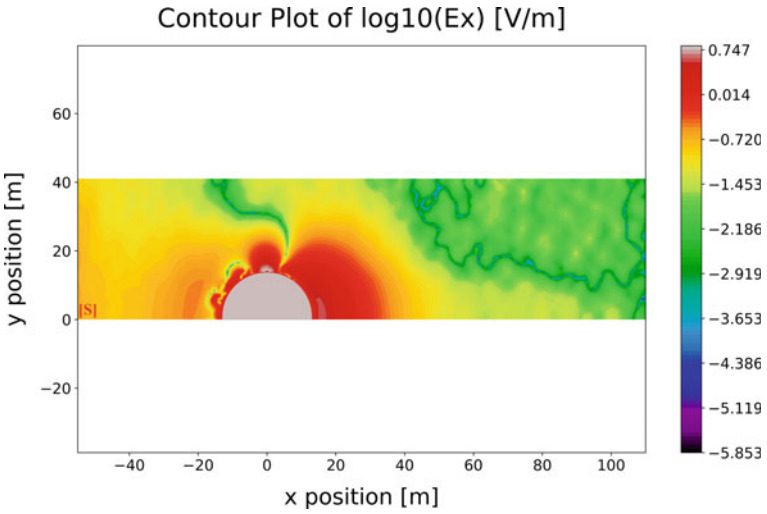

Fig. 2.55 Axial electrostatic field in the xy-plane

the entire process, but the drawback is that the possibility of achieving an electrostatic periodic orbit is not explored nor for regions further from the asteroid surface nor for a higher level of charge. This means that the solution space is not completely explored; thus, a better characterization (with a more powerful algorithm) could be needed to fully explore the solution space. It is better to stress here a main difference between the Nitter model used for past analysis and the model resulting from the PIC method used here. The electrostatic field around a spherical object in a 3D domain can be defined using the Nitter model by computing the field itself on a reference plane (the *xy-plane* in the RIC reference frame for example) and then performing a rotation of 360° of the obtained results around the x-axis. The electrostatic field obtained from the PIC results is computed by interpolating the data that outcome from the numerical analysis on the 3D sector identified by the x-axis and the positive semi-axis of y and z directions in the RIC reference frame. The 3D complete field can then be obtained by mirroring the 3D sector with respect to the *xy-plane* and then with respect to the *xz-plane*. By evaluating the x-component of the electrostatic field on the *xy-plane* (reported in Fig. 2.55) and comparing the results with the ones reported in Fig. 2.54, some variations between the plots are evident. Especially on the sunlit region, the differences between the x-component of the electrostatic field on the *xy-plane* and the one in the *xz-plane* are quite strong in magnitude and shape of the field itself. Thus, the PIC-based model has a higher degree of complexity with respect to the Nitter model since it does not show the rotational symmetry previously discussed for the Nitter model. This loss of symmetry in the numerical results of the PIC analysis can be compared with the Nitter model computed for the case of a slightly ellipsoidal main body in Kikuchi (2017); thus, in this case, an electrostatic field can be obtained which does not have a rotational symmetry about the x-axis

in RIC reference frame. Hence, this "asymmetry" can affect the periodicity of the orbits, also leading to open orbits as reported in Kikuchi (2017).

By running the simulation, it is possible to compute the initial conditions that allow us to obtain those orbits that cross the *xz-plane* perpendicularly. These vectors of initial conditions are stored in an external file compatible with MatLab. This file is post-processed in order to propagate the obtained initial conditions for an entire orbital period and check the distance between the starting point and the final point. This process of evaluation of the obtained orbits is a fast way to verify if they are closed, thus periodic, and if not, how big the distance between the starting and the final condition is. The results of the post-process analysis show that by using a PIC-based electrostatic field model and under the restriction previously reported, in the region of low required charge defined above, there are no periodic electrostatic orbits. This means that it is not possible to obtain a closed periodic orbit displaced through the sunlit direction by imposing a constant negative charge to the spacecraft. The analysis of the obtained distances shows that the smallest deviations (less than 1 m) are obtained for a radius of the starting orbit below 17 m and level of charge of the order of 10^{-7} C. For a higher radius of the initial position, by imposing a charge level lower than 10^{-5} C, deviations lower than 1 m after an orbital period have not been computed. The minimum distance computed is 17 cm obtained for $R_0 = 16$ m, $V_{y0} = 0.0105$ m/s and $Q_0 = -1.9 \cdot 10^{-7}$ C. In the following, the orbit obtained by imposing a charge equal to $Q = -1.6\,\mu$C and a starting distance from the center of the asteroid equal to 21 m is taken as an example. The algorithm gives as initial position the vector $\mathbf{r} = (-3.245, 0, 20.748)$ in meters, and as initial velocity the vector $\mathbf{v} = (0, 6.562, 0)$ in millimeters per seconds. Both $\mathbf{r}$ and $\mathbf{v}$ are expressed in the RIC reference frame. The condition of perpendicularity at the crossing of the *xz-plane* is satisfied since by propagating the orbit for the resulting half-period (which is about 1.94 h) it is obtained in which the x-component of the velocity vector is of the order of magnitude of 10^{-13}, while the z-component is of the order of magnitude of 10^{-14}. The y-component of the velocity at the crossing position is –1.09 cms per second. Thus, the velocity vector results to be perpendicular to the *xz-plane* as expected. The orbit obtained for a propagation of one orbital period is shown in Fig. 2.56.

It is evident that even if the trajectory crosses the *xz-plane* perpendicularly, the orbit results in being an open orbit, thus not periodic. The displacement of the final position with respect to the initial condition is both through the positive x-direction and through the positive z-direction in the RIC reference frame. This result is in agreement with that stated in Kikuchi (2017) for the case of an ellipsoidal main body; thus, the result confirms that the loss of a degree of symmetry given by the PIC results affects the possibility of defining electrostatic periodic orbits, as previously hypothesized. The main cause of the asymmetry is thus in the electrostatic field in which the spacecraft moves along its orbit. The electrostatic field components along the orbit under analysis for one orbital period are reported in Fig. 2.57.

From Fig. 2.57, it can be noticed that in correspondence with the half-period, the electrostatic field components have a strong modification (with a high gradient) with respect to the instant of time just before and just after the crossing of the *xz-plane*.

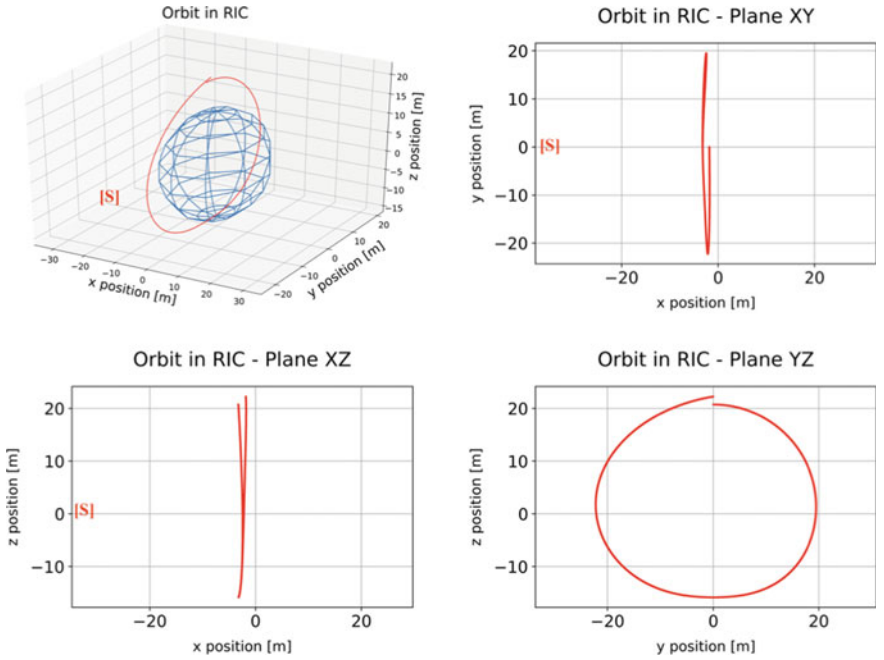

Fig. 2.56 Electrostatic orbit

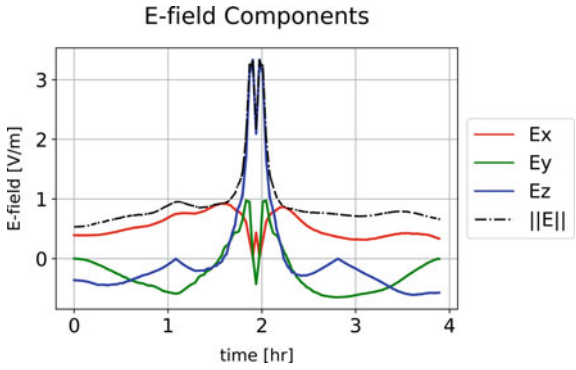

Fig. 2.57 Electrostatic field components along the orbit

This modification has an effect on the electrostatic force acting on the spacecraft. Like in the motion of a pendulum, to have periodicity in the trajectory, it is required that the resultant of the forces acting in the out-of-plane direction is zero when the pendulum is in the vertical position in order to avoid perturbations in the trajectory and thus rotations of the plane of motion and loss of periodicity. The same must be verified for the orbital motion here considered, but due to the shape of the electrostatic

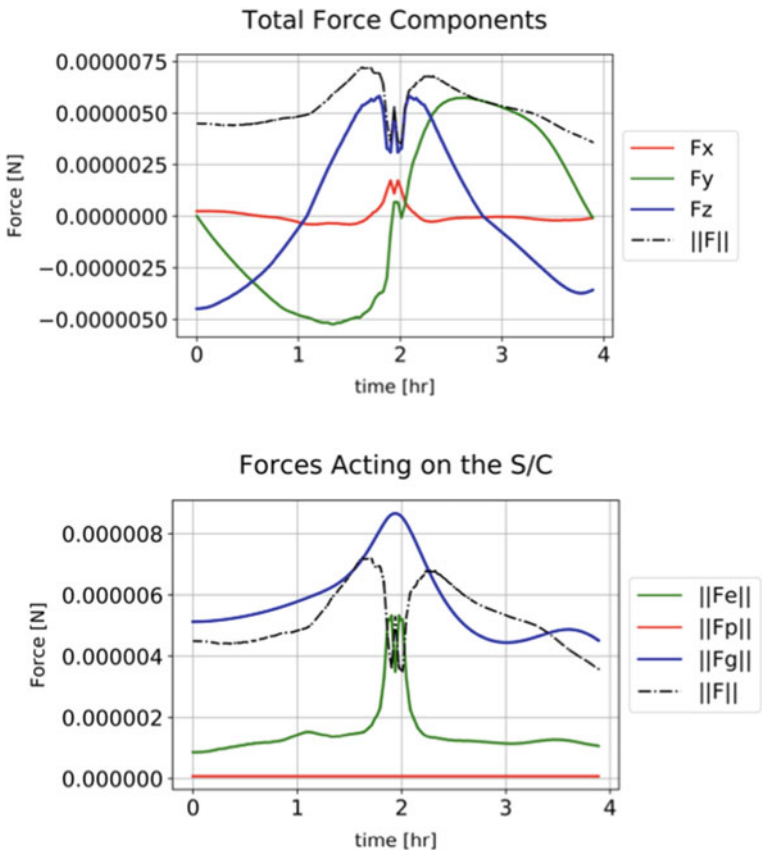

Fig. 2.58 Total force components along the orbit (top) and norm of the forces acting on the spacecraft (bottom)

field, the balance between the forces acting in the x-direction (but also along the z-direction) in the RIC reference frame is not satisfied, as can be noticed in Fig. 2.58 in the upper plot. The non-zeroing of the force component along the x-axis in the RIC reference frame and the unbalancing of the forces along the z-direction cause the displacement of the final point with respect to the initial position and the asymmetry of the orbit and thus of the resultant of the forces on the spacecraft (as can be noticed in the plot on the bottom in Fig. 2.58).

2.14 Control

2.14.1 Control Approach

Key characteristics of small-body targets are lower gravity and lack of atmosphere. The low gravity allows for (1) longer timelines for surveillance and characterization of the target site, (2) gradual descent to the target, (3) multiple landings or contacts and ascent, and (4) aborting and restarting during critical activities. Low-gravity maneuvering differs fundamentally from high gravity in the timescales, requirement for high thrust, and the need for closely monitoring the trajectory and attitude-control loops. An important characteristic of these missions is the lack of a priori information about the body. *JPL's* AutoNav (Quadrelli and Bhaskaran 2019) is ideally suited for E-Glider operations and is capable of achieving position control to within 3 m and horizontal velocity control better than 2 cm/s. Landmark-based autonomous navigation with terrain relative navigation (TRN) and hazard detection and avoidance (HDA) will be necessary for the E-Glider to reach critical landing sites of high scientific interest that are surrounded by terrain hazards. TRN is an image processing method that extracts kinematic position (and optionally attitude) information from onboard sensor data (e.g., camera images, LIDAR range image/map, etc.) for subsequent use in an estimation filter. HDA is a landing function that uses data collected onboard to identify safe landing sites in real time as the vehicle descends. The NEAR and Hayabusa asteroid landings demonstrated that such missions are feasible using ground-in-the-loop navigation at tens of meters of accuracy. Future proximity operations and landings on small bodies may need to achieve accuracies of less than 5 m. A typical timeline for the E-Glider, in the context of a small-body mission, is discussed next. Once released, the vehicle extends its wings and hovers. Through an array of Langmuir probes that measure the spatial distribution of the charges surrounding the vehicle, a map of the local electrostatic field is generated. This map is the result of the differentials between the model and the measurements which are continuously updated in flight. Once the electric potential has been mapped, the E-Glider is able to use this electrostatic topographic map for path planning and navigation. Further articulation of the electrodes would generate a component of lift depending on the articulation angle. This selective maneuvering capability would lead to electrodynamic (rather than aerodynamic) flight. In this context, a potential field approach to path planning for navigation (Quadrelli et al. 2004) is a likely candidate. For navigation, the important determination is which low-altitude ranging sensors (i.e., altimetry) would be needed closer to the ground, if it would be more advantageous for the E-Glider to descend/ascend cyclically in response to solar illumination condition, or what is needed for stable station keeping. Another concern is how to differentially bias the charge on the surfaces relative to the body being orbited since solar wind can cause charge neutralization within a fraction of a second on exposed spacecraft surfaces. To provide continually varying charge emission to control the spacecraft potential relative to the space environment and asteroid, proper orbital design will significantly mitigate this concern by leveraging the natural charging, first hovering

in the dark side (where both the E-Glider and the surface are charged negatively) and then approaching the positively charged surface in the sunlit side at much lower altitude when both the E-Glider and the surface are charged positively. E-Glider navigation requires a local measurement of the direct current (DC) electric field near the spacecraft (and a feedback loop for control). Measuring DC electric fields requires double-probe sensors on long deployable booms (typically 30 m or more in 1-AU solar wind). These measurements are a function of the spacecraft's electrostatic environment including photo- and secondary emission, current bias setting, etc.

In the rest of this section, we consider the E-Glider as an extended body, particularly a dipole. We examine the possibility for a dumbbell E-Glider to achieve a hovering position with a desired attitude on the sunlit side in the RIC reference frame starting from a given initial position. Since the equations of translational motion and the ones of the attitude motion are highly coupled for a dumbbell spacecraft, the assessment of the capabilities of an E-Glider to perform both attitude and orbital control together by exploiting the electrostatic force and torque is fundamental. The coupled control is here developed for the planar case. An initial attempt to control a point mass E-Glider by acting on both the net and the differential charges has been performed in Corradino (2018) but under strong assumptions (e.g., the linearity of the electrostatic field). In this work, the case in which the spacecraft is composed by separated electrostatically active masses linked by a rigid tether controlled by adopting a control strategy similar to the one presented in Corradino (2018) is investigated. The problem is reduced to the planar case by considering only the *xy-plane* in the RIC reference frame.

2.14.2 Assumptions of the Hovering Dipole Model

The system can be represented in the planar case as in Fig. 2.59. The position of the center of mass $\mathbf{R}_c$ and the attitude angle ψ, defined as the angle between the x-direction in the RIC reference frame and the x-direction in the BF reference frame (see Fig. 2.59), describe the system under investigation.

The objective is the achievement of a desired hovering configuration defined by $\mathbf{R}_{cd}$ and ψ_d starting from a given initial position $\mathbf{R}_{c0}$ and ψ_0. The hovering conditions have been previously found under the assumption of the Clohessy–Wiltshire equations (see Sect. 2.13.2). Here, the RIC reference frame is used to derive an ideal control law, but the terms related to the heliocentric motion of the spacecraft have been neglected; since the order of magnitude of the apparent forces given by the non-inertial RIC reference frame is as low as their effects result in a periodic motion with a characteristic time of about one Earth year, they can be safely neglected in first approximation.

The equations of motion (and so all the terms related) are reduced to the 2D case (only x- and y-components). The electrostatic effects can be modulated by changing the charge of the two point masses A and B. To achieve the desired hovering condition, the total resultant charge must be at least equal to the one obtained in

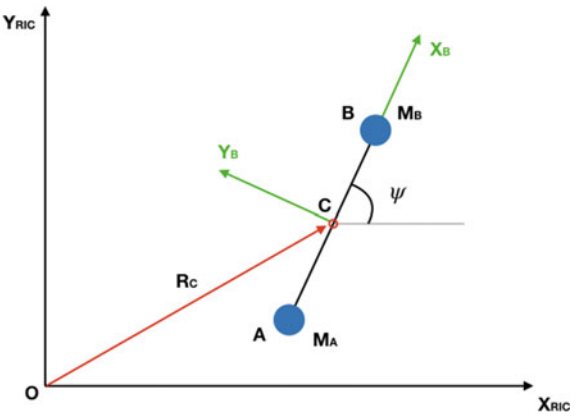

Fig. 2.59 Reference frame for the control analysis

the previous analysis for the case of a point mass spacecraft (see Sect. 2.13.2). Hence, $Q_d = Q_{Hover}$, where Q_{Hover} can be computed by evaluating Eq. (2.117) at the desired final position and configuration. The level of charge that allows the E-Glider to electrostatically levitate at each position over the asteroid on the sunlit side must be evaluated at each instant of time. The level of charge needed to hover at the current position and the one needed to achieve the final hovering can be decoupled by writing $Q(t) = Q_d + dQ(t)$, where $dQ(t)$ is the net charge control variable.

Dumbbell spacecraft can be considered as a single dipole immersed in the electrostatic field given by the PIC analysis. The basic physics of an electric dipole indicates that the first moment of charge can be obtained by differentially charging the endpoints of the dipole itself, hence, by differentially charging A and B. By assuming, for example, a charge -q on mass A and +q on mass B, a dipole moment defined as $S_q = qL$ is generated. The electric dipole moment acts on the direction from the negative to the positive charge (along the x-direction in BF reference frame); thus, it can be expressed in RIC frame components as

$$\begin{aligned} S_{q,x} &= qLcos\psi \\ S_{q,y} &= qLsin\psi \end{aligned} \tag{2.120}$$

If the differential charge on A is the positive one, the dipole moment acts in the –x direction in a BF frame. The differential charging affects at the same time the dynamics of the position of the center of mass and the attitude dynamics, since the dipole moment generated tends to align the spacecraft with the local electric field (generating the rotational effects given by $\mathbf{S}_q \times \mathbf{E}(\mathbf{R}_c)$), but it also gives a translational component since the E-field is a local property. By adopting the formulation derived in Sect. 2.9.1, the electrostatic acceleration can be expressed as

$$\frac{\mathbf{f}_e}{M} = \frac{\mathbf{Q}}{M}\mathbf{E}(\mathbf{R}_c) + \mathbf{G}_e(\mathbf{R}_c)\frac{\mathbf{S}_q}{M} \tag{2.121}$$

where $M = M_A + M_B$, $Q = Q_A + Q_B$, $\mathbf{E}(\mathbf{R}_c)$ is the 2D electric field evaluated at $\mathbf{R}_c$, and $\mathbf{G}_e(\mathbf{R}_c)$ is the 2D electrostatic gradient tensor evaluated at $\mathbf{R}_c$. Equation (2.121) shows how both the net and the differential charge affect the translational motion of the center of mass.

Since the reference frame used is the RIC reference frame and since the analysis is reduced to the planar case, the solar radiation pressure affects only the motion in the x-direction in the RIC frame by assumption. Due to the rigid dumbbell spacecraft model adopted for the E-Glider, both the total gravitational force acting on the equivalent mass M located on the center of mass and the effects of the decentralized masses M_A and M_B given by the gravity gradient term $\mathbf{G}_g$ must be considered. This last contribution can be expressed as (Beletsky and Lavin 1993)

$$\mathbf{G}_g = \frac{3\mu}{R_c^4}\left[\frac{1}{2}(J_{yy} + J_{zz}) - J_{xx};\, J_{xy};\, J_{xz}\right]^T \tag{2.122}$$

where

$$J_{ii} = M_A i_A^2 + M_B i_B^2 \text{ with } i = x, y, z$$
$$J_{ij} = M_A i_A j_A + M_B i_B j_B \text{ with } i = x, y, z \text{ and } i \neq j$$

with *x, y, z* components of the vector $\mathbf{r} = \mathbf{R} - \mathbf{R}_c$ in the local vertical/local horizontal (LVLH) reference frame with the $\mathbf{R}$ position vector in the ACI reference frame of the part considered. Hence, $\mathbf{f}_g = -\frac{\mu M}{R_c^3}\mathbf{R}_c + \mathbf{G}_g$. Also in this case, the vector and the tensor must be reduced to the 2D case by taking only the components related to the x- and y-axis.

The Euler equation previously discussed can be used for the rotational motion. By assuming that the angular rate of the spacecraft with respect to the inertial reference frame expressed in the body reference frame is $\boldsymbol{\omega} = (0, 0, \dot{\psi})^T$ and by assuming that the BF reference frame is aligned with the principal axis of inertia, we obtain that $\mathbf{J}\boldsymbol{\omega} \times \boldsymbol{\omega} = 0$. Thus, the cardinal equation for the rotation around the z-axis in the BF frame can be written as $J_{zz}\ddot{\psi} = T_z$. Solar radiation pressure torque is assumed to be negligible in this analysis, while the electrostatic torque can be computed as $T_{e,z} = \mathbf{S}_q \times \mathbf{E}(\mathbf{R}_c) + T_{eG,z}$ (see Sect. 2.9.1). $\mathbf{S}_q \times \mathbf{E}(\mathbf{R}_c)$ gives the effect of the dipole moment which tends to align the dipole itself with the local electrostatic field, while $T_{eG,z}$ is the third element of the vector $\mathbf{T}_{eG}$. The vector $\mathbf{T}_{eG}$ is defined by the second moment of charge $\mathbf{I}_q$; thus, it depends on the level of charge of the spacecraft. From geometric considerations, we can easily verify that $\mathbf{I}_q$ is symmetric for a dumbbell spacecraft. Moreover, $I_{q,yy}$ and $I_{q,zz}$ are always equal for the spatial symmetry of both the masses and the charges.

If the problem is reduced to the planar case, the vector $\mathbf{T}_{eG}$ has only the component $T_{eG,z}$ different from zero. In order to develop an electrostatic control system based on the charge level of the points A and B, $T_{eG,z}$ must be formulated as an explicit function of the charge Q (since the terms related to the differential charge are auto-balanced). By starting from the computation of $\mathbf{I}_q$ and after some mathematical

steps, we can write $T_{eG,z} = G_{e,xy}(\mathbf{R}_c)\frac{L^2}{4}Q$. This equation indicates that the higher the distance between the charges, the higher the torque given by the electrostatic gradient. By considering the symmetry relations and by remembering that we are analyzing the planar case, we can write the z-component of the gravitational torque as $T_{g,z} = G_{g,xy}(\mathbf{R}_c)(J_{yy} - J_{xx})$. The coupled equations of motion can be written as

$$
\begin{aligned}
{}^r\ddot{\mathbf{R}}_c &= -\frac{\mu}{R_c^3}{}^r\mathbf{R}_c + \frac{{}^r\mathbf{G}_g}{M} + \frac{{}^r\mathbf{f}_p}{M} + \frac{{}^r\mathbf{E}({}^r\mathbf{R}_c)}{M}Q + \frac{{}^r\mathbf{G}_e({}^r\mathbf{R}_c)}{M}{}^r\mathbf{S}_q \\
\ddot{\psi} &= {}^bG_{g,xy}({}^r\mathbf{R}_c)\left(\frac{J_{yy} - J_{xx}}{J_{zz}}\right) + {}^bG_{e,xy}({}^r\mathbf{R}_c)\frac{L^2}{4J_{zz}}Q + \left({}^b\mathbf{S}_q \times {}^b\mathbf{E}({}^r\mathbf{R}_c)\right)\frac{1}{J_{zz}}
\end{aligned}
\tag{2.123}
$$

In Eq. (2.123), the equations for the translation are in the RIC reference frame, while the equation for the rotation is in the BF frame. The electrostatic effects depend on both Q and $\mathbf{S}_q$, which can be assumed to be the inputs of the system (even if the real control variables are the net charge Q and the differential charge q); thus, the redefinition of the equation of motion as an explicit function of Q and $\mathbf{S}_q$ is needed in order to properly formulate a control law. This implies that $\mathbf{S}_q$ must be written in a common reference frame, or the RIC or the BF frame for all the equations. For the planar 2D case, the RIC reference frame and the BF reference frame have the z-axis in common, such that the rotation matrix that allows switching from the inertial to the body reference frame ${}^b\mathbf{R}_r$ is the elementary rotation matrix about the z-axis of an angle ψ. By defining ${}^b\mathbf{T}_e = {}^b\mathbf{S}_q \times {}^b\mathbf{E}({}^r\mathbf{R}_c)$, we can write ${}^b\mathbf{T}_e = {}^b\mathbf{R}_r{}^r\mathbf{T}_e$ with ${}^r\mathbf{T}_e = {}^r\mathbf{S}_q \times {}^r\mathbf{E}({}^r\mathbf{R}_c)$. In the RIC reference frame, for the case under analysis, we have ${}^r\mathbf{S}_q = ({}^rS_{q,x}, {}^rS_{q,y}, 0)^T$, thus ${}^r\mathbf{T}_e = (0, 0, {}^rE_y{}^rS_{q,x} - {}^rS_{q,y}{}^rE_x)^T$. By applying the rotation matrix ${}^b\mathbf{R}_r$ to ${}^r\mathbf{T}_e$, we can verify that since the ${}^r\mathbf{T}_e$ has only the z-component different from zero and since the RIC and the BF reference frames have the z-axis in common, ${}^b\mathbf{T}_e = (0, 0, {}^rE_y{}^rS_{q,x} - {}^rS_{q,y}{}^rE_x)^T = {}^r\mathbf{T}_e$; thus, Eq. (2.123) can be rewritten by switching $\mathbf{S}_q$ from the BF frame to the RIC reference frame (to obtain ${}^r\mathbf{S}_q$ in all the equations) as

$$
\begin{aligned}
{}^r\ddot{\mathbf{R}}_c &= -\frac{\mu}{R_c^3}{}^r\mathbf{R}_c + \frac{{}^r\mathbf{G}_g}{M} + \frac{{}^r\mathbf{f}_p}{M} + \frac{{}^r\mathbf{E}({}^r\mathbf{R}_c)}{M}Q + \frac{{}^r\mathbf{G}_e({}^r\mathbf{R}_c)}{M}{}^r\mathbf{S}_q \\
\ddot{\psi} &= {}^bG_{g,xy}({}^r\mathbf{R}_c)\left(\frac{J_{yy} - J_{xx}}{J_{zz}}\right) + {}^bG_{e,xy}({}^r\mathbf{R}_c)\frac{L^2}{4J_{zz}}Q + \left({}^r\mathbf{S}_q \times {}^r\mathbf{E}({}^r\mathbf{R}_c)\right)\frac{1}{J_{zz}}
\end{aligned}
\tag{2.124}
$$

2.14.2.1 Proportional-Derivative (PD) Active Control

In an initial analysis, a proportional-derivative (PD) controller has been selected to command the required accelerations that must be given to reach the desired configuration. The PD receives as input the state vector of the errors, composed of the error itself (given by the difference between the position at a given instant of time and the reference position) and its time derivative and gives as output the required

accelerations by scaling by a factor K_P the error and by a factor K_D the error time derivative. A PD controller has been used for each variable in the analysis proposed, so the system can be assumed to be composed by three parallel PDs, each one with its own K_P and K_D parameters to be tuned. The parameters of each PD controller have been selected by starting from reference values (Corradino 2018) and then adjusted for the case under analysis by using the trial-and-error method. The outputs of the PDs are the inputs of an ideal actuator which processes these demanded accelerations in order to obtain the net charge and the differential charge needed. The control system is thought to shift the spacecraft from an equilibrium condition (artificially generated by tuning the value of Q) to the next one, hence starting from $\mathbf{R}_{c0}$ to $\mathbf{R}_{cd}$. The total charge is considered as $Q = Q_d + dQ$ such that $\ddot{\mathbf{R}}_c(\mathbf{R}_c, Q, q) = \ddot{\mathbf{R}}_{cd}(R_{cd}, Q_d, 0) = 0$. The control equations are derived by assuming that $\mathbf{R}_{c0}$ is close to $\mathbf{R}_{cd}$ (small displacements) such that once that the error state vector is processed by the PD block, the following control equations can be written:

$$\begin{Bmatrix} \Delta\ddot{x}_c \\ \Delta\ddot{y}_c \\ \Delta\ddot{\psi} \end{Bmatrix} = \begin{bmatrix} \frac{{}^rE_x}{M} & \frac{{}^rG_{e,xx}}{M} & \frac{{}^rG_{e,xy}}{M} \\ \frac{{}^rE_y}{M} & \frac{{}^rG_{e,yx}}{M} & \frac{{}^rG_{e,yy}}{M} \\ {}^bG_{e,xy}\frac{L^2}{4J_{zz}} & \frac{{}^rE_y}{J_{zz}} & -\frac{{}^rE_x}{J_{zz}} \end{bmatrix} \begin{Bmatrix} dQ \\ S_{q,x} \\ S_{q,y} \end{Bmatrix} \tag{2.125}$$

where $\boldsymbol{\Delta}\ddot{\mathbf{R}}_c = (\Delta\ddot{x}_c, \Delta\ddot{y}_c, \Delta\ddot{z}_c)$ and $\Delta\ddot{\psi}$ are the demanded accelerations given by the PDs. From simple geometrical relations, we can derive the equation in matrix form that relates the first moment of charge in the RIC reference frame to the differential charge q. Thus,

$$\begin{Bmatrix} dQ \\ S_{q,x} \\ S_{q,y} \end{Bmatrix} = \begin{bmatrix} 1 & 0 \\ 0 & Lcos\psi \\ 0 & Lsin\psi \end{bmatrix} \begin{Bmatrix} dQ \\ q \end{Bmatrix} \tag{2.126}$$

By defining as $\mathbf{A}$ the matrix that relates the output of the PDs to the vector $(dQ, S_{q,x}, S_{q,y})^T$ and naming $\mathbf{B}$ the matrix that links the vector $(dQ, S_{q,x}, S_{q,y})^T$ with the net charge and the differential charge, we can compute the ideal actuator equations by computing the pseudoinverse of the 3×2 $[\mathbf{A} \cdot \mathbf{B}]$ matrix.

2.14.3 Ideal Hovering Control for a Single-Dipole Spacecraft

The simulations are run by considering a spacecraft composed by identical spheres (which are the "point masses") of 0.065 m of radius linked by a tether such that the distance between the center of mass (and charge) of sphere A from the center of mass (and charge) of sphere B is 10 m. The gravity model used for the asteroid is the point mass model. The ideal control developed relies on the fact that the inertia matrix of the spacecraft is perfectly known. The exact knowledge of the inertia matrix can be an issue for a long-term mission or for objects which stay in space for a long period of time. The measurements of the state of the system (thus position, velocity,

and acceleration of both the center of mass and the angular coordinate) are exact by assumption. Moreover, the electrostatic field and its gradient at each instant of time and for each position are assumed to be exactly known. This last assumption can be extremely difficult to be satisfied in practical cases since even if there is the capability of measuring the electrostatic field at each position through some Langmuir probes (Chen 2003), the time needed to know the electrostatic field must be infinitesimal, and the electrostatic field may also change as a function of time. Lastly, the control system is assumed to be capable of determining the needed net and differential charges instantaneously and the actuator to be capable of providing them to the system itself in a short period of time. The masses are supposed to have the capability of assuming a certain level of charge as it is transmitted as input, without time delays. To make the ideal actuator model more realistic, a certain threshold for the maximum and the minimum charge that the actuator can deliver has been considered in the simulations. If the net or the differential charges reach the saturation level, the actuator model automatically scales the other charge to maintain the alignment of the resultant force equal to the one that can be obtained without the saturation limit.

Due to the strong coupling already noticed and since both the net control charge and the differential control charge affect both the translational and the rotational dynamics together, we analyzed first the capability of achieving a desired position disregarding the attitude control; then the attitude control was added to explore the possibility of performing both the translation and the attitude control simultaneously.

This control strategy aims to verify the possibility of achieving a desired final position given an initial state vector by imposing a control action only on the translation of the spacecraft. The attitude dynamics is not directly controlled here, but it evolves under the electrostatic effects since the equations of motions are coupled. In particular, due to the electrostatic torque given by the total charge (term $\mathbf{T}_{eG}$) and due to the dipole moment effects, the spacecraft is expected to start spinning about the z-axis in the BF frame. A certain level of charge (Q_0) must be always maintained in order to guarantee the hovering condition, such that a certain level of torque is always acting on the spacecraft. Each change in the charges causes a torque acting on the spacecraft which cannot be balanced by any other torque (since the spacecraft is composed of a single dipole and does not have any momentum exchange device), and which induces a rotation of the spacecraft itself. The control of such a spacecraft is also made extremely difficult by the fact that the forces along the x- and y-axis in the RIC reference frame depend on the attitude of the dipole, making the control action and the translational motion itself strictly bounded to the attitude motion and constrained by that. The initial scenario of the simulation is given by the spacecraft hovering at an arbitrarily chosen initial position and attitude over the sunlit face of the main body, as reported in Table 2.9.

Since the spacecraft at the initial condition is hovering, the initial velocities are all equal to zero. The reference final position has been arbitrarily chosen as reported in Table 2.10.

The maximum charge level is set to be equal to $\pm 750\,\mu$C. All the considerations and issues related to charging a spacecraft to such a high level have not been taken into account in this analysis. The simulation time is set to 20 h (as done in Corradino

Table 2.9 Initial position and attitude in hovering

x [m]	y [m]	ψ [rad]
–25	2	1

Table 2.10 Reference position in hovering

x [m]	y [m]
–23	1

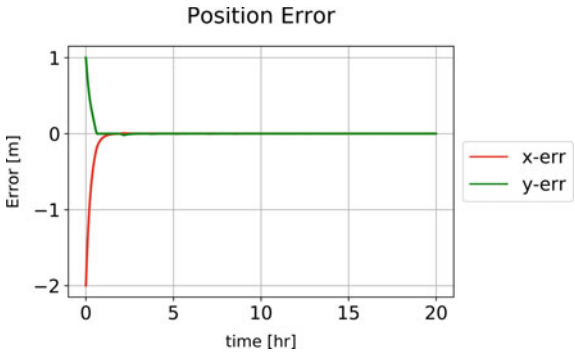

Fig. 2.60 Time evolution of the position errors for the hovering control without attitude control

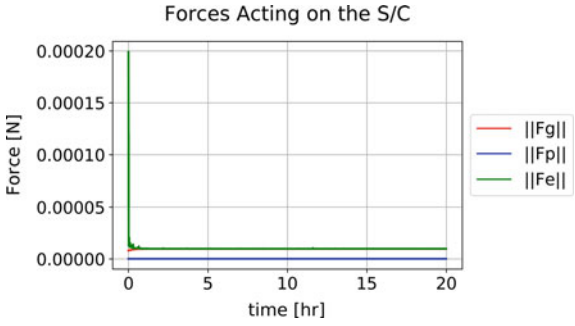

Fig. 2.61 Forces acting on the spacecraft for hovering control without attitude Control

2018). The results of the simulation are reported in Fig. 2.60 by the means of the error between the position at the current instant of time and the reference position (e.g., $e_x(t) = x(t) - x_{ref}$).

Both the position errors are dropped to zero in a short amount of time by using the ideal control law previously discussed. From Fig. 2.60, the possibility to maintain the hovering condition is evident even if the desired location is not a stable equilibrium point, as in the case here presented (see Sect. 2.13.2). The norm of the forces acting on the spacecraft is in Fig. 2.61.

As expected, the electrostatic force has a peak during the first instants of time due to the control action demanded by the PD controller. When the spacecraft reaches

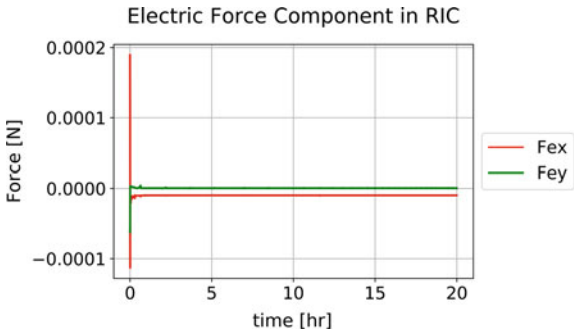

Fig. 2.62 Electrostatic force components for the hovering control without attitude Control

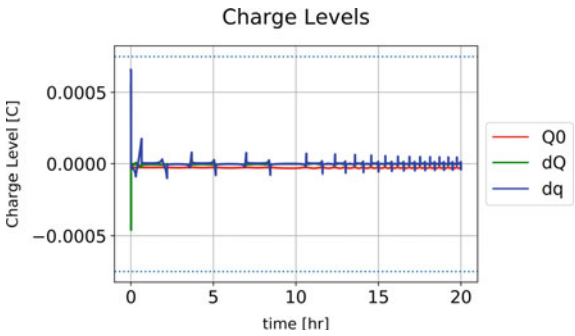

Fig. 2.63 Control charges for hovering control without attitude control

the desired final position, the electrostatic force is maintained almost constant in order to keep the position. The delivered electrostatic force is always higher than the gravitational force acting on the spacecraft, which is due to the fact that to maintain the hovering position, the electrostatic force must counter the summation of both the gravitational and the SRP forces. Hence, the hovering is confirmed to be an energetically inefficient strategy. The electrostatic force is expected to be delivered mostly along the x-direction in the RIC frame in order to maintain the hovering position. This is confirmed in Fig. 2.62.

The levels of charge (both net and differential) needed are reported in Fig. 2.63 together with the level of charge Q_0 that must be maintained to achieve the hovering at the reference position. Once the final position has been achieved, the net charge dQ required to maintain the final position is almost zero, while a continuous control on the differential charge is needed to avoid drifting of the spacecraft. In Fig. 2.63, the blue dotted lines show the saturation levels imposed for both the total and the differential charge.

To reduce the control effort and the pulsations in the differential charge, a dead band in which the spacecraft is free to drift should be considered. The dead band can be defined in terms of both x and y positions. If the spacecraft is inside this region, the only charge applied is Q_0, while if the spacecraft exits the predefined region, the

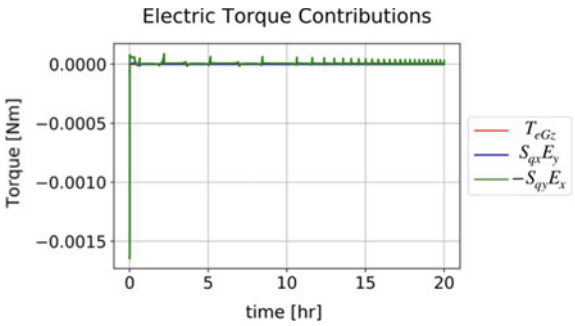

Fig. 2.64 Electrostatic torque for hovering control without attitude control

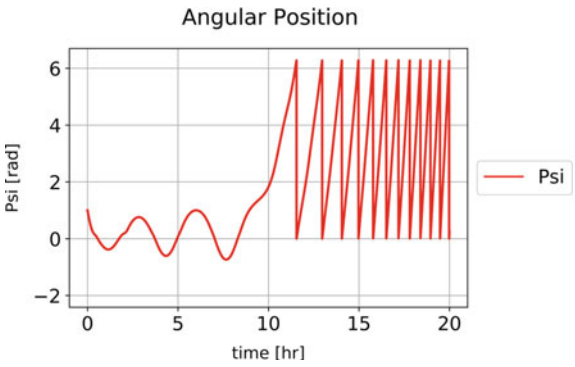

Fig. 2.65 Angular position of the spacecraft during hovering control without attitude Control

complete control law previously described is applied again. The differential control charge also generates a torque that affects the attitude motion of the spacecraft, modifying the spinning rate. The electrostatic torque contributions are reported in Fig. 2.64.

Figure 2.64 points out that the torques introduced during the position keeping are all positive, meaning that the spacecraft rotates in a counterclockwise direction in the RIC reference frame around the z-axis with an increasing spin rate. This result is confirmed by Fig. 2.65.

The highest contribution to the total electrostatic torque, in this case, is given by $-S_{q,y}E_x$ because the electric field is mostly directed along the x-direction in the RIC reference frame (see Fig. 2.66).

As expected, after an initial phase in which the spacecraft angular position oscillates under the torques given by the control charges required to translate the spacecraft itself from the initial position to the reference one, the angular position becomes positive during the position-keeping phase, and the spin rate increases. To limit the increment in the spin rate, the dead-band control law previously discussed can be used (Fig. 2.66).

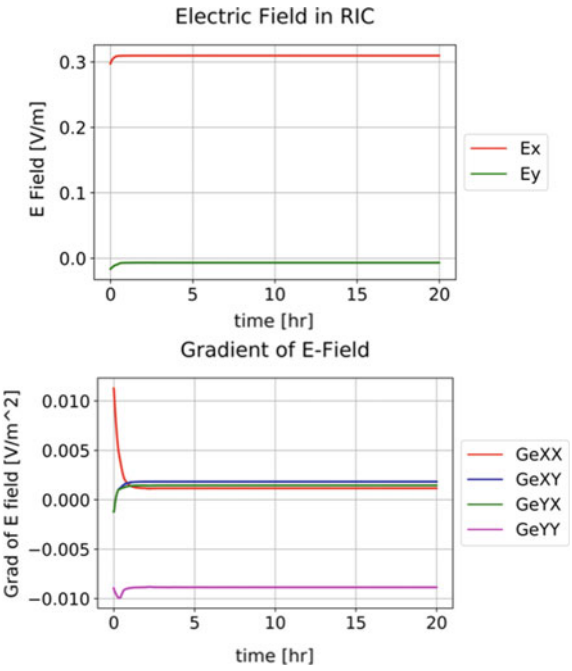

Fig. 2.66 Electrostatic field (upper) and gradient of the electrostatic field (lower) components in 2D in the RIC frame

2.14.4 Position and Attitude Control for Single-Dipole Spacecraft

Once the capabilities of achieving a desired position in hovering starting from an initial hovering condition with a single-dipole spacecraft have been explored, the possibility of achieving a desired final position with a desired final attitude starting from a given initial hovering condition is analyzed. The initial conditions are maintained equal to the ones reported in Table 2.9, while the final reference conditions are set as reported in Table 2.11.

The spacecraft has a line connecting the two masses perpendicular to the subsolar axis (the -x direction in the RIC reference frame) at the final desired attitude. The scenario described in this case is far more complex than the previous one because here a single electrostatic dipole that acts as an ideal actuator (that has coupled effects on the rotational and on the translational dynamics) should control a spacecraft with the rotational and the translational dynamics highly coupled. Furthermore, if the electric

Table 2.11 Reference position and attitude in hovering

x [m]	y [m]	ψ [rad]
–23	1	$-\pi/2$

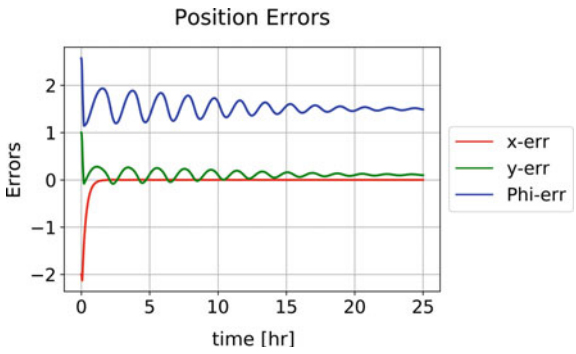

Fig. 2.67 Position and attitude errors for hovering and attitude control

dipole is aligned with the electric field described in each point by the PIC results, the torque component given by the first dipole moment is null, such that the modulation of the net charge gives the only control term on the attitude motion.

Figure 2.67 shows the results of the simulation which has been selected as the best one since it leads to a "stable" final configuration.

By considering the results in Fig. 2.66, we expected that the highest torque will be delivered by the term $-E_x S_{q,y}$. Moreover, the term $G_{e,yy}$, which is the highest in modulus, causes a strong coupling between the y-position and the attitude of the spacecraft (see also Eq. (2.124)), making the control extremely difficult. On the contrary, the x-position is not strongly affected by the attitude dynamics, since the predominant component of the control action is the net charge term. Figure 2.67 confirms this expectation. The reference x-position is achieved in a relatively low amount of time (about 2 h), while after 25 h of simulation, both the y-position and the angular position dynamics show low-amplitude and low-frequency oscillations around a reference error value which is different from zero. In particular, the residual error for the y-position is in the order of centimeters far from the reference value reported in Table 2.11, while the angular position error is of about 1.5 radians.

Hence, a PD controller can drive single-dipole spacecraft to a certain fixed final configuration, performing both the translational and the attitude control simultaneously. The main problem is that the PD controller is not capable of making the error equal to zero in steady-state conditions. This drawback is due to the proportional part of the PD controller; thus, a simple solution could be to augment the gain K_P associated with the proportional error, putting a bigger effort in the control action and making the steady-state error closer to zero or to substitute the PD controller with a proportional-integral-derivative (PID) one. The integrative part of this new controller will ensure the zeroing of the steady-state error.

The biggest issue for the case here analyzed is the coupling of the equations of motions and, as a consequence, also the ones of the actuator. In particular, the net charge is always different from zero, and it gives a constant torque which always acts on the attitude motion of the spacecraft. By changing the structure of the spacecraft, the torque term related to $T_{eG,z}$ can be canceled out for symmetry, making it possible to partially decouple the equation of motions and the equation of the ideal actuator

(indeed, the adoption of a new geometry can be seen as a change of the ideal actuator). The new geometry adopted and the new hovering control results are described in the following section.

2.14.5 *Ideal Hovering Control for a Double-Dipole Spacecraft*

The spacecraft with the new geometry adopted is composed by four spheres connected by two rigid tethers in a cross shape. The length of the tether is maintained equal to the one of the single-dipole spacecraft previously analyzed (10 m). The radius of each sphere is equal to $R_s = 0.046$ m such that each sphere of the new spacecraft has half cross-sectional area with respect to the single-dipole spacecraft. A mass equal to 0.665 Kg per sphere has been fixed to maintain the total mass of the spacecraft constant. Figure 2.68 shows the new geometry adopted and the reference frames used.

The total charge Q is now split in the four spheres, resulting in a net charge equal to $Q/4$ per each sphere. The differential charge associated with the spheres aligned with the x-axis in the BF reference frame is named q_1 (or first differential charge), while q_2 (or second differential charge) is the differential charge of the spheres on the y-axis in the BF frame. If the charges are assigned as in Fig. 2.68, the vector $\mathbf{S}_q$ in the RIC reference frame can be redefined as the summation of the effects given by the two dipoles formed by the masses along the x-axis and along the y-axis in the BF frame; thus, the matrix that links the vector $(dQ, S_{q,x}, S_{q,y})^T$ with the net and the differential charges can be rewritten as

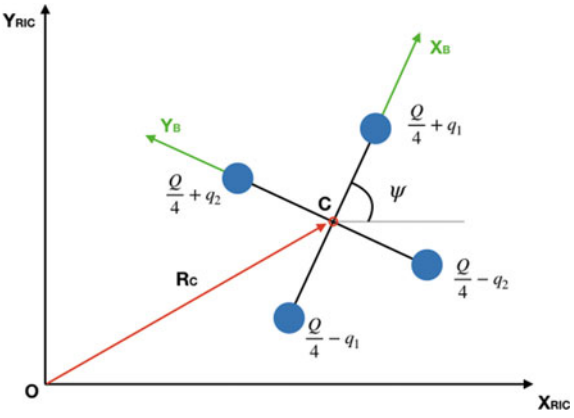

Fig. 2.68 Reference frame for the control analysis: four-sphere spacecraft

$$\begin{Bmatrix} dQ \\ S_{q,x} \\ S_{q,y} \end{Bmatrix} = \begin{bmatrix} 1 & 0 & 0 \\ 0 & +Lcos\psi & -Lsin\psi \\ 0 & +Lsin\psi & +Lcos\psi \end{bmatrix} \begin{Bmatrix} dQ \\ q_1 \\ q_2 \end{Bmatrix} \tag{2.127}$$

This new configuration is double symmetric with respect to the x-axis and the y-axis in the BF frame. Thus, the term given by the gravity gradient can be canceled out by the equation of motion for the rotation ψ. The symmetry of the spacecraft leads also to $I_{q,yy} = I_{q,xx}$; thus, $T_{eG,z} = G_{e,xy}(I_{q,yy} - I_{q,xx}) = 0$ in the Euler equation for the attitude motion. Thus, the equations of motion for the four-sphere spacecraft can be written as

$$\begin{aligned} {}^r\ddot{\mathbf{R}}_c &= -\frac{\mu}{R_c^3}{}^r\mathbf{R}_c + \frac{{}^r\mathbf{G}_g}{M} + \frac{{}^r\mathbf{f}_p}{M} + \frac{{}^r\mathbf{E}({}^r\mathbf{R}_c)}{M}Q + \frac{{}^r\mathbf{G}_e({}^r\mathbf{R}_c)}{M}{}^r\mathbf{S}_q \\ \ddot{\psi} &= \left({}^r\mathbf{S}_q \times {}^r\mathbf{E}({}^r\mathbf{R}_c)\right)\frac{1}{J_{zz}} \end{aligned} \tag{2.128}$$

In Eq. 2.128, the effects of the total charge are present only in the translational equations of motion. Moreover, in the ideal case here analyzed, the rotational motion is affected only by the electrostatic effects induced by the dipoles, which are directly delivered by the actuator. Thus, a finer control of the rotational motion can be achieved.

By following the very same procedure described for the case of a single-dipole spacecraft, the accelerations commanded by the controller can be linked to the vector $(dQ, S_{q,x}, S_{q,y})^T$ through the matrix $\mathbf{A}$, here redefined as

$$\begin{Bmatrix} \Delta\ddot{x}_c \\ \Delta\ddot{y}_c \\ \Delta\ddot{\psi} \end{Bmatrix} = \begin{bmatrix} \frac{{}^rE_x}{M} & \frac{{}^rG_{e,xx}}{M} & \frac{{}^rG_{e,xy}}{M} \\ \frac{{}^rE_y}{M} & \frac{{}^rG_{e,yx}}{M} & \frac{{}^rG_{e,yy}}{M} \\ 0 & \frac{{}^rE_y}{J_{zz}} & -\frac{{}^rE_x}{J_{zz}} \end{bmatrix} \begin{Bmatrix} dQ \\ S_{qx} \\ S_{qy} \end{Bmatrix} = \mathbf{A} \begin{Bmatrix} dQ \\ S_{qx} \\ S_{qy} \end{Bmatrix} \tag{2.129}$$

The problem of the loss of controllability due to the alignment of the electric dipole with the electrostatic field is no more an issue since even if one of the dipoles is aligned with the electric field lines, the other dipole is still capable of delivering a certain level of torque due to the perpendicularity of the two dipoles. Due to the partial decoupling of the equations of motions and of the actuator achieved with the geometry here presented, the coupled orbital and attitude control of the E-Glider can be achieved more easily with respect to the single-dipole case.

2.14.6 Position and Attitude Control for a Double-Dipole Spacecraft

Here, the results for the coupled control of both attitude and orbital motion to achieve a desired hovering condition with a desired angle of the x-axis in the BF reference

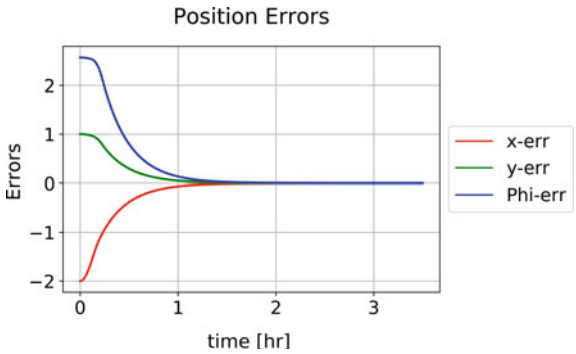

Fig. 2.69 Position and attitude errors: double dipole

frame with respect to the x-axis in the RIC reference frame are discussed. The parameters used are the same presented for the single-dipole case (see Tables 2.9 and 2.11). The saturation level for this simulation is set equal to $\pm 750\,\mu$C for both the net and the differential control charges. In this case, the control law adopted is capable of driving to zero the errors both in the translational motion and in the attitude motion without any overshoot and in a relatively low amount of time, as Fig. 2.69 points out.

The higher level of decoupling of the equations reached by adding the second dipole makes possible finer control of both the attitude and the orbital motion in the ideal case. By comparing the error rejection here presented with the results obtained for the coupled control in the single-dipole case, the improvement offered by adopting the second dipole is clear, as all the errors are driven to zero almost simultaneously without any oscillations or coupling both in the y error and in the angular error.

In the upper part of Fig. 2.70, the electrostatic force components $F_{e,x}$ and $F_{e,y}$ are reported, while in the lower portion, there are the two terms $S_{q,x}E_y$ and $-S_{q,y}E_x$, the sum of which gives the electrostatic torque on the spacecraft. The biggest effort is related to the x-component of the electrostatic force also in this case. Regarding the electrostatic torque terms, after an initial phase of almost constant low torque (in which the control action is mostly devoted to reducing the error in the x-position), there is a strong peak due to an abrupt variation of the component $-S_{q,y}E_x$. After this strong peak, both the terms of the electrostatic torque have a positive value which gradually decreases to almost zero once the ψ error becomes null.

In the upper portion of Fig. 2.71, the commanded charge levels to obtain the previously discussed electrostatic forces and torques are reported, while in the lower part, the actuator electrostatic effects are presented. The control charges needed are well under the saturation limit imposed, also during the initial transient phase in which the charges reach the highest level due to a strongest control action needed. The strong variations and the changes in the polarity of both q_1 and q_2 during the initial phases determine the previously noticed peaks in the electrostatic force and torque. In particular, by considering the initial attitude of the spacecraft, even if the magnitudes of the differential charges are comparable, values of $S_{q,x}$ notably higher than those of $S_{q,y}$ are expected during the initial phase. This is confirmed by the plot

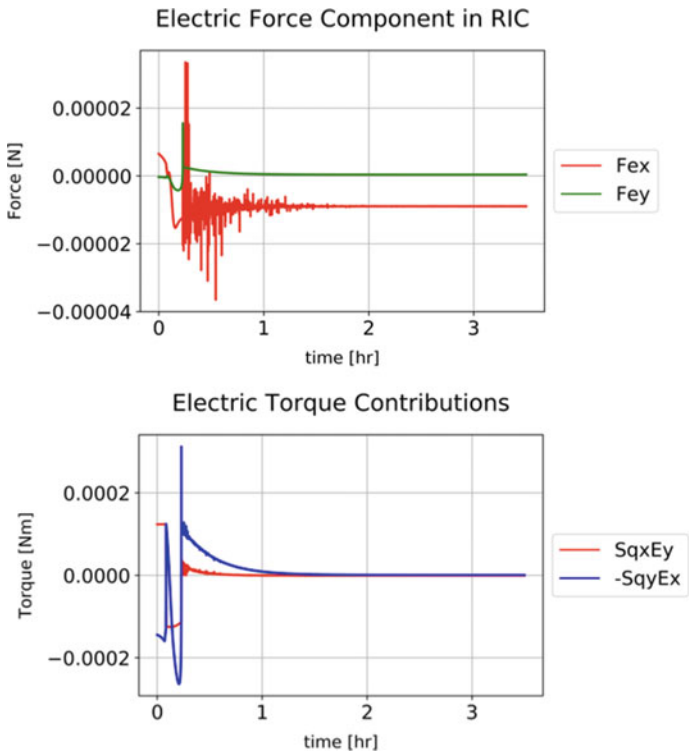

Fig. 2.70 Electrostatic force (upper) and torque (lower) components: double dipole

of the actuator electrostatic effects. The high value of $S_{q,x}$ in this phase, coupled with the also relatively high levels of the net control charge dQ, gives the peaks previously noticed in the $F_{e,x}$ components. The strong peak in the electrostatic torque is given by the $S_{q,y}$ component of the first momentum dipole even if $S_{q,x}$ is higher, due to the components of the electric field in the region considered. During the final phase in which the main objective is to maintain the hovering condition previously achieved, the charge levels are very low such that the resulting $S_{q,x}$ component is positive and slightly higher in modulus than $S_{q,y}$ to ensure the zero torque condition (given by $S_{q,x}E_y - S_{q,y}E_x = 0$) once the system reaches steady-state conditions. Since the component E_x of the electric field is always positive and greater than E_y (which is also negative) in the region of interest, the general rule $|S_{q,x}| > |S_{q,y}|$ can be derived for the case here analyzed. Moreover, S_{qx} and S_{qy} must have opposite signs in order to balance the torque contribution.

As said, the saturation level of $\pm 750\,\mu$C was arbitrarily imposed on the actuator, and it could be reduced to a more realistic value. A high limit of saturation for the levels of charge implies a wider range of feasibility for the maneuvers tested, and it makes it possible to increase the proportional gains K_P of the PD controller here adopted, reducing the error at steady state. This means that the proper definition

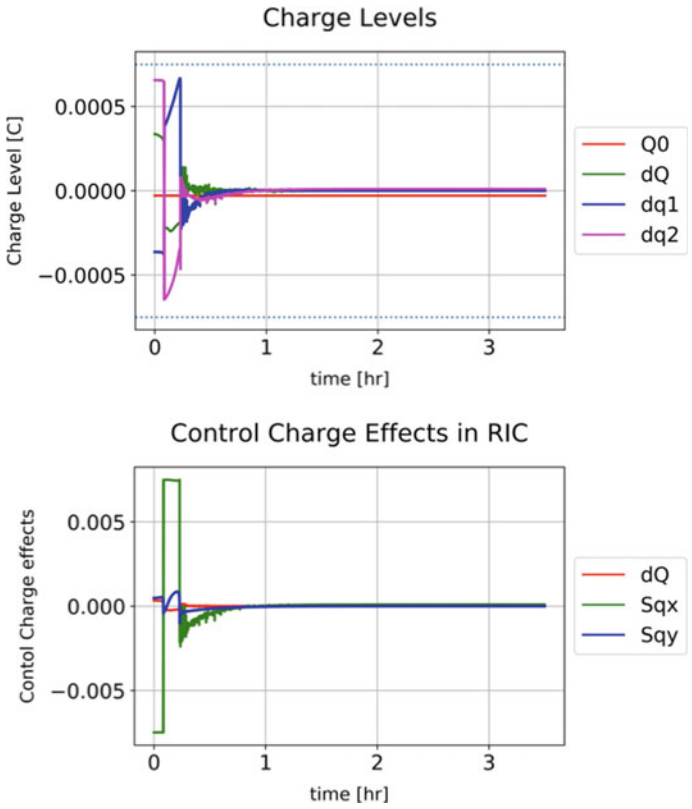

Fig. 2.71 Control charges (upper) and actuator electrostatic effects (lower): double dipole

of a saturation level affects the choice of the controller and the error in steady-state condition for a PD controller. The selection of a saturation charge below the predicted levels of Q/M defined in Sect. 2.13.2 is not possible; otherwise, the actuator will saturate before reaching the charge level needed to levitate over the asteroid surface, making the hovering not feasible. By considering Fig. 2.45, we can conclude that by reducing the saturation level, a sort of "no-fly" zone is created starting from the asteroid surface (the height of this zone increases as the saturation level decreases). This zone must be avoided to prevent the spacecraft from irreversibly collapsing on the asteroid.

2.14.7 Tether Length Sensitivity

In this section, an analysis of the effects of the length of the tether that links the four masses of the spacecraft is presented. The length of the tether can be seen as

Table 2.12 Tether length values for simulations

Value 1 [m]	Value 2 [m]	Value 3 [m]	Value 4 [m]	Value 5 [m]
0.25	1.00	2.00	5.00	10.00

a parameter of the actuator since it affects the outputs $S_{q,x}$ and $S_{q,y}$ delivered by the actuator in the RIC reference frame once the net control charge dQ and the differential charge q_1 and q_2 are given as input. During this analysis, five different spacecraft are considered. All of them are equal, except for the length of the tethers. The tether lengths used for these simulations are reported in Table 2.12.

As for the previous analysis, the tether length is considered as the separation distance between the center of mass of two spheres with opposite position with respect to the center of mass of the spacecraft. Since the charge for this analysis is assumed to be concentrated in the center of mass of each sphere, the length of the tether is the separation distance between the two charges that constitutes one of the two dipoles of the spacecraft. It is assumed that the two tethers of a single spacecraft are equal in length in order to maintain the symmetry of both the masses and the charges, making it possible to use the very same control law developed for the four-sphere spacecraft. The parameters used here are the very same as in previous simulations. The proportional and derivative gains K_p and K_d of the PD controllers have been kept constant and equal to the ones selected for the simulation discussed previously. Also, the initial and final conditions are kept constant with respect to the previous analysis in order to detect only the variations due to the different lengths of the tether selected. The saturation level is $\pm 750\,\mu\text{C}$, which is high enough to ensure the convergence of all the error dynamics to about zero for all the cases here analyzed. Figure 2.72 presents the results obtained from the simulations of the cases reported in Table 2.12.

Only the level of charges and the rejection of the errors for each case are reported in the figure since it is possible to identify the effects given by changing the tether length by analysis of these two plots. Generally speaking, it is possible to identify two regions in both the plot of the charge level and the plot of the errors. The first region is referred to the transient phase and the second one to the hovering conditions maintained. The transient phase in the plot of the charge level is characterized by the abrupt variation of the differential charges and the high level of the net charge dQ. In the plots of the errors, the transient phase is identified as the region in which the errors move from the initial value to a band close to the condition of zero error and do not escape from this region. It is immediately clear that the length of the tether affects the duration of the transient phases. By increasing the length of the tether, the time duration of the transient phase is reduced. The reduction is more evident in the plot of the charges. It is better to remark that the levels of charge are influenced by the error through the accelerations imposed by the PD controllers and that the errors are affected by the charges since they define the level of force and torque applied to the system in a closed-loop system; thus, a reduction in the transient phase of the

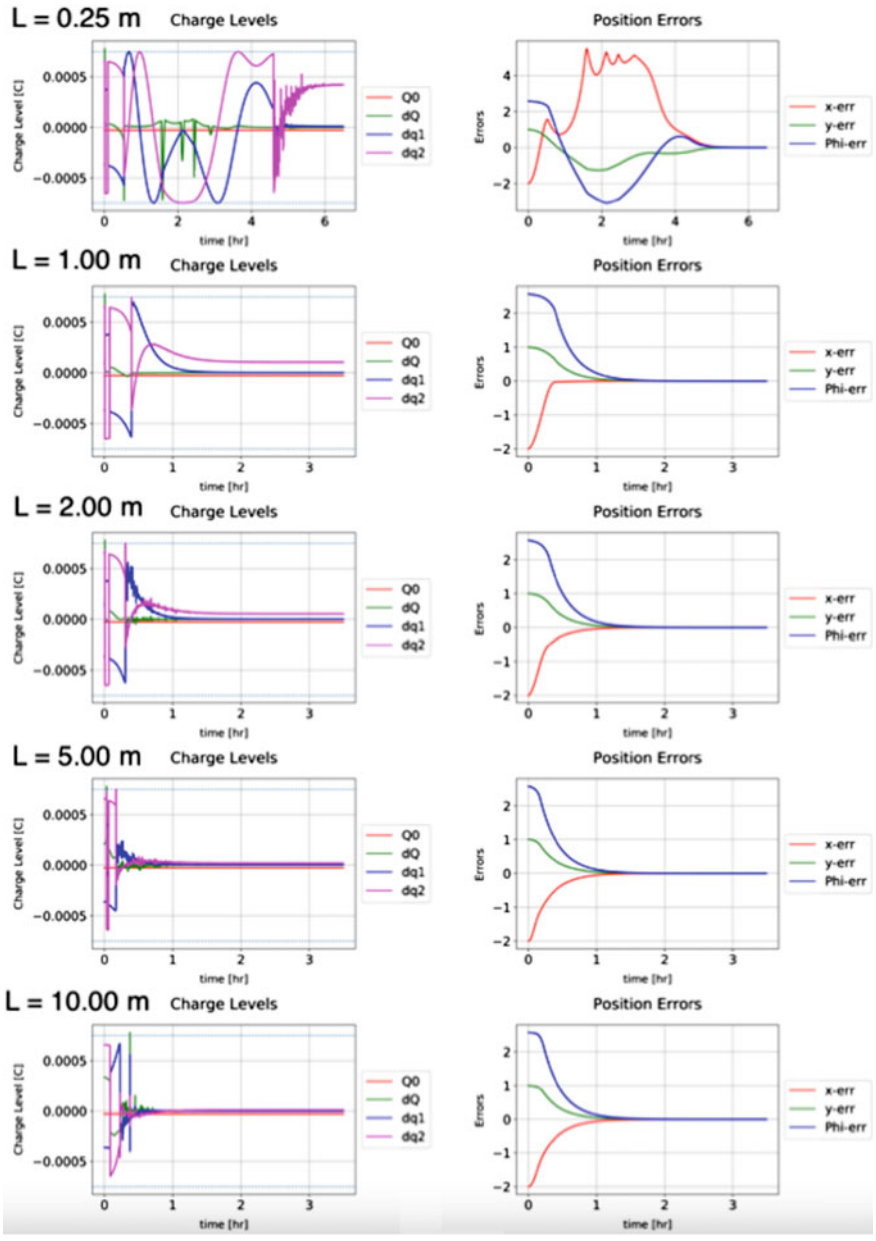

Fig. 2.72 Control charges (left) and error dynamics (right) for different tether lengths

charges implies a reduction in the transient phase of the errors. The reduction of the transient phase of the errors is evident by doing a comparison between the case of

tether length equal to 0.25 m and the one which measures 1 m. In the former case, the error is driven to zero in almost 6 h, while in the latter case, it takes only about 2 h. By doing the same comparison for the other case, it can be seen that the settling time (defined as the time at which the errors enter in the band close to zero and do not exit again) is reduced by just a few minutes. On the contrary, on the plot of the charges, it is evident that the initial transient phase is strongly reduced. The transient phase of the charges can be divided into two sub-phases; in the first one, the control charges are varying in a continuous way, and in the second one, they behave in an impulsive way. The increment of the length of the tether mostly reduces the time of the first phase, while the second one is not largely affected by the length of the tether. It can be noticed that the amplitude of the impulses in the control charges highlighted by the simulations during the second phase of the transient is extremely reduced if the tether is 1 m long. Moreover, during the transient phase in all the cases, except the last one reported, the charges reach the saturation level. Now the second part of the plots, the hovering conditions maintained, is taken into account. The increment of the tether length affects the level of the differential charges q_1 and q_2 needed to maintain the position achieved and to obtain the condition of zero torque previously identified as necessary to maintain the desired attitude. In particular, the reduction of the level of q_2 is evident. This is due to the fact that the level of q_2 at $\psi = -\pi/2$ affects only $S_{q,x}$, while q_1 affects only $S_{q,y}$. From this, and by recalling that the electric field in the region swept by the spacecraft during this maneuver has a positive component along the x-axis and a negative one along the y-axis lower in modulus than the positive one and also that the electrostatic torque can be computed as $T_e = S_{q,x} E_y - S_{q,y} E_x$, the reason for which a value for q_2 always notably higher than q_1 is obtained, it is rather clear. In general, it can be concluded that a higher tether length implies a lower level of charge needed to accomplish the same maneuver in a lower amount of time. For the cases analyzed here, it is also evident that for a tether length equal to 0.25 m, achievement of the previously defined hovering condition is extremely difficult, and the feasibility of the maneuver cannot be ensured since there is a phase during the transient in which the center of mass of the spacecraft is extremely close to the asteroid surface, reaching a minimum distance from the center of the asteroid of about 18 m; thus, it should be verified that the attitude conditions during this phase are such that the electrodes do not impact the surface of the asteroid. It can be noticed that the four peaks of maximum error in the x-position of the spacecraft with a tether of 0.25 m correspond to the peaks in the net charge $Q = dQ + Q_0$ equal to the saturation level. This analysis highlights the fact that adopting a short separation of the charges can make the mission unfeasible from the energetic point of view. This is due to the fact that the level of charge needed by each electrode affects the total power level required onboard; in particular, a higher charge means a higher electric potential (in modulus) of the spacecraft and thus a higher power needed to maintain the level of charge.

2.15 Including the Effect of Charging Electrodes

2.15.1 Spacecraft Charging

The power supply voltage for charging a spacecraft, which is regarded as the electrostatic potential of the spacecraft relative to the ambient plasma potential, is given by the equation below.

$$V_{sc} = \frac{Q}{C} \tag{2.130}$$

A spacecraft in the plasma environment around an asteroid collects charged particles. Besides, the spacecraft itself is also exposed to the solar radiation and emits photoelectrons. As a result, the charge of the spacecraft varies due to the current flux from/to the ambient plasma, as expressed by the equation below (Nitter et al. 1998; King et al. 2002).

$$\frac{dQ}{dt} = I_i - I_e - I_p + I_{p,sc} \tag{2.131}$$

where I_i, I_e, and I_p are the currents from the solar wind ions, the solar wind electrons, and the photoelectrons emitted from the asteroid surface, respectively; and $I_{p,sc}$ is the photoelectron current from the spacecraft. These currents can be expressed as follows (Nitter et al. 1998; Havnes et al. 1987; Hirata and Miyamoto 2012):

$$\begin{aligned}
I_i &= \begin{cases} N_{sp} \cdot \pi r_{sp}^2 e n_i v_i \left(1 - \dfrac{2eV_{sc}}{m_i v_i^2}\right) & \left(V_{sc} < \dfrac{m_i v_i^2}{2e}\right) \\ 0 & \left(V_{sc} \geq \dfrac{m_i v_i^2}{2e}\right) \end{cases} \\
I_e &= \begin{cases} N_{sp} \cdot \pi r_{sp}^2 e n_e \sqrt{\dfrac{8k_B T_e}{\pi m_e}} \exp\left(\dfrac{eV_{sc}}{k_B T_e}\right) & (V_{sc} < 0) \\ N_{sp} \cdot \pi r_{sp}^2 e n_e \sqrt{\dfrac{8k_B T_e}{\pi m_e}} \left(1 + \dfrac{eV_{sc}}{k_B T_e}\right) & (V_{sc} \geq 0) \end{cases} \\
I_p &= \begin{cases} N_{sp} \cdot \pi r_{sp}^2 e n_p \sqrt{\dfrac{8k_B T_p}{\pi m_e}} \exp\left(\dfrac{eV_{sc}}{k_B T_p}\right) & (V_{sc} < 0) \\ N_{sp} \cdot \pi r_{sp}^2 e n_p \sqrt{\dfrac{8k_B T_p}{\pi m_e}} \left(1 + \dfrac{eV_{sc}}{k_B T_p}\right) & (V_{sc} \geq 0) \end{cases} \\
I_{p,sc} &= \begin{cases} N_{sp}^* \cdot \pi r_{sp}^2 \dfrac{\varepsilon_{sc} J_0}{d^2} & (V_{sc} < 0) \\ N_{sp}^* \cdot \pi r_{sp}^2 \dfrac{\varepsilon_{sc} J_0}{d^2} \exp\left(-\dfrac{eV_{sc}}{k_B T_p}\right) & (V_{sc} \geq 0) \end{cases}
\end{aligned} \tag{2.132}$$

where k_B is the Boltzmann constant; $v_i \equiv (v_D^2 - 2e\phi/m_i)^{1/2}$ is the velocity of the solar wind ions; T_e and T_p are the temperatures of the solar wind electrons and photoelectrons, respectively; m_i and m_e are the masses of an ion and an electron,

respectively; ε_{sc} is the photoemissivity of a spacecraft; $J_0 \equiv 4.5 \times 10^{-6}\ \mathrm{A/m^2}$ is the photoemission current density at 1 AU (Nitter et al. 1998); and d is the distance of an asteroid from the Sun expressed in AU. These equations indicate that a positively charged spacecraft attracts more electrons, while a negatively charged spacecraft attracts more ions. The last equation shows that the photoelectric effect is less likely to occur for a positively charged spacecraft. Note that Eq. (2.132) is derived based on the assumption that $v_{T,i} \ll v_D \ll v_{T,e}$.

Since the charge of the spacecraft is affected by the ambient plasma, the spacecraft must emit current constantly in order to maintain the charge level (King et al. 2002). The emitted current I_{sc} is given by the following equation:

$$\begin{aligned} \frac{dQ}{dt} &= I_i - I_e - I_p + I_{p,sc} - I_{sc} = 0 \\ \therefore I_{sc} &= I_i - I_e - I_p + I_{p,sc} \end{aligned} \tag{2.133}$$

Although possible methods for emitting current from a spacecraft are not discussed in this paper, several solutions have been proposed in previous research (Quadrelli et al. 2017a; Schaub et al. 2004; King et al. 2002). Consequently, the required power for electrostatic levitation with a constant charge Q is calculated from Eqs. (2.130)–(2.133) as follows:

$$P = |V_{sc} I_{sc}| \tag{2.134}$$

The flow chart to calculate the required power is described in Fig. 2.73.

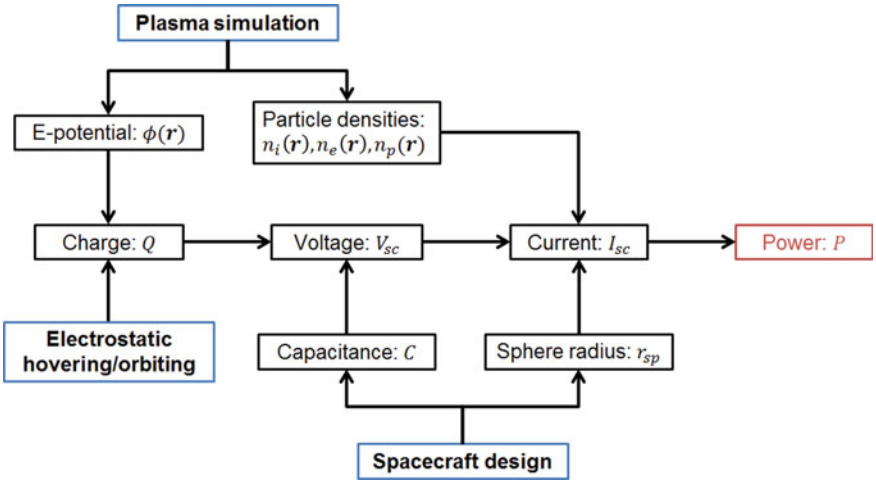

Fig. 2.73 Flow chart of power calculation

2.15.2 Power Required for Electrostatic Hovering

Electrostatic hovering above an asteroid can potentially be achieved by creating artificial equilibrium points with electrostatic force. This section investigates the feasibility of electrostatic hovering from the perspective of power requirement. Analyses are performed for the collinear equilibrium point solutions obtained in the previous subsection.

Figure 2.74a shows the magnitude of voltage required for electrostatic hovering at the corresponding altitude. The power supply voltage is calculated from the required charge based on Eq. (2.130). This result indicates that dayside hovering requires at least 100 kV levels of charge. Although such high-voltage charging itself might not cause any risk to a spacecraft, it can cause electrostatic discharge, which is harmful to spacecraft subsystems. Therefore, the spacecraft must be designed to prevent electrostatic discharge itself or instrument damage due to it, as discussed in previous research (Schaub et al. 2004; King et al. 2002).

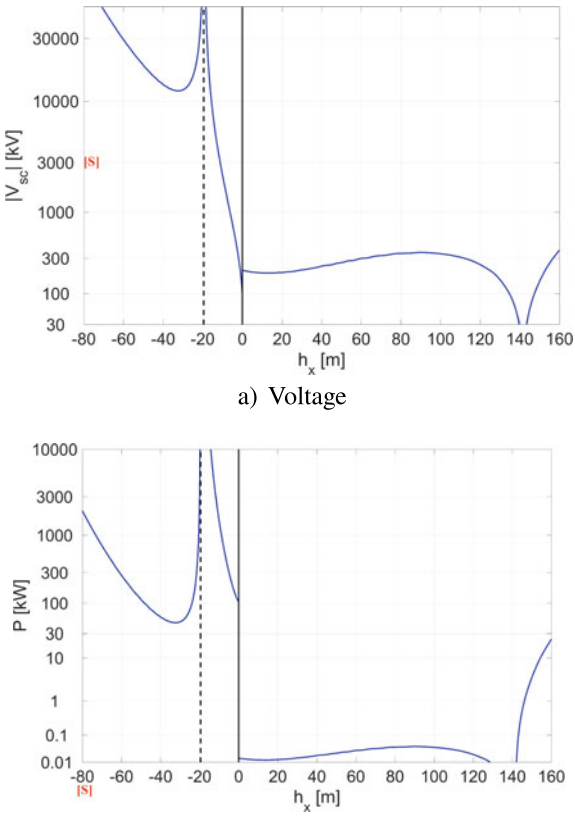

Fig. 2.74 Required voltage/power for electrostatic hovering at a collinear equilibrium point

Figure 2.74b illustrates the power required to hover the spacecraft at an equilibrium point. It is indicated that hovering on the dayside near the surface requires the power of as much as 100 kW, while hovering on the nightside requires only about 15 W, despite almost the same charge levels. This difference primarily stems from two reasons. First, the mass of an electron is much smaller than that of an ion, and thus, electrons are much more mobile in a plasma. This results in a large negative current flux, requiring much power to maintain a positive charge. Second, a dense photoelectron layer near the surface is present around the subsolar region, as shown in Fig. 2.11. This environment also involves a large negative current for a positively charged spacecraft. These results imply that electrostatic hovering with a negative charge is more feasible than that with a positive charge from the perspective of power requirement.

2.15.3 *Power Required for Electrostatic Orbiting*

The power requirement for electrostatic orbiting is analyzed in this subsection. Figure 2.75 shows the power history of the orbit provided in Fig. 2.21a during one orbital period. Even though the charge Q is given as a constant, the required power varies because the current flux from an ambient plasma depends on the position of a spacecraft with respect to an asteroid. The broken line in the figure represents the average power defined by the following equation:

$$P_{ave} = \frac{1}{T}\int_0^T P(t)dt \tag{2.135}$$

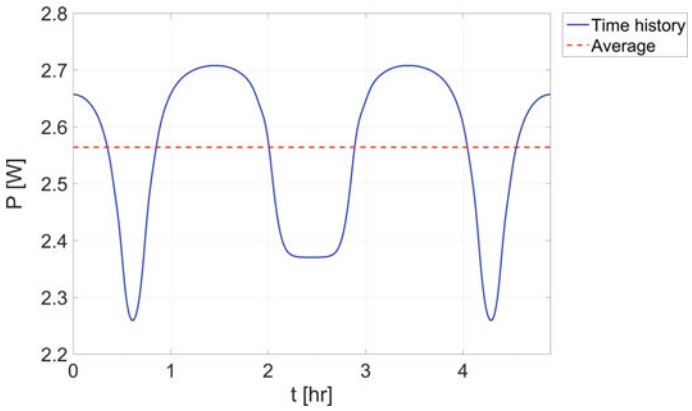

Fig. 2.75 Power consumption during one orbital period

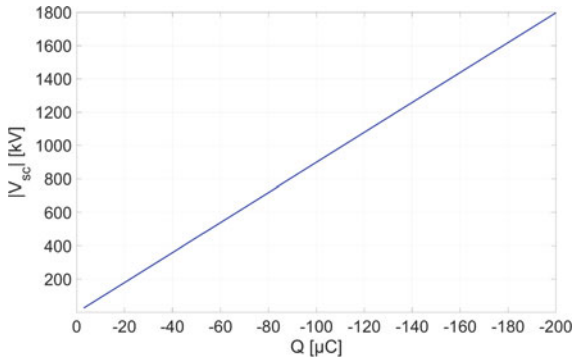

a) Voltage

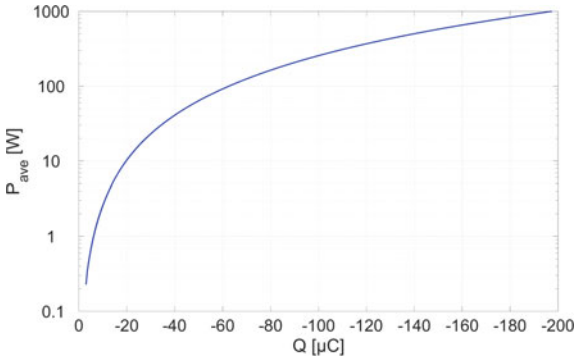

b) Power

Fig. 2.76 Required voltage/power for electrostatic orbiting

The average power required for this electrostatic periodic orbit is calculated as 2.56 W, and it appears to be feasible for missions.

Figure 2.76 shows the voltage and power required to achieve electrostatic periodic orbit solutions provided in Fig. 2.23. Figure 2.76a is simply obtained from the relationship between the charge and the voltage, and Fig. 2.76b plots the average power of each single periodic orbit. Interestingly, even though the solution space structure of electrostatic periodic orbits is complex and involves bifurcation, the power diagram exhibits a simple profile as shown in Fig. 2.76b. According to this analysis, example values of the required voltage and power are $|V_{sc}| = 89.9\,\mathrm{kV}$ and $P_{ave} = 2.56\,\mathrm{W}$ for the orbit with $Q = -10\,\mu\mathrm{C}$; and $|V_{sc}| = 449\,\mathrm{kV}$ and $P_{ave} = 63.8\,\mathrm{W}$ for the orbit with $Q = -50\,\mu\mathrm{C}$.

Comparing Figs. 2.74b and 2.76b, electrostatic orbiting requires considerably lower energy than electrostatic hovering on the dayside. Although an E-Glider must be inserted into an orbit either by itself or a mother spacecraft, after the insertion, it can orbit around an asteroid without requiring any fuel. The required voltage and power largely depend on the design of an E-Glider, and thus, further investigations must be carried out to optimize the entire system design of the E-Glider. In addition,

as mentioned in Sect. 2.15.3, the spacecraft must be designed to have the capability of handling high voltage.

2.15.4 Current Collection for Spherical Electrodes

As already indicated above, the electrodes are assumed to be totally insulated from the spacecraft structure and also from the other electrodes such that the mutual capacitance is equal to zero. This gives a diagonal capacitance matrix for the overall spacecraft given only by the self-capacitance of each electrode.

To correctly evaluate the total power needed to maintain a certain level of charge, computation of the current collected by each electrode of the spacecraft is required. The current collection in a plasma can be analyzed by considering two different regimes: the sheath-area-limited (SAL) regime and the orbit-motion-limited (OML) regime (Bhattarai and Mishra 2017).

The SAL regime can be adopted when the radius of the electrode R_{el} is comparable or higher than the sheath dimension given by the local value of the Debye length λ_D. Hence, if $R_{el}/\lambda_D \geq 1$, the thin-sheath approximation of the SAL model can be used. In the SAL regime, all the particles that enter the Debye sheath are assumed to be captured by the electrode; thus, the current density is mostly limited to the thermal current on the spacecraft surface (Mott-Smith and Langmuir 1926).

Instead, the OML regime can be assumed when the radius of the electrode is lower than the sheath dimension, such that $R_{el}/\lambda_D \ll 1$. In this case, under the assumption of the OML regime, only a small percentage of the particles that enter the Debye sheath are captured by the electrode (only the particles with a trajectory that approaches the electrode with a minimum distance below a certain threshold), while most of the particles are deflected following a curved trajectory that does not bring them close enough to the electrode to be captured. Thus, in the OML regime, it can be assumed that the current collected is mainly limited by the electrode dimension.

First, the current collected by a spherical electrode in a plasma environment as the one described by the PIC analysis is evaluated. The density of each species at each position is known from the outputs of the PIC analysis. By knowing these densities and the temperature of each species, the total Debye length can be computed at each position as

$$\lambda_D(\mathbf{R}) = \sqrt{\frac{\varepsilon_0 k_B/e^2}{\frac{N_p(\mathbf{R})}{T_p} + \frac{N_e(\mathbf{R})}{T_e} + \frac{N_i(\mathbf{R})}{T_i}}} \tag{2.136}$$

where $\mathbf{R}$ is the position vector in the RIC reference frame, ε_0 is the vacuum permittivity, k_B is the Boltzmann constant, e is the elementary charge, $N_j(\mathbf{R})$ is the density of the species j function of the position of evaluation, and T_j is the temperature of the species j. By assuming a plasma field as the one previously described, the total Debye length can be evaluated by using the PIC results as explained. In Fig. 2.77,

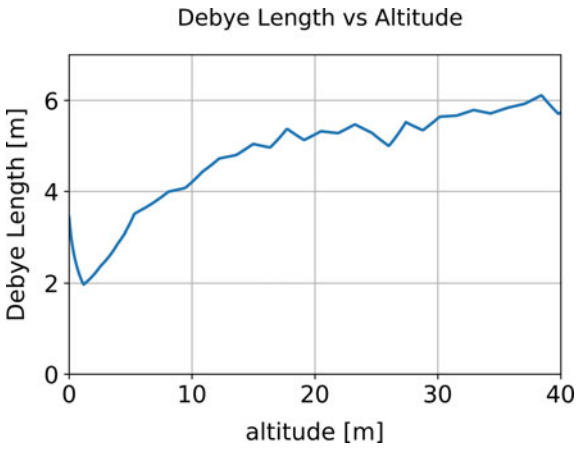

Fig. 2.77 Total Debye length as a function of the altitude

the Debye length as a function of the altitude on the subsolar axis (x-axis in the RIC frame) is reported.

The total Debye length is almost always higher than 2 m. Thus, for the case of a spherical electrode with radius $R_s = 0.046$ m, the OML regime is the most suitable. Under this assumption, the collected ion current I_i for each spherical electrode can be computed as (Quadrelli et al. 2017b; Nitter et al. 1998)

$$\begin{aligned} I_i &= \frac{1}{4} A_{sph} e N_i v_i \left(1 - \frac{2eV_{el}}{m_i v_i^2}\right) \quad \text{if} \quad V_{el} < \frac{m_i v_i^2}{2e} \\ I_i &= 0 \qquad\qquad\qquad\qquad\quad \text{if} \quad V_{el} > \frac{m_i v_i^2}{2e} \end{aligned} \tag{2.137}$$

where A_{sph} is the external surface of the sphere considered as an electrode, e is the elementary charge, $v_i = (v_D^2 - 2e\phi/m_i)^{0.5}$ is the solar wind ion velocity computed by knowing the potential ϕ of the plasma and the drift velocity, V_{el} is the bias electrostatic potential of the spherical electrode, and m_i is the proton mass.

If the electrode has a negative potential ($V_{el} < 0$), the collected electron and photoelectron currents are computed as (Bhattarai and Mishra 2017)

$$\begin{aligned} I_e &= \frac{1}{4} A_{sph} e N_e \sqrt{\frac{8k_B T_e}{\pi m_e}} exp\left(\frac{eV_{el}}{k_B T_e}\right) \\ I_p &= \frac{1}{4} A_{sph} e N_p \sqrt{\frac{8k_B T_p}{\pi m_e}} exp\left(\frac{eV_{el}}{k_B T_p}\right) \end{aligned} \tag{2.138}$$

Both the electron and the photoelectron can be expressed by using the very same formulation. Note that in Eq. 2.138, the electrode potential V_{el} is negative; hence, the entire exponential term is negative, leading to an exponential decrement of the

collected current if the potential is decreased. This can be expected since the more negative the potential, the better the approximation of an ion-saturated sheath (Bhattarai and Mishra 2017).

If the electrode has a positive potential ($V_{el} > 0$), the electron and photoelectron current collection is enhanced and can be computed as (Laframboise and Parker 1973)

$$\begin{aligned} I_e &= \frac{1}{4} A_{sph} e N_e \sqrt{\frac{8 k_B T_e}{\pi m_e}} \left(1 + \frac{e V_{el}}{k_B T_e}\right) \\ I_p &= \frac{1}{4} A_{sph} e N_p \sqrt{\frac{8 k_B T_p}{\pi m_e}} \left(1 + \frac{e V_{el}}{k_B T_p}\right) \end{aligned} \tag{2.139}$$

By using these equations, the power needed by the spacecraft here considered can be evaluated to assess the feasibility of hovering from the energetic point of view. The total power needed is computed by evaluating both the potential V_{el} and the current collected I_{el} by each electrode of the spacecraft. Once that these values are available, the total power needed is computed as the sum of the power required by each electrode at each instant of time. Knowledge of the exact position in the RIC frame of each electrode leads to a more accurate evaluation of the collected current since the exact density of each species on that location is known from the PIC results. The scenario used for the simulation here presented is exactly the one previously analyzed in Sect. 2.14.6; thus, the length of the rigid tethers is 10 m. The results in terms of potential for each electrode (upper plot) and total power needed onboard (lower plot) for the repositioning and pointing maneuver analyzed in depth in Sect. 2.14.5 are shown in Fig. 2.78.

Note that the legend of this figure says which color is associated with the electrode located on a certain semi-axis in the BF reference frame. The symmetry of the potential of the electrodes located on two opposite sides with respect to the center of mass of the spacecraft is given by the fact that they are all equal from the geometric point of view and because the two electrodes that form a dipole have the same level of net charge Q and opposite differential charge dq. The potential bias of the electrodes is extremely high, reaching values even higher than 10000 KV in modulus during the initial transient phase. During the final position-keeping phase, the potentials drop to lower values in modulus, being about -1400 kW for the electrodes along the x-axis in BF and 600 KV and about -3400 KV for the electrodes on the +y and -y semi-axes, respectively. These levels are clearly unfeasible, especially for a small CubeSat like the one simulated here. Such a high potential is given by an extremely low capacitance due to the extremely reduced size of the spheres. By increasing the size of the spheres, the enhancement of the self-capacitance could be possible, but the hypothesis of the OML theory could be not valid for the needed increment in the size of the sphere; moreover, a higher surface area implies a higher current collection that can affect the total power needed. The total power required during the initial transient phase shows peaks of about 800 W, while during the final position-keeping phase, the power required is about 75 W. These values are extremely high for the

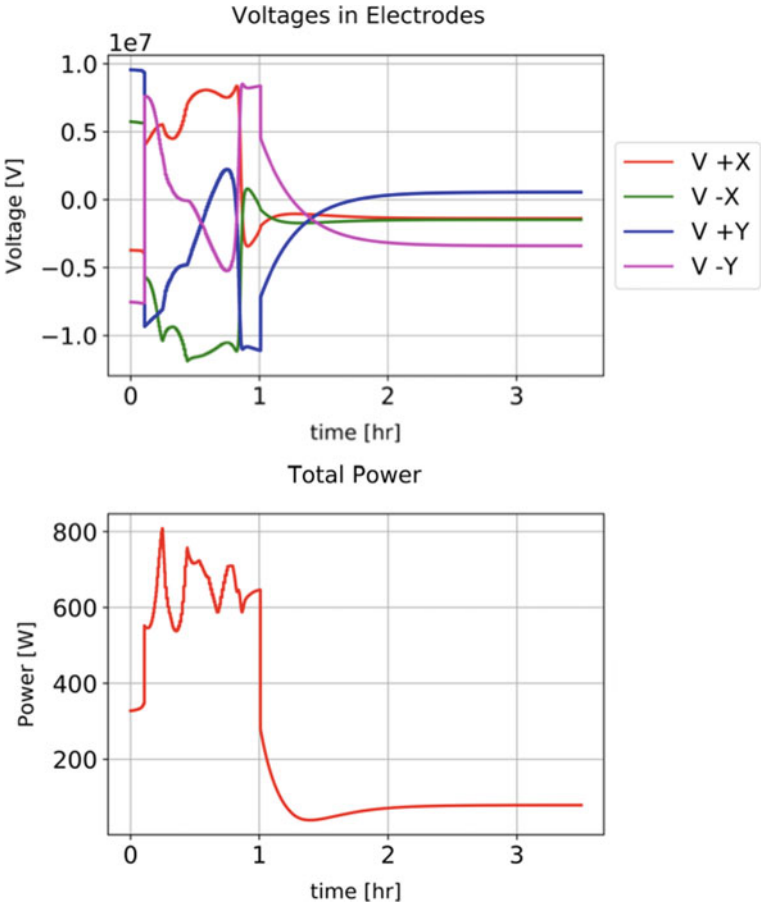

Fig. 2.78 Electrode potentials (upper) and total power needed (lower) for a four-sphere spacecraft model

state-of-the-art technologies available for the power production in a small CubeSat (NASA 2020). By considering both the total power level and the potential reached by the electrodes, we can state that neither the maneuvering phase nor the final hovering phase are feasible with the spherical electrodes assumed here.

In Corradino (2018), an analysis that investigates the behavior of different electrode shapes in plasma is reported, and from this analysis the wire electrodes, in particular, if they are shaped like a loop, appear to be capable of reducing both the power consumption and the potential with respect to the spherical electrodes here presented. A detailed analysis of the simulations run by using the wire electrodes is presented in Sect. 2.15.5.

2.15.5 Current Collection for Wire Electrodes

From the analysis of several electrode shapes reported in Corradino (2018), good improvements from the power consumption point of view can be obtained by using a wire electrode. In particular, the high efficiency of the hoops in achieving an extremely low power consumption with a lower increment in the voltage with respect to a straight wire has been highlighted. This effect is given by the fact that hoop electrodes can be modeled exactly as wire electrodes but with a total length equal to the loop length. For this reason, in this section, the benefits that have been theoretically evaluated for a simpler static case in Corradino (2018) are simulated for the previously analyzed scenario in order to assess the feasibility of the maneuver itself by using a different electrode model (the hoops in this case).

The assumption of OML regime is valid also for type of electrodes, in particular for the case in which the radius of the wire is small (as in this case in which a radius of 1 mm has been assumed). The total current collection for a wire electrode is here modeled by using the empirical formulas derived in Choiniere et al. (2003) and Fuhrhop (2007) used also in Corradino (2018). For the case of negative hoop potential we can write that

$$I_{el} = \frac{1}{4} A_l e N_i \sqrt{\frac{8 k_B T_i}{\pi m_i}} \frac{2}{\sqrt{\pi}} \sqrt{T_i + F - V_l} \tag{2.140}$$

where A_l is the surface area of the loop, F is the energy of the ion beam computed as $F = \frac{1}{2e} m_i v_D^2$, and V_l is the potential of the wire. In the case of positive potential, the collected current can be computed as

$$I_{el} = \frac{1}{4} A_l \left(e N_e \sqrt{\frac{8 k_B T_e}{\pi m_e}} + e N_p \sqrt{\frac{8 k_B T_p}{\pi m_e}} \right) \frac{2}{\sqrt{\pi}} \sqrt{1 + X} \tag{2.141}$$

where X is the nondimensional potential defined in Choiniere et al. (2003) as $X = V / T_e$.

To perform simulations also for this case, a new spacecraft model is needed. To verify the possibility of using a wire-hoop electrode, a 1U CubeSat (CubeSat 2019) has been selected. Hence, the spacecraft's central body is a cube of $10 \times 10 \times 11$ cm of mass 1.33 Kg with optical properties equal to the previously analyzed cases. The hoops are assumed to be tangent to the rectangular side faces of the CubeSat. Each hoop is modeled as a circumference with the center of mass at 2.5 m from the center of mass of the central body, such that each hoop in this case has a radius of 2.445 m (see Fig. 2.79). As previously declared, the thickness of the wire that composes the hoop is assumed to be 1 mm. By using this new configuration, the center of mass of two opposite hoops is located at exactly 5 m of distance.

By assuming that the total charge of each hoop is concentrated in the center of mass of the hoops, the same model developed in Sect. 2.14.5 can be used to simulate

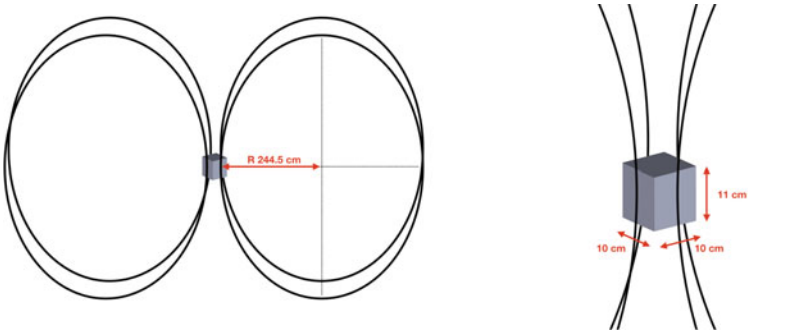

a) 1U E-Glider Concept b) 1U E-Glider Concept Detail

Fig. 2.79 1U E-Glider concept with wire electrodes (not to scale)

the spacecraft dynamics in 2D. For the case here presented, the distance between the two charges of a dipole is equal to 5 m.

Since the total mass of the CubeSat is halved with respect to the previous cases, the saturation level for both the net and differential charge can be reduced to $\pm 50\,\mu$C. For the maneuver here analyzed, the standard distance of 10 m between the charges cannot be used because the further portion of the "most inner hoop" may collide with the asteroid surface.

The results of the potential and power analysis are reported in Fig. 2.80. The upper plot shows the potential level of each electrode, while the second plot shows the total power needed to perform the maneuver and to keep the final condition.

Also in this case, the symmetry of the potential level assumed by two opposite electrodes can be noticed. During the initial transient phase, the potential of the electrodes is extremely high for all of them, reaching levels of about 500 KV and also showing strong oscillations from strongly positive to strongly negative values as a function of the polarity of the charges. During the position-keeping phase the levels of charge needed are lower, and as a result, the potential of the electrodes settles down to about 50 KV in modulus for the electrodes on the x-axis in the body frame, -150 KV for the electrode on the -y-axis in the BF frame, and about 100 KV for the electrode on the +y-axis in the BF frame.

The values obtained for the position-keeping phase are in agreement with the analysis of this type of electrodes developed in Corradino (2018), where the analysis was carried out using the convergence method previously introduced that led to the computation of the "true" capacitance C and the "true" potential V_{el} of an electrode in plasma. By using the results of the analysis in Corradino (2018), for a wire electrode with a radius of the wire of the order of 10^{-3} m and length of the order of 10^{1} m (as the case here analyzed), a potential of the order of about $10^{5} - 10^{6}$ volts can be expected for a spacecraft of comparable mass. Thus, by computing the potential of the electrodes as Q/C, a slightly overestimated value for the actual potential is obtained but inside the range provided in Corradino (2018). This makes the analysis carried

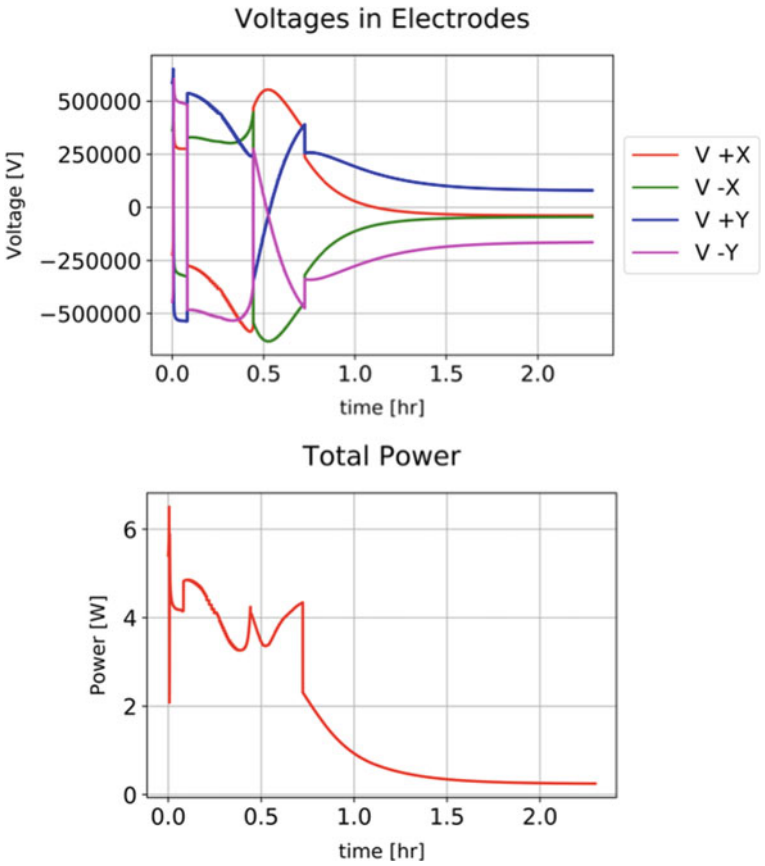

Fig. 2.80 Electrode potentials (upper) and total power needed (lower) for a four-Hoop 1U CubeSat

out in this work suitable at least for the preliminary evaluation of the feasibility of hovering on the sunlit side of an airless body.

The extremely high level of the potential is mainly due by the fact that the capacitance of a wire electrode is extremely low, of the order of 10^{-11} Farad. By considering the total power needed, we can immediately notice that the amount of power to be provided is low even during the initial transient phase. During the initial phase of the simulation, the power needed has a peak of about 6 W due to a peak on the potentials of all the electrodes. During the position keeping, the total power needed is extremely low, settling down to about 0.3 W. Also in this case, the result of the simulation is in agreement with the results of the parametric analysis on the total power required by a wire electrode reported in Corradino (2018) since a total power of the order of 10^{-1} W was expected.

In this case, by looking at the power level required, the maneuver and, in general, the hovering can be stated to be feasible with a state-of-the-art solution for onboard

power generation. The limiting factor here is confirmed to be the extremely high level of the potential, as already highlighted by previous analysis (Quadrelli et al. 2017b; Corradino 2018). The potential can be reduced by substantially increasing the length of the electrode. The increment in the total length can be achieved by using multiple hoops, but this can make the control law extremely complex due to the presence of a higher number of dipoles and due to the fact that the interferences among the electrodes (that are neglected here) can become relevant due to the short distance among two consecutive electrodes.

To assess the effects of a higher mass on the required power and on the electrode potential, we analyzed the case of a 12U CubeSat with four hoop electrodes.

2.15.6 *Example of a 12U CubeSat with Four Hoop Electrodes*

In this section, the results obtained from the analysis of a 12U CubeSat are reported. The central box-shaped body used for this simulation has the same dimensions of the 1HOPSat satellite (1HOPSat 2020) ($22.6 \times 22.6 \times 34$ cm) and a total mass of 22 Kg. Once again, the hoops are located on the side rectangular faces with the center of mass at a distance of 2.5 m from the center of mass of the central 12U structure (thus a radius of the hoop equal to 2.387 m; see Fig. 2.81). Also in this case, the thickness of the wire is set to be equal to 1 mm. The initial and the final conditions for the maneuver analyzed are the same as the previous case with a 1U CubeSat, and the optical properties of the external faces are unchanged. Due to the higher mass, the saturation level used in this case is $\pm 750\,\mu$C. The increment of the mass with respect to the 1U CubeSat previously analyzed affects only the net charge, resulting in a higher Q_0 and in a higher dQ needed to achieve the maneuver. The higher level of $Q = Q_0 + dQ$ makes the maneuver unfeasible for the low saturation limit since $|Q_0| > 50\,\mu$C.

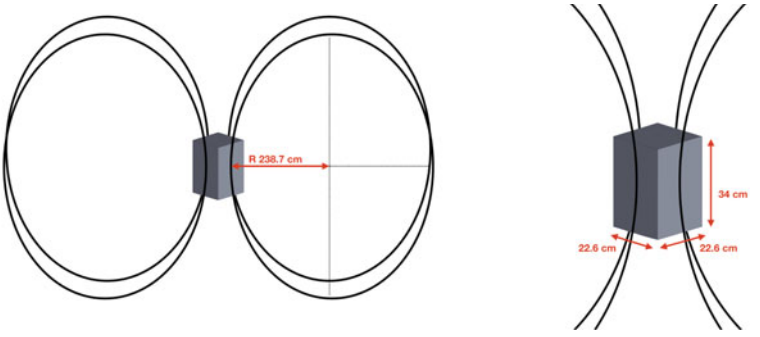

a) 12U E-Glider Concept b) 12U E-Glider Concept Detail

Fig. 2.81 12U E-Glider concept with wire electrodes (not to scale)

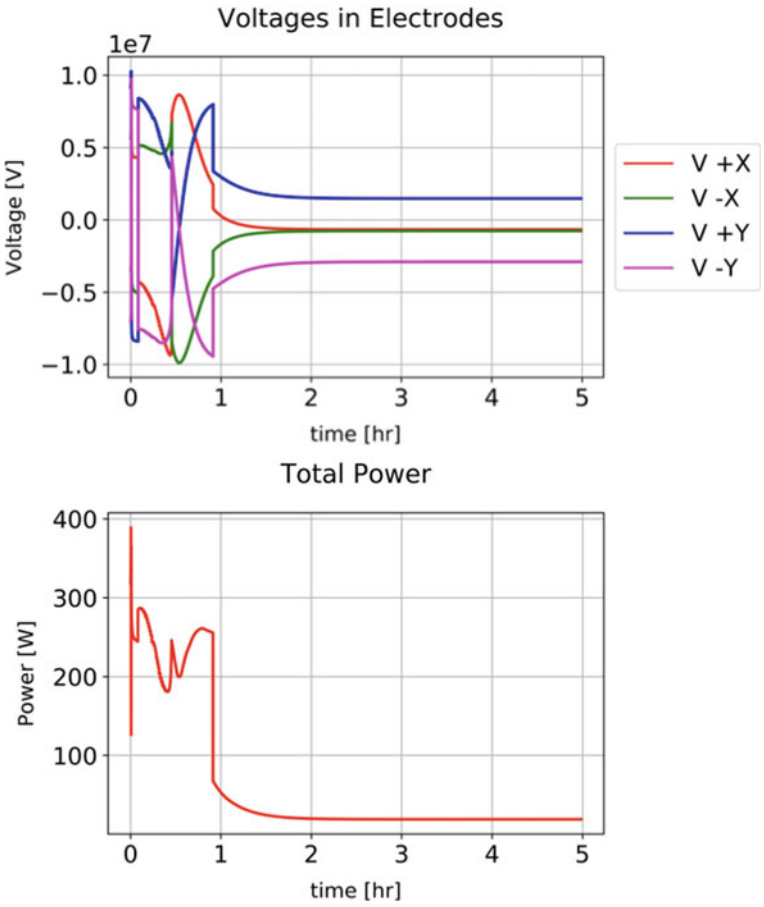

Fig. 2.82 Electrode potentials (upper) and total power needed (lower) for a four-Hoop 12U CubeSat

The selection of a new saturation level of $\pm 750\,\mu C$ leads to an increment in the saturation level itself with respect to the previous case which is almost proportional to the increment in the spacecraft mass. This makes the dynamics of the two simulations almost equal (the low differences detected are due to the different surface areas). This makes it possible to evaluate the changes in the total power required and in the electrode potentials due to a higher mass, and thus a higher level of charge needed. From the analysis already developed for a single static electrode in Corradino (2018), a nonlinear increment in the total power needed with respect to the increment in the mass of the spacecraft can be expected.

The resulting potential of the electrodes (upper) and the resulting total power (lower) are reported in Fig. 2.82. The results are proportional to the ones reported in Fig. 2.80.

During the transient phase, the potentials are extremely high, reaching peaks of about 10000 KV, which are practically unfeasible with the technology available nowadays for space applications. Also during the final position keeping, the potentials are high, reaching a level higher than 650 KV in modulus for each electrode (−650 KV is the potential of the electrodes aligned with the x-axis that results to be the ones with lower potential in modulus). The potential reaches scales linearly with the increment of mass (the small variations here are due to a different size of the hoops).

On the other side, the total power required is below 400 W during the entire transient phase. The total power settles down to a level of about 20 W and has an increment of about 60 times the power computed for the 1U CubeSat previously analyzed. This value is in agreement with the sensitivity analysis reported in Corradino (2018) in which a superlinear increment (power of $\sqrt{2}$) with the spacecraft mass has been identified. The total power levels obtained from this analysis are feasible for a 12U CubeSat spacecraft (e.g., the 6U solar panels produced by *Innovative Solutions In Space* can be used as a power source onboard).

The maneuver here analyzed is clearly feasible for a 12U E-Glider from a dynamical and power point of view, but it results to be unfeasible for the extremely high level of potential on each electrode. This analysis confirmed that the limiting factor for the development of an E-Glider mission is the potential level of the electrodes and not the power required to enable the electrostatic flight. Moreover, the total power needed and also the potential reached during the transient phase are much higher than the values computed for the final position keeping. This means that the feasibility of a given maneuver must also be carefully evaluated from the energetic viewpoint. The enhancement of the power needed during the maneuvering phase is due to the fact that the charge levels of the electrodes are substantially increased during this phase with respect to the ones needed during the position keeping. Also in this case, the increment obtained is not linear, in agreement with the analysis of the power consumption sensitivity with respect to the Q/M ratio developed in Corradino (2018), in which, again, a superlinear increment (power of $\sqrt{2}$) is identified.

The potential levels reached here for all the cases analyzed make mandatory a new evaluation of the effects of a spacecraft with such a high potential on the environment in which it operates. For example, if the plasma sheath of the spacecraft (enhanced by the extremely high potential) is wide enough to reach the surface of the asteroid, it may affect the photoelectron sheath of the main body itself, which can cause change of the flow of the particles and a modification in the solar wind effects, leading to strong variations in the previously computed conditions of hovering. Corradino (2018) reported a numerical simulation (provided by William Yu and Dr. Wang from USC) run by using the PIC method in which it is proven that a spacecraft with a potential of 1 KV, for the plasma here analyzed, has a sheath of a few Debye lengths, thus not high enough to strongly affect the results previously obtained. The same type of evaluation should also be carried out for higher potentials in order to try to define a limit potential that should not be exceeded. The extremely high potential may also prevent this type of technology to be applied to a planetary environment (thus in presence of an atmosphere) due to the atmospheric breakdown threshold that

should not be exceeded in order to avoid strong discharges (glow discharges), peak in the power needed for the levitation, and also possible damages to the electrode itself.

From the material viewpoint, the composition of all the electrodes here analyzed is a challenge; in particular, the sputtering and the erosion of the electrodes that can strongly limit the lifetime of an E-Glider mission must be evaluated. Finally, we showed that the current collection can be enhanced by a flowing plasma (Choiniere et al. 2003); thus, more exact numerical simulations with the PIC method should be useful to evaluate this increment for the cases here presented and eventually find a correction factor for the basic OML formulation assumed here.

2.16 Conclusions

This paper has proposed a novel flight mechanism around airless bodies in the solar system, utilizing the electrostatic field around them. The two distinct types of operations have been presented, namely, electrostatic hovering and electrostatic orbiting. We showed that both of these methods allow dayside operation without requiring any fuel. Therefore, the electrostatic flight around an asteroid offers significant advantages against conventional methods based on natural dynamics, from the perspective of mass budget, optical observation, solar power generation, and thermal design. By inducing the electrostatic force, several different artificial equilibrium points around an asteroid can be created, including the dayside equilibrium that cannot be observed in the natural dynamics. Electrostatic hovering can be achieved by placing a spacecraft at these artificial equilibrium points, and it could potentially be an option for effective proximity operation around asteroids. However, the power analyses showed that electrostatic hovering on the dayside requires high levels of power, based on our current model. For this reason, the electrostatic orbiting method was also discussed as an alternative strategy for an E-Glider operation. A new class of periodic orbits, called electrostatic periodic orbits, was successfully designed. These orbits exist on the dayside of an asteroid, requiring only a few watts of power for some cases. Moreover, the specific impulse of the E-Glider was found to be significantly higher than conventional propulsion systems. From these observations, the electrostatic orbiting strategy appears to be promising for asteroid missions.

Finally, the effects of an irregularly shaped asteroid, including the irregular gravitational field and the irregular electrostatic field, have been formulated and evaluated. As a result, an electrostatic periodic orbit solution can serve as a good approximation for an asteroid with a relatively small oblateness. Although an asteroid with a highly irregular shape perturbs the orbital motion significantly, possible approaches to this problem were also proposed, including feedback control of the spacecraft charge.

While much work remains to be carried out, including gaining additional insight into the engineering behavior, developing approaches for path planning and navigation, and conceiving plans to build and test a prototype, we conclude that the

electrostatic flight method using an E-Glider is useful for airless body missions and exhibits intriguing and valuable dynamic characteristics.

Acknowledgements ©2020. All rights reserved. This research was carried out at the Jet Propulsion Laboratory, California Institute of Technology, under a contract with the National Aeronautics and Space Administration, under the NASA Innovative Advanced Concepts Program. The authors are very grateful to Dr. Henry Garrett of JPL and many students who have worked at JPL with Dr. Quadrelli on the E-Glider, including Mr. Filippo Corradino of the Politecnico of Torino, Italy.

Nomenclature

d	Main body to Sun distance, m
h	Angular momentum, m^2/s
a	Semimajor axis, m
e	Eccentricity, -
P	Semilatus rectum, m
θ	True anomaly, deg
μ	Gravitational parameter, m^3/s^2
M	Mass, Kg
f	Force, N
N	Orbital angular velocity in a circular orbit, rad/s
ω	Angular velocity, rad/s
$\mathbf{J}$	Mass inertia moment matrix, kg m^2
$\mathbf{T}$	Torque vector, Nm
$\mathbf{a}$	Acceleration vector, m/s^2
$\mathbf{v}$	Velocity vector, m/s
$\mathbf{r}$	Position vector, m
$\mathbf{G}$	Gradient tensor of a vector field
C	Solar radiation pressure coefficient
$\mathbf{E}$	Electric field vector, V
q	Single charge, C
Q	Total net charge, C
$\boldsymbol{S}_q$	First moment of the charge vector, Cm
$\boldsymbol{I}_q$	Second moment of the charge tensor, Cm^2

Subscript

a	Asteroid
s	Sun
SC	Spacecraft
g	Gravitational
p	Solar radiation pressure
pa	Absorption
ps	Specular reflection
pd	Diffuse reflection

e Electrostatic
x, y, z General directions of a component in a vector/tensor
Superscript (for rotation matrices, the super- and subscripts refer to this list)
r Radial/in-track/cross-track (RIC) frame
a Asteroid-centered inertial (ACI) frame
b Body-fixed (BF) frame

References

1HOPSat Formal Orbital Debris Assessment Report (ODAR) and End of Mission Plan (EOMP). https://apps.fcc.gov/els/GetAtt.html?id=218010&x=. Accessed: 07-01-2020.

Aplin, K.L., Bowles, N., Urbak, E., and Sawyer, E.C. 2011. Asteroid electrostatic instrumentation and modelling. *Journal of Physics Conference Series*.

Aslanov, Vladimir, and Hanspeter Schaub. 2019. Detumbling attitude control analysis considering an electrostatic pusher configuration. *Journal of Guidance, Control, and Dynamics* 42 (4): 900–909.

Bechini, M. 2020. *E-glider. Modeling and simulation of an electrically actuated spacecraft in a PIC-described plasma field*, Politecnico di Milano, Tesi di Laurea Magistrale. https://www.politesi.polimi.it/handle/10589/153193.

Bechini, Michele, Quadrelli, Marco B., Lavagna, Michèle, and Wang, Joseph J. 2021. Hovering of an electrically actuated spacecraft in a small-body plasma field. *Journal of Spacecraft and Rockets* 58 (5): 1461–1476. https://doi.org/10.2514/1.A34954.

Beletsky, V.V., and Lavin, E.M. 1993. *Dynamics of space tether systems*. American Astronautical Society Publication. (Advances in the Astronautical Sciences). ISBN 0877033706.

Bellerose, Julie, and Yano, Hajime. 2010. Dynamics of asteroid 1999 JU3: target of the Hayabusa follow-on mission. *Transactions of JSASS Aerospace Technology Japan* 8 (ists27): Tk_23–Tk_28.

Besse, Arthur L., and Allen G. Rubin. 1980. A simple analysis of spacecraft charging involving blocked photoelectron currents. *Journal of Geophysical Research: Space Physics* 85 (A5): 2324–2328.

Bhattarai, Shankar, and Lekha Mishra. 2017. Theoretical study of spherical Langmuir Probe in Maxwellian plasma. *International Journal of Physics* 5 (08): 73–81.

Birdsall, C.K., and Langdon, A.B.: *Plasma physics via computer simulations*. Institute of Physics Publishing. (The Adam Hilger Series on Plasma Physics). – ISBN 9780750301176.

Broschart, S.B., and D.J. Scheeres. 2005. Control of hovering spacecraft near small bodies: application to asteroid 25143 Itokawa. *Journal of Guidance, Control, and Dynamics* 28 (2): 343–354.

Broschart, Stephen B., Daniel J. Scheeres, and Benjamin F. Villac. 2009. New families of multi-revolution terminator orbits near small bodies. *Advances in the Astronautical Sciences* 135 (3): 1685–1702.

Chen, F.C. 2003. *Langmuir probes diagnostics*. Electrical Engineering Department, University of California, Los Angeles, 2003 (Minicourse on Plasma Diagnostic).

Choiniere, Eric, Gilchrist, Brian, Bilen, Sven, and Fuhrhop, Keith. 2003. *Measurement of cross-section geometry effects on electron collection to long probes in mesosonic flowing plasmas*. In *39th AIAA/ASME/SAE/ASEE joint propulsion conference and exhibit*. https://arc.aiaa.org/doi/abs/10.2514/6.2003-4950.

Clark, Beth E., Bruce Hapke, Carlé Pieters, and Daniel Britt. 2002. Asteroid space weathering and regolith evolution. *Asteroids III* 585: 90086–2.

Colwell, Joshua E., Amanda A. Gulbis, Mihály Horányi, and Scott Robertson. 2005. Dust transport in photoelectron layers and the formation of dust ponds on Eros. *Icarus* 175 (1): 159–169.

Corradino, F. 2018. *Modeling of orbital and attitude dynamics of a satellite controlled via active electrostatic charging*, Politecnico di Torino, Tesi di Laurea Magistrale. https://webthesis.biblio.polito.it/6853/1/tesi.pdf.

CubeSats Overview. https://www.nasa.gov/mission_pages/cubesats/overview. Accessed 03-10-2019.

Council, National R. 2011. *Vision and voyages for planetary science in the decade 2013–2022*. Washington, DC : The National Academies Press. https://www.nap.edu/catalog/13117/vision-and-voyages-for-planetary-science-in-the-decade-2013-2022. ISBN 978-0-309-22464-2.

Cui, C, and Wang, J. 2019. Numerical simulations of plasma-spacecraft interactions near irregularly shaped small asteroids. In *Applied Space Environments Conference* Los Angeles, CA.

Curtis, H.D. 2010. *Orbital mechanics for engineering students*, 3rd edn. Elsevier. – ISBN 9780080977478.

Czepiela, Steven A., Hugh McManus, and Daniel Hastings. 2000. Charging of composites in the space environment. *Journal of Spacecraft and Rockets* 37 (5): 556–560.

Eckman, R.A., Brown, A.J., and Adamo, D.R. 2011. Normalization of gravitational acceleration models. In *NASA scientific and technical information*. https://ntrs.nasa.gov/archive/nasa/casi.ntrs.nasa.gov/20110023121.pdf.

Evlanov, E.N., M.A. Zavjalov, and P.M. Tyuryukanov. 2013. Electron guns for spacecraft. *Cosmic Research* 51 (5): 388–395.

Fantino, E., and S. Casotto. 2009. Methods of harmonic synthesis for global geopotential models and their first-, second- and third-order gradients. *Journal of Geodesy* 83 (7): 595–619.

Finckenor, M.M. 1999. Multilayer insulation material guidelines. In *National aeronautics and space administration*. https://ntrs.nasa.gov/archive/nasa/casi.ntrs.nasa.gov/19990047691.pdf.

Fuhrhop, Keith. 2007. *Theory and experimental evaluation of electrodynamic tether systems and related technologies.*, The University of Michigan, Dissertation. https://deepblue.lib.umich.edu/bitstream/handle/2027.42/57663/kfuhrhop_1.pdf?sequence=2&isAllowed=y.

Fujiwara, Akira, J. Kawaguchi, D.K. Yeomans, M. Abe, T. Mukai, T. Okada, J. Saito, H. Yano, M. Yoshikawa, D.J. Scheeres, et al. 2006. The rubble-pile asteroid Itokawa as observed by Hayabusa. *Science* 312 (5778): 1330–1334.

Gorham, P. 2013. Ballooning spiders: the case for electrostatic flight. *eprint* arXiv:1309473.

Gottlieb, R.G. 1993. Fast gravity, gravity partials, normalized gravity, gravity gradient torque and magnetic field: derivation, code and data. *Nasa Contractor Report 188243*. https://ntrs.nasa.gov/archive/nasa/casi.ntrs.nasa.gov/19940025085.pdf.

Han, D. 2015. *Particle-in-cell simulations of plasma interaction with asteroidal and lunar surfaces*, University of South California, Dissertation. http://digitallibrary.usc.edu/cdm/ref/collection/p15799coll3/id/639389.

Han, D., J. Wang, and X. He. 2016a. A nonhomogeneous immersed-finite-element particle-in-cell method for modeling dielectric surface charging in plasmas. *IEEE Transactions on Plasma Science* 44 (8): 1326–1332.

Han, Daoru, Wang, Pu, He, Xiaoming, Lin, Tao, and Wang, J. 2016b. A 3D immersed finite element method with non-homogeneous interface flux jump for applications in particle-in-cell simulations of plasma-lunar surface interactions. *Journal of Computational Physics* 321 : 965 – 980. ISSN 0021-9991.

Han, Daoru, and Joseph Wang. 2019. 3-D fully kinetic particle-in-cell simulations of small asteroid charging in the solar wind. *IEEE Transactions on Plasma Science* 47 (8): 3682–3688.

Han, Daoru, Joseph J. Wang, and Xiaoming He. 2018. Immersed finite element particle-in-cell simulations of plasma charging at the lunar terminator. *Journal of Spacecraft and Rockets* 55 (6): 1490–1497.

Hartzell, C.M. 2012. *The dynamics of near-surface dust on airless bodies*, University of Colorado Boulder, Dissertation, 2012. https://scholar.colorado.edu/concern/graduate_thesis_or_dissertations/6w924c073.

Havnes, O., C.K. Goertz, G.E. Morfill, E. Grün, and W. Ip. 1987. Dust charges, cloud potential, and instabilities in a dust cloud embedded in a plasma. *Journal of Geophysical Research: Space Physics* 92 (A3): 2281–2287.

Hénon, Michel. 1969. Numerical exploration of the restricted problem, V. Hill's case: periodic orbits and their stability. *Astronomy and Astrophysics* 1: 223–238.

Hirata, Naoyuki, and Hideaki Miyamoto. 2012. Dust levitation as a major resurfacing process on the surface of a saturnian icy satellite. *Atlas. Icarus* 220 (1): 106–113.

Hughes, P.C. 1986. *Spacecraft attitude dynamics*, 0471818429. ISBN: Wiley Inc.

Ip, W.H. 1986. Electrostatic charging and dust transport at Mercury surface. *Geophysical Research Letters* 13: 1133–1136.

Iwata, Minoru, Arifur R. Khan, Hideyuki Igawa, Kazuhiro Toyoda, Mengu Cho, and Tatsuhito Fujita. 2012. Development of electron-emitting film for spacecraft charging mitigation. *Journal of Spacecraft and Rockets* 49 (3): 546–552.

Jeong, H. 2008. *Kinetic simulations of spacecraft charging and plasma interactions in the solar wind*, Virginia Polytechnic Institute and State University, Dissertation. https://vtechworks.lib.vt.edu/bitstream/handle/10919/30237/Dissertation_Jeong.pdf?sequence=1&isAllowed=y.

Kafafy, R., T. Lin, Y. Lin, and J. Wang. 2005. Three-dimensional immersed finite element methods for electric field simulation in composite materials. *International Journal for Numerical Methods in Engineering* 64 (7): 940–972.

Kafafy, R., and J. Wang. 2006. A hybrid grid immersed finite element particle-in-cell algorithm for modeling spacecraft-plasma interactions. *IEEE Transactions on Plasma Science* 34 (5): 2114–2124.

Khan, Arifur R., Minoru Iwata, Kazuhiro Toyoda, Mengu Cho, Setuo Tomonari, and Yuta Takaki. 2013. In-orbit demonstration of newly developed passive electron-emitting film for spacecraft-charging mitigation. *Journal of Spacecraft and Rockets* 50 (4): 853–859.

Kikuchi, S. 2017. *E-glider: active electrostatic flight for airless body exploration*. Research Report: The University of Tokyo.

King, B.L., Parker, G.G., Deshmukh, S., and Chong, J.H. 2002. NIAC phase i final report - spacecraft formation-flying using inter-vehicle coulomb forces. In *NASA Innovative Advanced Concepts (NIAC)* (2002). – http://www.niac.usra.edu/files/studies/final_report/601King.pdf.

Kobrick, Ryan, Hoffman, Jeffrey, Street, Kenneth, and Rickman, Douglas. 2014. Overview of instruments for investigating dust interactions on small solar system bodies by landers and rovers, 09.

Kominato, Takashi, Masatoshi Matsuoka, Masashi Uo, Tatsuaki Hashimoto, and Jun'ichiro Kawaguchi. 2006. Optical hybrid navigation and station keeping around Itokawa. *In AIAA/AAS Astrodynamics Specialist Conference and Exhibit* 2006: 6535.

Kryszczyńska, A., La. Spina, Paolicchi Alessandra, Harris Paolo, and AW, Breiter, S, and Pravec, P. 2007. New findings on asteroid spin-vector distributions. *Icarus* 192 (1): 223–237.

Laframboise, J.G., and L.W. Parker. 1973. Probe design for orbit? limited current collection. *The Physics of Fluids* 16 (5): 629–636.

Lai, S.T. 1989. An overview of electron and ion beam effects in charging and discharging to spacecraft. *IEEE Transactions on Nuclear Science* 36 (6): 2027–2032.

Lee, P. 1996. Dust levitation on asteroids. *Icarus* 124 (1): 181–194.

Lundberg, B.J. 1988. Recursion formulas of legendre functions for use with nonsingular geopotential models. *Journal of Guidance, Control, and Dynamics* 11 (1): 31–38.

Lyon, H.R. 2004. *Geosynchronous orbit determination using space surveillance network observations and improved radiative force modeling*, Massachusetts Institute of Technology, Master Degree Thesis. https://dspace.mit.edu/handle/1721.1/17779.

Masek, T.D., and H.A. Cohen. 1978. Satellite positive-ion-beam system. *Journal of Spacecraft and Rockets* 15 (1): 27–33.

Mendis, D.A., Jay R. Hill, Harry L. Houpis, and E.C. Whipple. 1981. On the electrostatic charging of the cometary nucleus. *The Astrophysical Journal* 249: 787–797.

Miyamoto, H., et al. 2007. Regolith migration and sorting on asteroid Itokawa. *Science* 316 (5827): 1011–1014.

Mizera, P.F. 1983. A summary of spacecraft charging results. *Journal of Spacecraft and Rockets* 20 (5): 438–443.

Morley, Erica L., and Daniel Robert. 2018. Electric fields elicit ballooning in spiders. *Current Biology* 28 (14): 2324–2330.

Mott-Smith, H.M., and Irving Langmuir. 1926. The theory of collectors in gaseous discharges. *Physical Review* 28: 727–763.

NASA: *State of the art of small spacecraft technologies - NASA*. https://sst-soa.arc.nasa.gov/03-power. Accessed: 07-01-2020.

Nesnas, Issa A., Matthews, Jaret B., Abad-Manterola, Pablo, Burdick, Joel W., Edlund, Jeffrey A., Morrison, Jack C., Peters, Robert D., Tanner, Melissa M., Miyake, Robert N., Solish, Benjamin S., and Anderson, Robert C. 2012. Axel and DuAxel rovers for the sustainable exploration of extreme terrains. *Journal of Field Robotics* 29 (4): 663–685. https://onlinelibrary.wiley.com/doi/abs/10.1002/rob.21407.

Nitter, T., O. Havnes, and F. Melandsø. 1998. Levitation and dynamics of charged dust in the photoelectron sheath above surfaces in space. *Journal of Geophysical Research: Space Physics* 103 (A4): 6605–6620.

Nolan, Michael C., Christopher Magri, Ellen S. Howell, Lance A. Benner, Jon D. Giorgini, Carl W. Hergenrother, R.S. Hudson, Dante S. Lauretta, Jean-Luc. Margot, Steven J. Ostro, et al. 2013. Shape model and surface properties of the OSIRIS-REx target Asteroid (101955) Bennu from radar and lightcurve observations. *Icarus* 226 (1): 629–640.

Olhoeft, G.R., and D.W. Strangway. 1975. Dielectric properties of the first 100 meters of the Moon. *Earth and Planetary Science Letters* 24 (3): 394–404.

Peck, Mason. 2005. Prospects and challenges for lorentz-augmented orbits. *In Collection of technical papers - AIAA guidance, navigation, and control conference* 3: 08.

Pines, S. 1973. Uniform representation of the gravitational potential and its derivatives. *AIAA Journal* 11 (10): 1508–1511.

Plis, Elena A., Daniel P. Engelhart, Justin Likar, Ryan C. Hoffmann, Russell Cooper, and Dale Ferguson. 2018. Electrical behavior of carbon-loaded kapton for spacecraft applications. *Journal of Spacecraft and Rockets* 55 (3): 775–777.

Poppe, Andrew R. 2011. *Modeling, theoretical and observational studies of the lunar photoelectron sheath*, University of Colorado at Boulder, Dissertation.

Páscoa, José, Teixeira, Odelma, and Ribeiro, Gustavo. 2018. A review of propulsion systems for CubeSats.

Quadrelli, B.M., and Bhaskaran, S. 2019. *Navigation in low gravity*, Ang M., Khatib O., Siciliano B. ed., Encyclopedia of robotics. Berlin: Springer.

Quadrelli, B.M., Kowalchuck, S., and Chang, J. 2004. Dynamics and control of a herd of sondes guided by a Blimp on Titan. In *14th AAS/AIAA space flight mechanics meeting*, 2004, 5310.

Quadrelli, B.M., Wood, L.J., Riedel, J.E., McHenry, M.C., Aung, M., Cangahuala, L.A., Volpe, R., Beauchamp, P.M., and Cutts, J. 2015. Guidance, navigation, and control technology assessment for future planetary science missions, journal of guidance, control, and dynamics. *Journal of Guidance, Control, and Dynamics* 1165–1186.

Quadrelli, M. B., Garrett, H., Castillo, J., Stoica, A., and Ono, H. 2017a. Schaub: active electrostatic flight for airless body. In *2017 IEEE aerospace conference* 1–16.

Quadrelli, M.B., Garrett, H., Castillo, J., Stoica, A., and Ono, H. 2017b. Schaub: NIAC phase I final report - E-Glider: active electrostatic flight for airless body exploration. *NASA innovative advanced concepts (NIAC)*. https://www.nasa.gov/sites/default/files/atoms/files/niac_2016_phasei_quadrelli_eglider_tagged.pdf.

Quadrelli, Marco B., Mazhar, Hammad, and Negrut, Dan. 2012. Modeling and simulation of anchoring processes for small body exploration. In *AIAA SPACE 2012 conference and exposition*, 5310.

Renno, Kok. 2008. Electrical activity and dust lifting on earth, mars, and beyond. *Space Science Reviews* 137 (11): 419–434.

Schaub, Hanspeter, Gordon G. Parker, and Lyon B. King. 2004. Challenges and prospects of coulomb spacecraft formation control. *Journal of Astronautical Sciences* 52 (1): 169–193.
Scheeres, D. 1994. Satellite dynamics about asteroids. In *AAS/AIAA spaceflight mechanics meeting*.
Scheeres, D. 2007. Orbit mechanics about small asteroids. *NASA Archive* 01. https://ntrs.nasa.gov/archive/nasa/casi.ntrs.nasa.gov/20080012725.pdf.
Scheeres, D. 2012. *Orbital motion in strongly perturbed environments*. Bd. 1. Springer.
Scheeres, D.J. 1999. Satellite dynamics about small bodies: averaged solar radiation pressure effects. *Journal of the Astronautical Sciences* 47 (1): 25–46.
Scheeres, D.J., Gaskell, R., Abe, S., Barnouin-Jha, O, and Hashimoto, T. 2006. The actual dynamical environment about Itokawa. In *AIAA/AAS astrodynamics specialist conference and exhibit*.
Scheeres, D.J., and F. Marzari. 2002. Spacecraft dynamics in the vicinity of a comet. *Journal of the Astronautical Science* 50 (1): 35–52.
Seeni, Aravind, Schäfer, Bernd, and Hirzinger, Gerd. 2010. *Robot mobility systems for planetary surface exploration - state-of-the-art and future outlook: a literature survey*, 189–208. Aerospace Technology Advancements.
Seydel, Rüdiger. 2009. *Practical bifurcation and stability analysis*. Bd. 5. Springer Science & Business Media.
Stubbs, Timothy J., Richard R. Vondrak, and William M. Farrell. 2006. A dynamic fountain model for lunar dust. *Advances in Space Research* 37 (1): 59–66.
Vladimirov, et al. 2005. *Physics and Applications of Complex Plasmas*. Imperial College Press.
Wang, J., Y. Cao, R. Kafafy, J. Pierru, and V.K. Decyk. 2006. Simulations of ion thruster plume-spacecraft interactions on parallel supercomputer. *IEEE Transactions on Plasma Science* 34 (5): 2148–2158.
Wang, Joseph, and Hastings, D.E. 1992. Ionospheric plasma flow over large high-voltage space platforms. II: The formation and structure of plasma wake. *Physics of Fluids B: Plasma Physics* 4 (6): 1615–1629
Wang, Joseph, and Yuan Hu. 2018. The breakdown of the fluid approximation for electrons in a plasma wake. *Journal of Geophysical Research: Space Physics* 123 (10): 8797–8805.
Whipple, Elden C. 1981. Potentials of surfaces in space. *Reports on progress in Physics* 44 (11): 1197–1250.
Withrow-Maser, Shannah, Koning, Witold, Kuang, Winnie, and Johnson, Wayne R. 2020. Recent efforts enabling martian rotorcraft missions. In *NASA Technical Reports Server (NTRS)*. https://ntrs.nasa.gov/archive/nasa/casi.ntrs.nasa.gov/20200000788.pdf.
Yu, W., J. Wang, and D. Han. 2016. *2016*. In AIAA space: Numerical modeling of dust dynamics around small asteroids.
Yu, Wiliam, Daoru Han, and Joseph Wang. 2019. Numerical simulations of dust dynamics around small asteroids. *IEEE Transactions on Plasma Science* 47 (8): 3724–3730.